Title

A Monte Carlo Method for Identifying Imaging Systematics in Galaxy Surveys

Permalink

https://escholarship.org/uc/item/3w60x4c9

Author

Burleigh, Kaylan

Publication Date

2018

Peer reviewed|Thesis/dissertation

A Monte Carlo Method for Identifying Imaging Systematics in Galaxy Surveys

By

Kaylan Burleigh

A dissertation submitted in partial satisfaction of the

requirements for the degree of

Doctor of Philosophy

in

Astrophysics

in the

Graduate Division

of the

University of California, Berkeley

Committee in charge:
Professor Aaron Parsons, Co-chair
Professor Joshua Bloom, Co-chair
Professor Peter Nugent
Professor Philip Stark

Summer 2018

A Monte Carlo Method for Identifying Imaging Systematics in Galaxy Surveys

Abstract

A Monte Carlo Method for Identifying Imaging Systematics in Galaxy Surveys

by

Kaylan Burleigh

Doctor of Philosophy in Astrophysics

University of California, Berkeley

Professor Aaron Parsons, Co-chair
Professor Joshua Bloom, Co-chair

The Dark Energy Spectroscopic Instrument (DESI) will soon start to obtain optical spectra for tens of millions of galaxies and quasars, constructing a 3–dimensional map spanning the nearby universe to 10 billion light–years. DESI aims to use the fossil imprint of sound waves from the first 380,000 years of the universe, which is still detectable as a pattern of temperature variations in the cosmic microwave background radiation (CMB), to measure how the universe has evolved since then the Baryon Acoustic Oscillations (BAO) technique. The early CMB temperature differences map early variations in density (the sound waves) that subsequently evolved into the clustering of galaxies and intergalactic gas (the baryons), as well as dark matter at recurrent intervals throughout space. These regularly spaced clusterings are consistent over time, very much like a ruler to measure the universe, with the CMB at one end. This allows one to measure the effect of dark energy on the expansion of the universe.

This thesis presents my work as a member of the DESI Imaging Team, for which I received DESI Builder status. We transform images of the night sky into a catalog of positions properties of automatically detected and measured astrophysical sources. This catalog will contain billions of astrophysical sources, but just a subset (tens of millions) of sources will be selected for spectroscopic observation with DESI. I was involved in all stages of the Legacy Surveys, from carrying out observations to building the large–scale-structure catalogs.

A major challenge for they Legacy Surveys is understanding the inevitable biases and systematics in their galaxy samples. The key product of my thesis is a Monte Carlo method, called `Obiwan`, that adds simulated sources to random locations in astronomical images and then performs source detection and measurement, characterizing the complex selection inherent in large–scale–structure catalogs. The process is repeated until the injected source density is high enough to satisfy one's science objectives. For instance, the DESI target density for emission line galaxies (ELGs) is 2400 deg^2, so simulated ELGs should be injected at more than 10 times this density.

I dedicate this thesis to God, my wife Sean and our daughter Ryan, my parents Stacy and Harry, my Grandpa Pete, and my in–laws Susan, Bruce, Shane, and Taylor.

Contents

List of Figures

List of Tables

Acknowledgments

- Peter Nugent and David Schlegel, you took me under your wing at a crucial moment in graduate school. You healed my weaknesses and resurrected my love for science and astronomy. I am your Padawan learner, you are my Jedi Masters.

- Aaron Parsons, Arjun Dey, and John Moustakas, you also took me under your wing. Thank you for helping me deal with conflict and for improving how I communicate.

- DESI Imaging Team, you taught me what a Team is and that I thrive in a team environment. Thanks for making the work fun, especially our Team Captains, David Schlegel and Arjun Dey.

- DESI Collaboration, what a great collaboration to be apart of.

- Qual and Thesis Committee, Joshua Bloom, Peter Nugent, Aaron Parsons, and Philip Stark, thank you for making sure I learned the skill I needed.

- Avengers, that was a long six years with many ups and downs. Thank you for going through it with me.

- UCB Astro, thank you for giving me the chance six years ago. It has been a privilege working with all of you.

Chapter 1

Introduction to Galaxy Surveys for Cosmology

1.1 The Big Bang Theory

The Cosmic Microwave Background (CMB), a uniform background radiation field everywhere one looks in the Universe (a blackbody with temperature of $2.7255\,$K), is the strongest evidence astronomers have for the Big Bang theory, which holds that our Universe has both increased in size and cooled from an initially smaller and hotter state. The CMB was predicted in 1948 by Ralph Alpher and collaborators (Alpher et al. 1948a,b; Alpher & Herman 1948a,b), and was later detected in 1964 by Penzias & Wilson (1965). For a historical review see Partridge (2007). Precise measurements thereafter (Smoot et al. 1992; Bennett et al. 2003; Planck Collaboration 2016) reveal that the CMB is incredibly uniform to one part in $\pm 10^{-5}\,$K. Fig. 1.1 (reproduced from Fixsen et al. 1996) shows the Cosmic Background Explorer (COBE) measurement of the CMB using the Far Infrared Absolute Spectrophotometer (FIRAS) instrument. The data are so precise (Planck blackbody spectrum for $T \sim 2.7$ K, black line) that the error bars are smaller than the thickness of the line (Fixsen et al. 1996).

Well before the discovery of the CMB, Edwin Hubble showed that the universe was expanding (Hubble 1929). Farther–away galaxies appear to move way from the Milky Way faster than closer galaxies. Combining an expanding universe (Hubble) with the Big Bang theory (the CMB) has motivated the last decades of research to answer/investigate, how did the universe expand? Did it expand with constant velocity or were there periods of acceleration or deceleration?

Recent independent measurements of the expansion rate, namely CMB, supernovae, and galaxy–redshift surveys (Weinberg et al. 2013), all agree that their data is best described by a ΛCDM cosmological model[1], which says that our Universe is 13.8 billion years old, expanding with increasing speed, and composed of 5% regular matter (galaxies, stars, planets, the

---

[1]The standard model for a universe beginning from a Big Bang that contains dark energy (denoted by a cosmological constant, Λ) and cold dark matter (CDM)
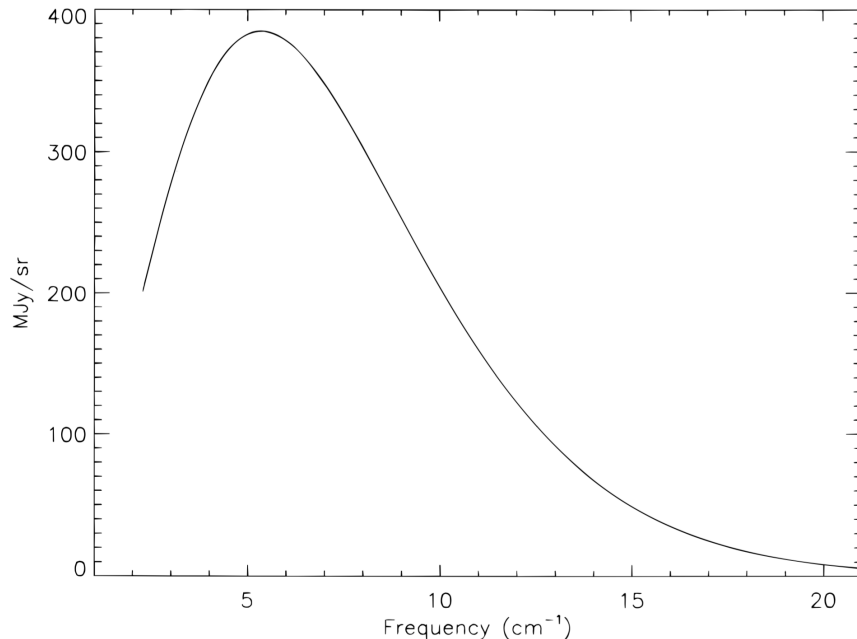
Figure 1.1: COBE measurement of the CMB using the FIRAS instrument. The data are so precise (Planck blackbody spectrum for $T \sim 2.7$ K, black line) that the error bars are smaller than the thickness of the line. Reproduced from Fixsen et al. (1996).

periodic table, etc.), 25% dark matter (particles that do not interact with photons and that only interact with regular matter via gravity), and 70% dark energy (a component we know almost nothing about, except that it also does not interact with light and that it is causing the apparent accelerated expansion of the universes).

1.2 Baryonic Acoustic Oscillations (BAO)

This dissertation focuses on detecting a signal that was imprinted on the distribution of regular matter in the Universe during the period of 3 minutes to 380,000 years after the Big Bang. After 3 minutes, the Universe is an ionized photon–baryon fluid that is being acted upon by a background gravitational field due to (at first) photons and neutrinos and (later) dark matter. Photons, electrons, and protons are in thermodynamic equilibrium (i.e., their energy distributions are described by the same temperature). Photons and electrons interact by Thomson scattering and electrons and protons interact by Coulomb scattering. At ~ 3 minutes, the photon–baryon fluid had a temperature of about 10^9 K and the radiation field was very uniform (just like the CMB we see today). Small variations in temperature and density launched sound waves in the photon–baryon fluid (a.k.a. Baryonic Acoustic Oscillations) where radiation pressure from the photons pushed fluid outwards and the background

gravitational potential, acting on the electrons and protons, pulled them inwards. There were about 10^9 more photons than baryons so the baryons contributed a negligible pressure (10^9 times less) than the photons. These waves continued for about 380,000 years until the Universe had cooled enough (to about 3,000 K) for electrons and protons to combine (a phase–transition that astronomers call "recombination"). The tail of the 3,000 K blackbody spectrum did not contain enough ionizing photons to prevent electrons and protons from combining. The photon–baryon fluid separated into two entities, a baryon fluid and free streaming photons, each containing the BAO signal. The photon fluid was a nearly perfect blackbody with a temperature that decreased as the universe expanded, from an initial $3,000$ K to the 2.7 K CMB. The baryon fluid flowed into dark matter dominated, gravitational potential wells. Regions of high baryon and dark matter density formed the first stars and galaxies.

Although the BAO can be seen in the CMB and the distribution of galaxies today, its characteristic length–scale (~ 150 Mpc) was determined $\sim 380,000$ years after the Big Bang. 150 Mpc is the comoving distance that photon–baryon sound waves, moving at $\sim 1/\sqrt{3}$ times the speed of light, can travel in 380,000 years; this correlates the distances between over–dense regions in the baryon–photon fluid, which are future sites of galaxy formation. The BAO signal is detectable as a relative increase in the number of galaxy pairs with 150 Mpc separation compared to other separations. The BAO signal is preserved in the distribution of galaxies ~ 13.8 billion years after recombination because the nonlinear processes, such as the gravitational growth of structure and redshift space distortions, only affect small scales ($\ell < 40$ Mpc) (Weinberg et al. 2013).

Fig. 1.2 shows the power spectra of temperature variations in the CMB (top) and density variations in the distribution of matter (bottom), which show what the BAO signal looks like in Fourier space. A peak in configuration space at $\ell \sim 150$ Mpc corresponds to a series of oscillations in Fourier space, roughly at $k \sim 2\pi/\ell \approx 0.06$ h Mpc^{-1}. The vertical–axis is the root mean square (RMS) deviation from a uniform temperature (T~ 2.7K) for the CMB and the deviation from the average density of matter in the universe for matter. The horizontal–axis is the wavenumber, with larger scales on the left. The peaks in the radiation spectrum are offset from that of the matter spectrum, and the relative amplitudes of the peaks are larger for the radiation spectrum. Both effects are primarily due to baryons constituting only about 15% of matter ($\Omega_b/\Omega_m \sim 0.15$), which dilutes the BAO signal in the matter spectrum. It is important to note two non–BAO features in Fig. 1.2. The CMB spectrum, on very large scales ($k < 0.01$ h/Mpc), contains information about the primordial fluctuations (the small variations in temperature and density at ~ 3 minutes) that launched the initial sound waves in the photon–baryon fluid; second, the largest feature in the matter power spectrum is the turnaround or peak at $k \sim 0.03$ h Mpc^{-1}, which corresponds to the comoving scale where the universe transitions from radiation dominated (on larger scales) to matter dominated (on smaller scales). For more details about the physics responsible for the BAO, see Silk (1968); Peebles & Yu (1970); Sunyaev & Zeldovich (1970); Doroshkevich et al. (1978); Hu & White (1996); Eisenstein & Hu (1998); Meiksin et al. (1999), or for a recent pedagogical discussion, see Eisenstein et al. (2007); Eisenstein & Bennett (2008); Anderson et al. (2012);

Weinberg et al. (2013); Slepian & Eisenstein (2015).
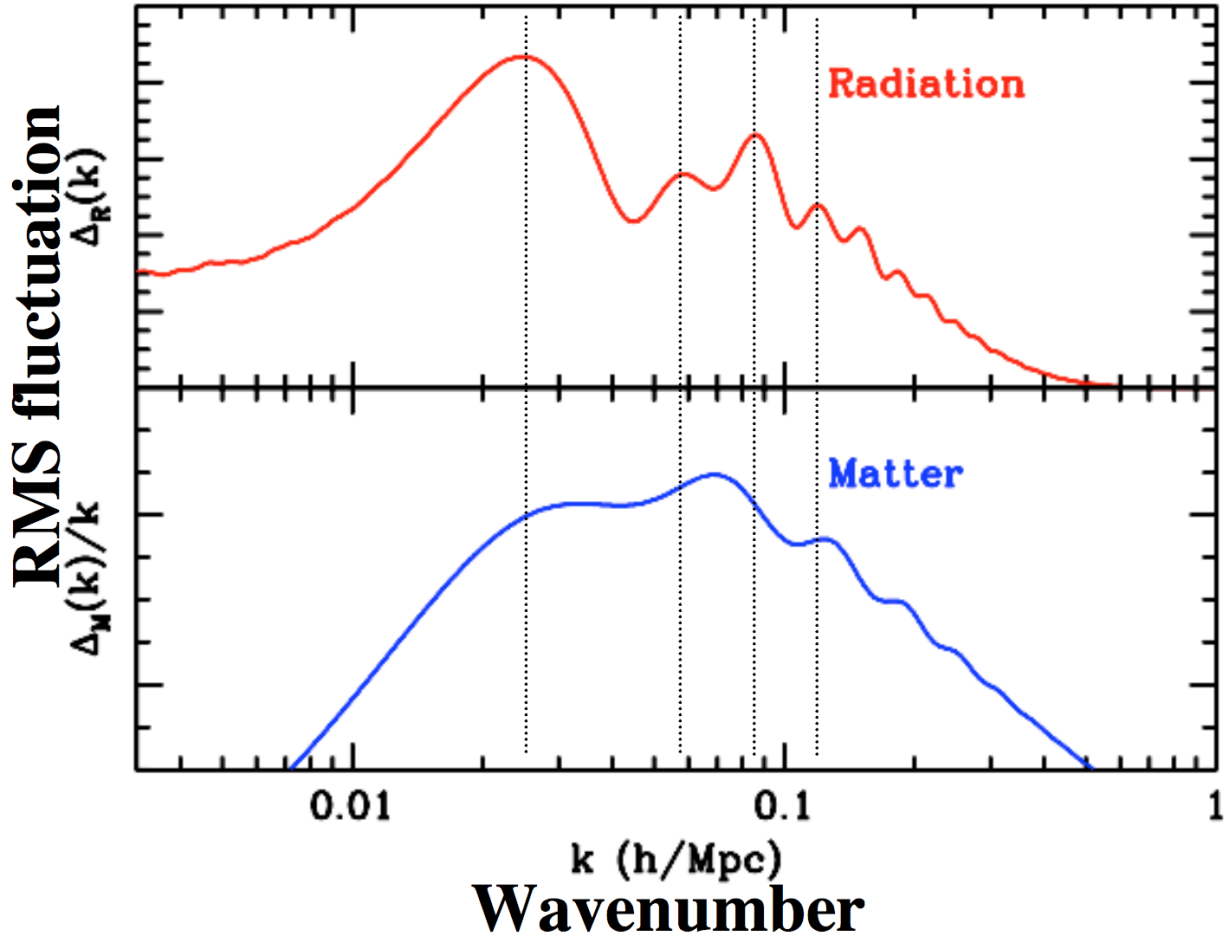
Figure 1.2: The BAO signal is present in both the CMB (top) and matter power spectra (bottom). Image Credit: Martin White, reproduced with permission.[3]

1.3 Galaxy Surveys

1.3.1 Collecting a Sample

Galaxy surveys image as much of the the night sky as possible, using the largest possible telescope(s), to collect a sample of galaxies spanning a large volume of the observable universe. Galaxies (baryons) trace the distribution of dark matter, which dominates the gravitational potential of the universe on large scales. This allows the BAO signal, and other clustering statistics, to be measured from a 3–dimensional map of galaxy positions.

Clustering statistics, such as the two–point correlation function, provide a measure of the expansion rate of the universe. Images of the night sky are transformed into a 2–dimensional large–scale–structure catalog by passing them through a pipeline that automatically detects and models galaxies and stars in the calibrated images. This becomes a 3–dimensional catalog by selecting galaxies of a specific type and obtaining spectra and measuring redshifts for them. Clustering statistics are then computed from the positions of the galaxies on the sky.

1.3.2   Galaxy Type

Although the locations of all galaxies are correlated with the distribution of dark matter, certain types of galaxies are much more correlated than others. Luminous red galaxies (LRGs) are one of the strongest present–day tracers of dark matter because they and their dark matter halos are relatively massive and they reside in galaxy groups and large galaxy clusters. Emission line galaxies (ELGs), blue star–forming galaxies, are poorer tracers because they have relatively low mass and star formation was more active in the past ($\sim$ 7–10 billion years ago). However, ELGs are preferable to LRGs at high redshift ($z > 1$) because the spectra of newly formed stars have relatively easy–to–detect emission lines. Astronomers quantify the strength of the tracer by the bias (b), which relates the galaxy power spectrum (P_g) to the matter power spectrum (P_{cdm}, Kaiser 1984; Desjacques et al. 2016),

$$P_g(k) = b^2 P_{cdm}(k). \tag{1.1}$$

LRGs have biases of $\sim$ 1.5–2 at redshifts of $0 < z < 1$ (Tegmark et al. 2006; Anderson et al. 2012, 2014), while ELGs have biases of $\sim$ 0.9–1.5 at redshifts of $0.6 < z < 2$ (Geach et al. 2008; Blake et al. 2009; Sumiyoshi et al. 2009; Comparat et al. 2013; DESI Collaboration 2016a). Two fundamental questions for any galaxy survey are, what type of galaxy should we target and how many of them do we need to observe? The following shows that the bias is the primary way to answer these questions.

Clustering measurements are limited by Poisson (Shot) noise and sample variance. Shot noise is the uncertainty due to counting, where observing more galaxies decreases the standard error by $\propto 1/\sqrt{N}$. Sample variance pertains to the finite number of modes (measurements) due to an incomplete or volume–limited survey. Shot noise dominates at small scales while sample variance dominates at large scales (of order the cube root of the survey volume) (Peebles 1980; Dodelson 2003; Weinberg et al. 2013). The optimal number density of galaxies (n) is related to the bias by

$$n \sim \frac{1}{P_g(k)} = \frac{1}{b^2 P_{cdm}(k)}. \tag{1.2}$$

where $P_{cdm}(k)$ is evaluated at roughly the BAO scale. Eqn. 1.2 shows that a small sample of relatively high–bias galaxies (e.g., LRGs) is just as good as a large sample of relatively low–bias galaxies (e.g., ELGs).

1.3.3 Measuring $H(z)$ and $d_A(z)$

Galaxy surveys use imaging and spectroscopic data to measure the BAO signal in the radial (line–of–sight) and tangential (angular) directions, respectively. Fig. 1.3 illustrates that this is similar to measuring the diameter of a sphere since the BAO signal is 3–dimensional. The radial direction provides a direct measurement of the Hubble parameter, $H(z)$, as

$$H(z) = \frac{c\Delta z}{s_{\parallel}}, \tag{1.3}$$

where Δz is what one is measuring (the redshift extent of the BAO signal), c is the speed of light, and $s_{\parallel} \sim 150$ Mpc is the comoving size of the BAO signal parallel to the line of sight. The tangential direction provides a direct measurement of the angular diameter distance, d_A, as

$$d_A(z) = \frac{s_{\perp}}{\Delta\theta(1+z)}, \tag{1.4}$$

where $\Delta\theta$ is what one is measuring (the angular extent of the BAO signal), z is the median redshift of the galaxy sample, and $s_{\perp} \sim 150$ Mpc is the comoving size of the BAO signal perpendicular to the line of sight. $H(z)$ represents how fast the universe is expanding relative to its size, while $d_A(z)$ is the physical distance between two points separated by an angle θ as a function of redshift. The simplicity of Eqns. 1.3 and 1.4 is one of the benefits of measuring such a large scale feature since it is not compromised by nonlinear effects (Eisenstein et al. 2007; Sherwin & Zaldarriaga 2012). The comoving size of the BAO signal was determined $380,000$ years after the Big Bang so galaxy surveys need only measure how large the signal appears in redshift space (Δz) or in the plane of the sky ($\Delta\theta$).

The ΛCDM cosmological model relates $H(z)$ and $d_A(z)$ to parameters describing the expansion history of the universe, so measuring Δz and $\Delta\theta$ constrains these parameters. If neutrinos are massless, the Hubble parameter is given by (Bassett & Hlozek 2010; Weinberg et al. 2013),

$$H(z) = H_0\sqrt{\Omega_m(1+z)^3 + \Omega_r(1+z)^4 + \Omega_K(1+z)^2 + \Omega_{DE}f(z)}, \tag{1.5}$$

where z is redshift, H_0 is the present day Hubble parameter, $\Omega_m, \Omega_r, \Omega_K$, and Ω_{DE} are the present day matter, radiation, curvature, and dark energy density parameters in units of the critical density, and $f(z)$ encodes the evolution of the dark energy density with redshift. The angular diameter distance depends on the integral of the Hubble parameter, as

$$d_A(z) = \frac{c}{H_0(1+z)\sqrt{-\Omega_K}} \operatorname{sinn}\left(H_0\sqrt{-\Omega_K}\int_0^z \frac{dz'}{H(z')}\right), \tag{1.6}$$

where sinn() is sin() for a spatially closed ($\Omega_K < 0$) universe and sinh() for an open ($\Omega_K > 0$) universe. Table 1.3.3 lists the galaxy surveys and galaxy samples that have detected the BAO
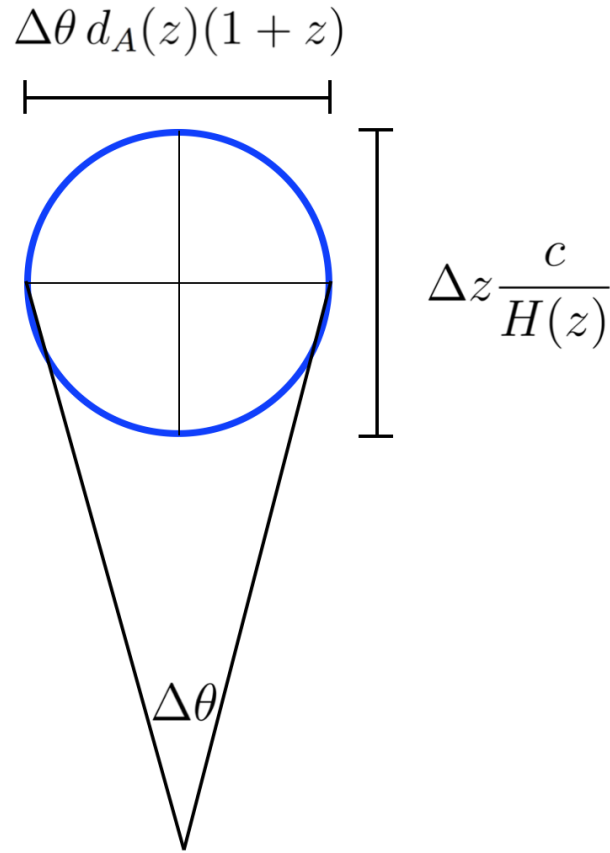
Figure 1.3: The BAO signal can be measured in both the radial (Δz) and tangential ($\Delta\theta$) directions. Reproduced from Bassett & Hlozek (2010).

signal along with their measurement uncertainties on $H(z)$ and $d_A(z)$. For simplicity, the first generation of galaxy surveys measured the spherically averaged combination of $H(z)$ and $d_A(z)$, the dilation scale (d_V),

$$d_V(z) = \left(\frac{d_A(z)^2 cz}{H(z)}\right)^{1/3}, \tag{1.7}$$

instead of $H(z)$ and $d_A(z)$ (Eisenstein et al. 2005; Bassett & Hlozek 2010), so the first few rows of Table 1.3.3 only have $d_V(z)$. The galaxy surveys include the Sloan Digital Sky Survey (SDSS–II, York et al. 2000; Eisenstein et al. 2005; Percival et al. 2010), 6–degree Field Galaxy Survey (6dFGS, Colless et al. 2001a; Beutler et al. 2011), WiggleZ Dark Energy Survey (WiggleZ, Drinkwater et al. 2010; Blake et al. 2011a,b), Baryon Oscillation Spectroscopic Survey (SDSS–III/BOSS, Dawson et al. 2013; Gil-Marín et al. 2015; Delubac et al. 2015; Beutler et al. 2014, 2016), extended Baryon Oscillation Spectroscopic Survey

(SDSS–IV/eBOSS, Dawson et al. 2016), and the Dark Energy Spectroscopic Instrument (DESI, DESI Collaboration 2016a).

myPapers

1.3.4 The Legacy Surveys

The Legacy Surveys[4] (Dey et al. 2018) are a cosmological survey of 14,000 deg^2 of sky in the g, r, and z–bands that is 1–2 magnitudes deeper than the SDSS. It is a combination of three surveys: the DECam Legacy Survey (DECaLS), the MOSAIC3 z–band Legacy Survey (MzLS), and the Beijing–Arizona Sky Survey (BASS). DECaLS uses the 4–m Blanco telescope and DECam[5] camera at Cerro Tololo, Chile, MzLS uses the 4–m Mayall telescope and MOSAIC3[6] camera at Kitt Peak, AZ, and BASS uses the 2.3–m Bok telescope and 90Prime[7] camera at Kitt Peak, AZ. Fig. 1.4 shows the CCD layout, pixel scale, and g, r, and z total system throughput for the three cameras. DECaLS, MzLS, and BASS images are publicly available within 1–2 days of observation and large–scale–structure catalogs are publicly released every $\sim$ 6 months.

The primary purpose of the Legacy Surveys is to provide galaxy targets for the Dark Energy Spectroscopic Instrument (DESI, see § 1.4), but they will have vast scientific impact in astronomy on their own. The g, r, z–band image quality is better than both the SDSS and the Panoramic Survey Telescope and Rapid Response System 1 (Pan–STARRS 1, or PS1) 3π Survey (Chambers et al. 2016), and the footprint spans the SDSS footprint, which improves the utility of existing spectroscopic and imaging data. Examples of high–impact science that the Legacy Surveys enables are studies of the Milky Way's stellar halo similar to Nidever et al. (2012) a 10–year time baseline with SDSS to measure proper motions of Galactic halo stars 2 mags fainter than Gaia's detection limit (Palanque-Delabrouille et al. 2011; Gaia Collaboration et al. 2016b); statistical studies of the stellar populations in Local Group galaxies (D'Souza & Bell 2018); new probes of the evolution of the intergalactic medium (IGM) and galaxy clusters and halos (Pilachowski et al. 2012); additional epochs of WISE infrared data for variable sources, such as high redshift quasars or Active Galactic Nuclei (AGN) (Meisner et al. 2017); and forced photometry of other lower–resolution imaging data such as the Palomar Observatory's PTF, iPTF, or future ZTF programs.[8]

---

[4]http://legacysurvey.org

[5]http://www.ctio.noao.edu/noao/content/DECam-Observing-Manual

[6]http://www.noao.edu/kpno/mosaic/manual/

[7]http://cameras.itl.arizona.edu/index.html?90Prime.html

[8]https://www.ptf.caltech.edu

Table 1.1: Galaxy Survey Measurements of $H(z)$ and $d_A(z)$

Survey	Sample	Redshift (Median)	σ_{d_A}/d_A (%)	σ_H/H (%)	σ_{d_V}/d_V (%)	Number of Measurements
SDSS–II	Main	0.2	–	–	3.4	1
SDSS–II	LRG	0.35	–	–	1.9	1
6dFGS	6dFGS	0.1	–	–	4.5	1
WiggleZ	ELG	[0.44, 0.73]	–	–	[4.7, 7.8]	3
SDSS–III	LOWz	0.38	1.6	2.9	1	1
SDSS–III	CMASS	0.61	1.5	2.3	0.88	1
SDSS–III	QSO–Lyα	2.34	5.8	3.2	2	1
eBOSS	LRG	0.72	1.2	2.1	0.8	1
eBOSS	ELG	0.87	3.1	4.7	2	1
eBOSS	QSO–tracers	[0.9, 2.1]	2.8	4.2	1.8	1
eBOSS	QSO–Lyα	[2.1, 3.5]	1.4	1.7	1	1
DESI	BGS	[0.05, 0.45]	[1.32, 6.12]	[2.44, 12.10]	[0.91, 4.33]	5
DESI	LRG	[0.65, 0.95]	[0.69, 0.82]	[1.22, 1.50]	[0.47, 0.57]	4
DESI	ELG	[0.65, 1.55]	[0.69, 1.90]	[1.22, 2.52]	[0.47, 1.16]	10
DESI	QSO–tracers	[0.95, 1.96]	[0.73, 4.71]	[1.22, 6.39]	[0.49, 2.92]	10
DESI	QSO–Lyα	[2.12, 3.55]	[1.95, 15.91]	[1.99, 8.89]	[1.02, 5.72]	10

Note. — Measurements of d_A and H are provided when possible. Brackets denote a closed range of values. The eBOSS and DESI measurement uncertainties are the forecasted values. Reconstruction was performed in making the SDSS–II LRG, SDSS–III LOWz and CMASS, eBOSS and DESI measurements. The reported measurements are from:
(SDSS–II Main): Percival et al. (2007),
(SDSS–II LRG): Padmanabhan et al. (2012),
(6dFGS): Beutler et al. (2011),
(WiggleZ): Blake et al. (2011a),
(SDSS–III LOWz): Beutler et al. (2016),
(SDSS–III CMASS): Beutler et al. (2016),
(SDSS–III QSO–Lyα): Delubac et al. (2015),
(eBOSS): Dawson et al. (2016),
(DESI): DESI Collaboration (2016a).

1.4   The Dark Energy Spectroscopic Instrument (DESI)

1.4.1   Overview

DESI is a robotically actuated 5,000–fiber spectrograph that will make the most precise measurement of dark energy to date. It is a five–year survey with first light slated in 2019. By obtaining redshifts for tens of millions of galaxies and QSOs spanning 14,000 $\deg^2$, DESI will measure the BAO signal to sub–percent accuracy in more than ~ 30 redshift bins between $0 < z < 3.6$. This will enable a few percent measurement of w_0 and w_a, the standard parameters that describe dark energy's equation of state (see Section 1.4.2). DESI's wavelength coverage is 360 to 980 nm at a resolution $R = \lambda/\Delta\lambda$ of 2000 to 5500. DESI will be installed at prime focus on the Mayall 4–m telescope in Kitt Peak, Arizona. For more details see DESI Collaboration (2016a,b).

Targets (galaxy samples) for DESI will be selected using the broadband optical grz imaging from the Legacy Surveys (see Section 1.3.4) and infrared imaging from the Wide–field Infrared Survey Explorer (WISE, Wright et al. 2010) using the $W1$ (3.4 μm) and $W2$ (4.6 μm) bands. DESI will use five galaxy samples to measure $H(z)$ and $d_A(z)$ in these ~ 30 redshift bins. Fig. 1.5 shows the redshift ranges for all DESI targets. Emission line galaxies (ELGs) are relatively isolated, inherently blue, disk–like galaxies with ongoing star formation. They are the faintest of all five galaxy targets and they are the majority of the sample due to their lower bias and wide redshift range. Bright galaxy sample (BGS) galaxies are similar to the SDSS main galaxy sample (MGS) but are slightly fainter in r. They are brightest DESI targets. Luminous red galaxies (LRGs) are relatively massive, inherently red, elliptical galaxies that host old stellar populations. Quasi–stellar objects (QSOs) are galaxies with a supermassive black hole at their center actively accreting gas, a process which emits enough light to outshine the entire galaxy (Mo et al. 2010). QSOs are very bright point sources so are useful tracers of clustering at high redshift. DESI QSOs will either be low redshift (z < 2.1) and used as tracers of spatial clustering (QSO–tracers) or high redshift (z > 2.1) and their spectra alone will be used to trace the clustering of matter along the line of sight (QSO–Lyα). For more details see DESI Collaboration (2016a).

1.4.2   Measuring w_0 and w_a

Dark energy is causing the universe to expand at an increasing speed (i.e. accelerated expansion). A widely adopted model for dark energy is to treat it as a fluid with equation of state $P = w(z)\rho$, where P is pressure, ρ is density, and $w(z)$ is given by the Chevallier–Polarski–Linder (CPL) parameterization (Chevallier & Polarski 2001; Linder 2003),

$$w(z) = w_0 + w_a \frac{z}{1+z}. \tag{1.8}$$

This parameterizes our ignorance about the physics of dark energy as w_0, the present value of dark energy's equation of state, and w_a, its behavior in the past. A universe with a

cosmological constant corresponds to $w_0 = -1, w_a = 0$. Substituting Eqn. (1.8) into the continuity equation,

$$\frac{\partial \rho}{\partial t} + \nabla \cdot (\rho \mathbf{v}), \tag{1.9}$$

where $\mathbf{v}$ is the velocity of the fluid, gives

$$f(z) = (1+z)^{3(1+w_0+w_a)} \exp\left(-3w_a \frac{z}{1+z}\right), \tag{1.10}$$

which renders $H(z)$ and $d_A(z)$ (Eqns. 1.3 and 1.4) functions of w_0 and w_a.

By studying the CMB, one can measure (among other parameters) the size of the BAO signal, $\Omega_m h^2$, and $\Omega_b h^2$, where $h = H_0/100$ km s^{-1} Mpc^{-1}. We are "in the golden age of astronomy" because Planck has measured these parameters to sub–percent precision (Planck Collaboration 2016); however, Ω_m is degenerate with H_0 while Ω_K is degenerate with w, so additional data is needed to measure these four parameters. Direct measurement of $H(z)$ and $d_A(z)$ breaks the Ω_K–w degeneracy, so marginalizing over all other cosmological parameters (a.k.a. adopting Planck priors) constrains w_0, w_a, and Ω_K. Combining Planck and current BAO measurements, such as from BOSS, measure w_0 and w_a to ~ 10 percent precision (Anderson et al. 2014; Weinberg et al. 2013).

The Dark Energy Task Force figure of merit (DETF FoM) quantifies the accuracy of w_0 and w_a measurements as inversely proportional to the area of the standard error ellipse in the w_0–w_a plane (Albrecht et al. 2006; DESI Collaboration 2016a). Larger FoM is better. Fig. 1.6 shows the forecasted 68th percentile constraints on the maximum likelihood estimates of w_0 and w_a for DESI, using Planck priors. The baseline DESI measurement (green) has a FoM more than 3 times larger than the final BOSS measurements do (blue). Including the galaxy broadband power spectrum, with a maximum mode (k_{max}) in the range $0.1 \leq k_{max} \leq 0.2h$ Mpc^{-1}, increases the FoM by a factor of 2 to 4. For more details see Dodelson (2003); Bassett & Hlozek (2010); Anderson et al. (2014); Albrecht et al. (2006); DESI Collaboration (2016a).

1.4.3 Challenges

DESI is trying to measure $H(z)$ and $d_A(z)$ to sub–percent accuracy, so its success depends on how well the angular and redshift selection functions (at least percent–level systematics) are understood. My thesis meets this challenge by presenting the first end–to–end method for modeling the DESI angular selection function, beginning with raw images and ending with target selection from a large–scale–structure catalog.

A major challenge for DESI is understanding the inevitable biases and systematics in its galaxy samples because the Legacy Surveys require a joint analysis of three telescopes' data. Repeat and multi–band images of the same part of the sky is done over month to year time

scales and all three cameras (see Fig. 1.4) have similar size to the BAO signal (∼5 deg. on the sky at redshift 1). In addition, DECaLS, MzLS, and BASS have different electronics, mountaintop conditions, and observing strategies (see Zou et al. 2017 and Chapter 2).

1.5   Objectives

In Chapter 2, I discuss the observing strategy for DECaLS and MzLS and our novel use of dynamic exposure times. Chapter 3 extends the dynamic exposure time analysis to determine the implications for the Zwicky Transient Facility (ZTF) and the Large Synoptic Survey Telescope (LSST). In Chapter 4, I introduce a Monte Carlo method, called `Obiwan`, that adds simulated sources to random locations in astronomical images and then performs source detection and measurement, characterizing the complex selection inherent in large–scale–structure catalogs. My dissertation concludes with Chapter 5, where I present a new method for removing imaging systematics from clustering statistics and use `Obiwan` to carry out this method for the eBOSS ELG sample.
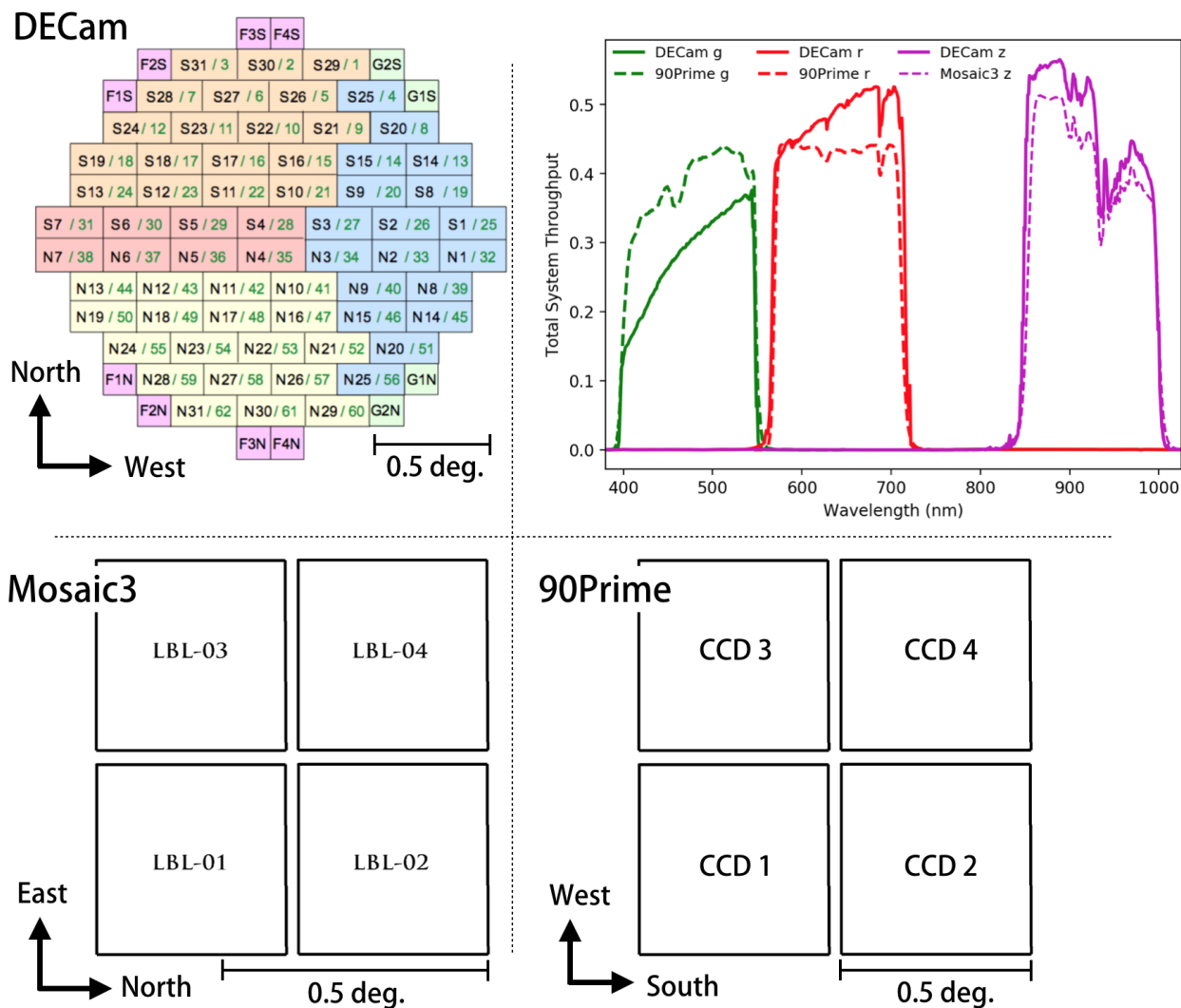
Figure 1.4: The DECam, Mosaic3, and 90Prime cameras. (Top Left, Bottom) DECam has 62 CCDs with pixel 0.262″ per pixel, while Mosaic3 and 90Prime have 4 CCDs with pixel scales of 0.260 and 0.455″ per pixel. See Table 2.4.1 for more info. Reproduced from the DECam,[5] Mosaic3,[6] and 90Prime[7] manuals. (Top Right) The total system throughput in g, r, and z–band for each camera. Reproduced from (Dey et al. 2016a).
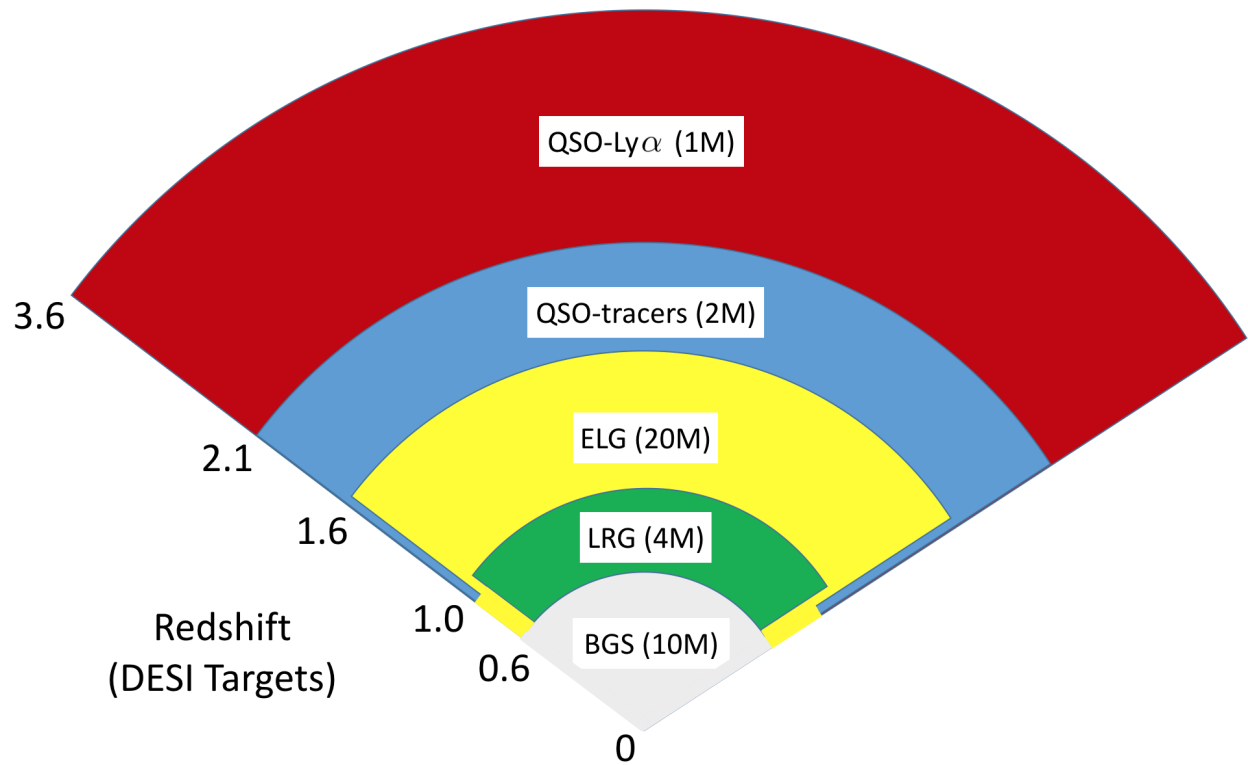
Figure 1.5: The total number of each DESI target and their redshift ranges. Colored regions correspond to the redshift range not to the imaging footprint (i.e. all targets have the same footprint). For example, ELGs have redshift $0.6 < z < 1.6$ and QSO–tracers have redshift $0.9 < z < 2.1$.
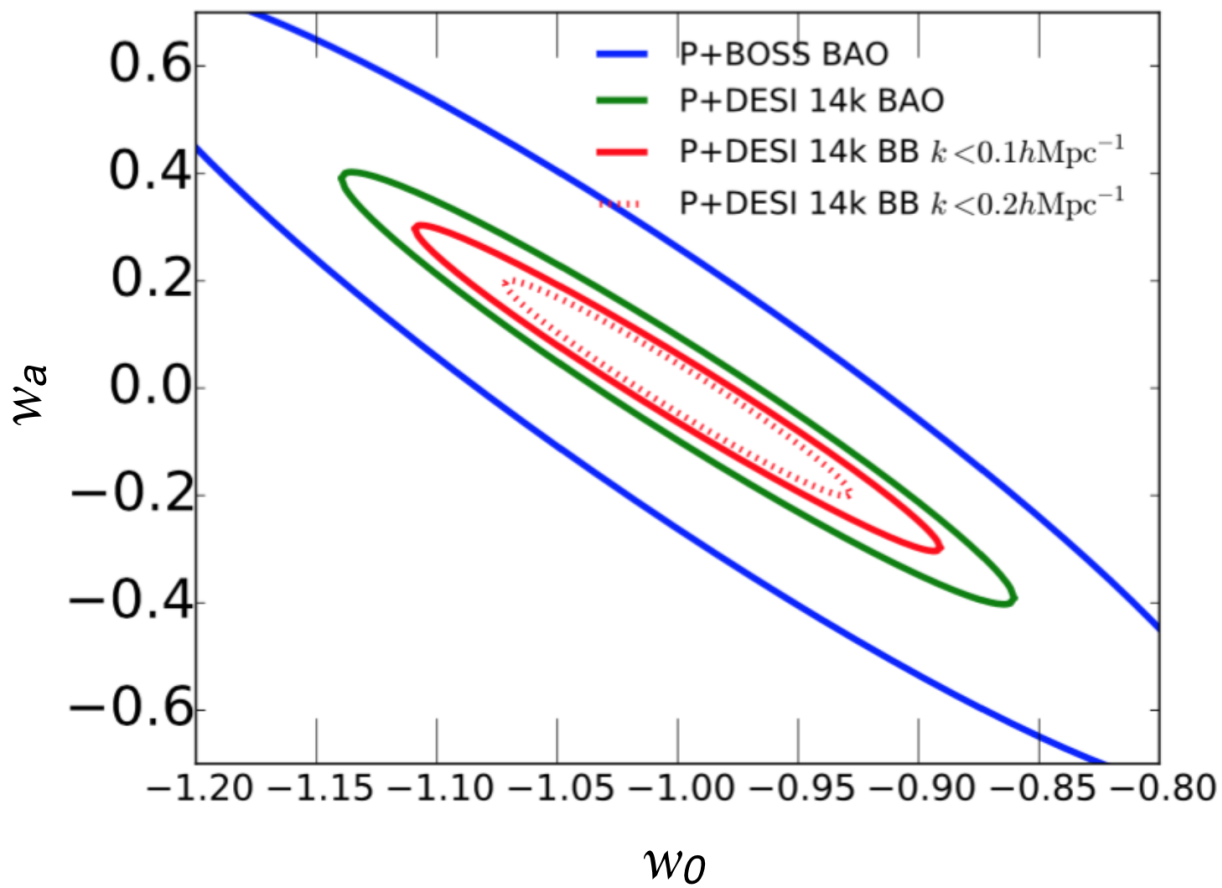
Figure 1.6: Forecasted 68th percentile constraints on the maximum likelihood estimates of w_0 and w_a for DESI, using Planck priors. The baseline DESI survey (green) has a FoM more than three times larger than the final BOSS survey (blue), i.e. the area inside the green curves is more than 3 times smaller than the area inside the blue curve. Reproduced from (DESI Collaboration 2016a).

Chapter 2

Observing Strategy for the Legacy Surveys

The work in this Chapter is in preparation and will be published as Burleigh et al. (2018a in prep.).

2.1 Chapter Abstract

The Legacy Surveys are a group of three imaging surveys mapping $\approx$14,000 deg^2 in three optical bands (g, r, and z) to a depth $\approx$ 1–2 mag deeper than the Sloan Digital Sky Survey (SDSS). One of the major challenges of past wide–field imaging surveys is the uneven depth that results from varying observing conditions that plague ground–based observatories. We present the mapping and observing strategy for two of the three surveys (the Dark Energy Camera Legacy Survey, or DECaLS; and the Mayall z–band Legacy Survey, or MzLS), both of which employ a unique strategy to dynamically adjust the exposure times as rapidly as possible (every 2–3 minutes for these two surveys) in response to the changing observing conditions. The goal is to achieve perfect exposure times (i.e., exposing precisely long enough to reach depth), but any improvement in depth uniformity allows for better control of clustering systematics. Using our astrometric and photometric calibration code `LegacyZpts`, we estimate that achieving perfect exposure times with DECaLS and MzLS would save about 23% and 12% of the telescope time compared to traditional fixed exposure times. This is an enormous effect. Naively extrapolating to the DESI (spectroscopic) survey, the average savings of 18% in telescope time corresponds to 0.9 years. We also investigate systematics in our astrometric and photometric calibrations, and compare DECaLS and MzLS per–exposure depths to the DESI requirements.

2.2   Introduction

The Legacy Surveys[1] (Dey et al. 2018) are a combination of three imaging surveys aiming to map 14,000 deg^2 in the north and south galactic caps in three optical bands (g, r and z) to depths ≈1–2 mag deeper than the Sloan Digital Sky Survey imaging (SDSS, Abazajian et al. 2009). The three surveys that make up the Legacy Surveys are: the DECam Legacy Survey (DECaLS); the Mayall z–band Legacy Survey (MzLS); and the Beijing–Arizona Sky Survey (BASS). DECaLS uses the Blanco 4–m telescope and Dark Energy Camera (Flaugher et al. 2015)[2] located at Cerro Tololo, Chile; MzLS uses the Mosaic3 camera (Dey et al. 2016b) at the Mayall Telescope located at Kitt Peak in Arizona;[3] and BASS uses the Bok 2.3–m telescope/90Prime camera on Kitt Peak.[4] BASS and MzLS cover the same area but in different bands.

The primary purpose of the Legacy Surveys is to provide targets for the Dark Energy Spectroscopic Instrument (DESI, DESI Collaboration 2016a,b). DESI is a robotically actuated 5,000–fiber spectrograph that will survey 14,000 deg^2 of sky in order to make a Stage–IV (sub–percent accuracy) measurement of dark energy. Spectra of more than 30 million galaxies and quasars will be obtained over this five–year survey. DESI's wavelength coverage is 360 to 980 nm at a resolution, $R = \lambda/\Delta\lambda$, of 2000 to 5500. DESI is currently in the process of being installed at prime focus on the Mayall 4–m telescope in Kitt Peak, Arizona and should see first light in mid–2019.

In addition to providing targets for DESI, the Legacy Surveys will dramatically improve the utility (e.g., cross–correlations) with existing spectroscopic and imaging datasets, as they are 1.5–2 mag deeper and have better image quality than either SDSS or the Panoramic Survey Telescope and Rapid Response System 1 (Pan–STARRS 1) 3π survey (Chambers et al. 2016). Existing spectroscopic datasets in the DESI footprint include the SDSS (York et al. 2000), 6dF Galaxy Survey (6dF, Jones et al. 2004), WiggleZ Dark Energy Survey (WiggleZ, Drinkwater et al. 2010); imaging datasets include the Wide–field Infrared Survey Explorer (WISE; Wright et al. 2010). Increasing g, r, and z–band depths by 1.5–2 mags increases the number of $z > 0.5$ galaxies by about a factor of 30. No currently ongoing survey is providing optical imaging to this depth or with as much overlap with northern spectroscopic surveys. For example, the Dark Energy Survey will observe $\approx$ 5,000 deg^2 of southern sky and will only overlap about 500 deg^2 of the SDSS footprint (The Dark Energy Survey Collaboration 2005; DES Collaboration 2017).

All previous ground–based wide–field imaging surveys have used fixed exposure times per band, thus resulting in survey depths that vary across the survey footprint due to both terrestrial and extraterrestrial constraints. Terrestrial constraints include the observing conditions (i.e., cloud cover, transparency, delivered image quality, sky brightness) and telescope limitations (e.g., zenith distance of observation, telescope pointing accuracy, telescope track-

---

[1]http://legacysurvey.org

[2]http://www.ctio.noao.edu/noao/content/DECam-Observing-Manual

[3]http://www.noao.edu/kpno/mosaic/manual/

[4]http://cameras.itl.arizona.edu/index.html?90Prime.html

ing accuracy, focus, etc.). Extraterrestrial constraints include the extinction due to Galactic and Solar System dust, zodiacal light, Galactic cirrus and other sources of diffuse emission, and source crowding. Cosmological surveys require a uniformity of depth over a large area (for better control of clustering systematics), and hence imaging surveys with varying depth are generally truncated to their shallowest depth when used for cosmological studies.

In this Chapter, we describe an innovative approach that we utilized for our DECaLS and MzLS observing strategy (the observing strategy for BASS is presented in Zou et al. 2017). Instead of using a fixed exposure time, we analyzed images on–the–fly in order to dynamically adjust the exposure time to ensure a near–constant depth for each image. This procedure allowed us to optimally use the available telescope time with minimal reobservation. The optimization of the surveys was particularly important given that the imaging surveys had to be completed to a minimum depth in $\sim$3 years due to the DESI construction and installation schedule.

This Chapter is split into three parts, which are organized as follows. The first part (Sections 2.3 – 2.5) presents the observing strategy for DECaLS and MzLS. In Section 2.3 we explain the Legacy Surveys' footprint and its depth requirements. Section 2.4 describes our tiling strategy. Section 2.5 explains how our observing strategy optimizes photometric calibration and image quality. The second part (Section 2.6) describes how we perform astrometric and photometric calibrations, such as computing sky brightness, seeing, photometric zeropoint, and 5σ extinction–corrected depth. The third part (Section 2.7), enabled by these calibrated data, summarizes our implementation of dynamic exposure times for DECaLS and MzLS and determines the maximum impact (e.g., telescope time saved) that our dynamic exposure times could have. We conclude in Section 2.8.

2.3 Footprint and 5σ Depth

The Legacy Surveys' footprint is shown in Fig. 2.1. The properties of each survey (telescopes, cameras, nights awarded) are shown in Table 2.3. DECaLS (magenta) spans 9,000 deg^2, while MzLS/BASS (green) spans 5,000 deg^2. There is an overlap region of 450 deg^2 at $30 <$ Dec < 34 (black), which will be used to determine biases and systematics between DECaLS and MzLS/BASS. DECaLS inherits data from the Dark Energy Survey (DES, The Dark Energy Survey Collaboration 2005). This region is show in yellow; the rest of the DES footprint is red. The two contiguous regions correspond to the North (NGC) and South Galactic Caps (SGC).

The 5σ AB magnitude DESI depth requirement for the Legacy Surveys is (g, r, z) of (24.0, 23.4, 22.5) magnitudes for an emission line galaxy with an exponential surface–brightness profile and a half–light radius of 0.45″ (DESI Collaboration 2016a). At least 90% of the footprint must reach this depth. Table 2.3 shows that the three–pass tiling strategy we utilize for DECaLS (see Section 2.4) covers 74% of the footprint sky with three images and 98% with two images. In order for 90% of the footprint to reach depth, DECaLS must meet the DESI requirement with just two passes. The MzLS tiling strategy (see Section 2.4)
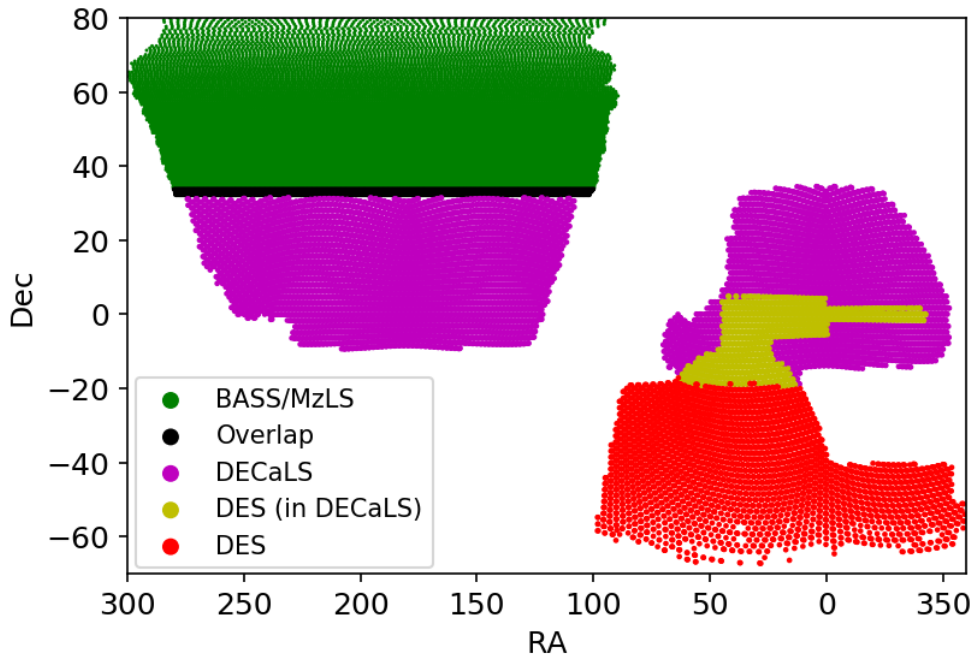
Figure 2.1: The Legacy Surveys footprint. DECaLS (magenta) spans 9,000 deg^2, while MzLS/BASS (green) spans 5,000 deg^2. There is an overlap region of 450 deg^2 at $30 < $ Dec < 34 (black), which will be used to determine biases and systematics between DECaLS and MzLS/BASS. DECaLS inherits data from DES. This region is show in yellow; the rest of the DES footprint is red. The two contiguous regions correspond to the North (NGC) and South Galactic Caps (SGC).

has higher coverage with 99.5 and 85% of the footprint sky having two and three passes, respectively, so MzLS is expected to meet the DESI requirement with three passes. This means that a single DECam exposure should be 2.5 $\log_{10}(\sqrt{2}) \sim 0.37$ AB mag shallower than the formal DESI imaging depth requirement, and a single MzLS/BASS exposure should be 2.5 $\log_{10}(\sqrt{3}) \sim 0.60$ AB mag shallower.

2.4 Tiling Strategy

2.4.1 General Concepts

Wide–field imaging surveys typically aim to cover one or more contiguous areas of sky much larger than the footprint of the imaging camera. The Legacy Surveys represent a particularly extreme case where we are attempting to image a $\approx$14,000 deg^2 region using cameras that have fields of view of 0.35–3.1 deg^2 (see Table 2.4.1). In addition, all of the camera focal planes are CCD mosaics that have gaps between individual CCDs. Hence, an

Table 2.1: The Legacy Surveys as of January 28, 2018

Telescope	Camera	Bands	Area (deg²)	Nights Awarded	Start (mm/yy)	Finish (mm/yy)	Complete %
Blanco 4–m	DECam	g, r, z	9,000	150	08/14	11/18	62
Mayall 4–m	MOSAIC3	z	5,000	240	02/16	02/18	100
Bok 2.3–m	90Prime	g, r	5,000	240	08/15	07/18	73

Table 2.2: Tiling Solutions for DECaLS and MzLS

N	DECaLS	MzLS
0	1.0000	1.0000
1	0.9998	1.0000
2	0.9801	0.9950
3	0.7443	0.8500

Note. — The DECaLS and MzLS columns are the fraction of the sky footprint having a given number of repeat exposures (N).

Table 2.3: Camera Properties

Camera	CCDs	Amplifiers (per CCD)	Pixels (per CCD)	Pixel Scale $''$ / pix	FOV (deg^2)	Fill Factor
DECam	62	2	4094×2046	0.262	3.18	0.87
Mosaic3	4	4	4079×4054	0.260	0.36	0.95
90Prime	4	4	4096×4032	0.455	1.16×1.16	0.94

Note. — FOV: Camera field of view including CCD gaps and dead CCDs. Fill Factor: Fraction of the FOV covered by CCDs.

efficient tiling pattern has to cover the entire area with as few tiles as possible, and also cover all of the CCD gaps to some minimum depth driven by the survey science requirements.

Once the basic tiling strategy was identified, we defined three independent (but equal) tilings, with each tiling offset from the other two by some prescribed amount. Three tilings ensure that the footprint is covered without any gaps, while also minimizing the amount of area that does not have at least two images at any given position. Two–pass coverage is useful both to discriminate and mask any particle events or other detector–based anomalies, and to boost signal–to–noise compared to a single pass. We used a Monte Carlo process of generating different offsets for the tiling sets for each camera in order to select the optimal offsets that maximized three–pass coverage while minimizing one–pass coverage.

The detailed implementations for each camera are described in the following two subsections.

2.4.2 Implementation for DECaLS

To define the tiling for DECaLS, we used the approach of Hardin, Sloane and Smith,[5] who considered the general problem of covering a sphere uniformly with a fixed number of points. For a camera with a field of view of a_{FoV} deg^2, the ideal tiling of the entire sky would require $N = 4\pi(180/\pi)^2/a_{\text{FoV}}$ tiles. For each of the cameras in the Legacy Surveys, we selected the pre–computed icosahedral arrangements of Hardin et al. with tiling N_{tile} that was close in number to but greater than N (i.e., the minimum number while still providing sufficient overlap with the neighboring tile).

DECam has a roughly circular field of view of 3.18 deg^2 (Flaugher et al. 2015), which implies a tiling number of $N \approx 13000$ (see Table 2.4.1). We investigated the icosahedral tilings with $N_{\text{tile}} = [15252, 15392, 15872, 16002, 16472, 16752]$ and settled on $N = 15872$ as providing the best compromise.

Passes 2 and 3 are copies of this pass 1 tiling (i.e., same N_{tile}, offset by [ΔRA,ΔDec] of [0.2917,0.0833] deg and [0.5861,0.1333] deg respectively. This solution results in fractional

---

[5]see http://neilsloane.com/icosahedral.codes/

coverage within the DESI footprint as shown in Table 2.3. Ideally, we would obtain three–image coverage of 100%, but this is not possible with a three–pass strategy given the gaps between the DECam CCDs. The resulting tiling for DECaLS is shown in Figure 2.2 along with the as–observed coverage statistics (which include pointing errors during the observations).
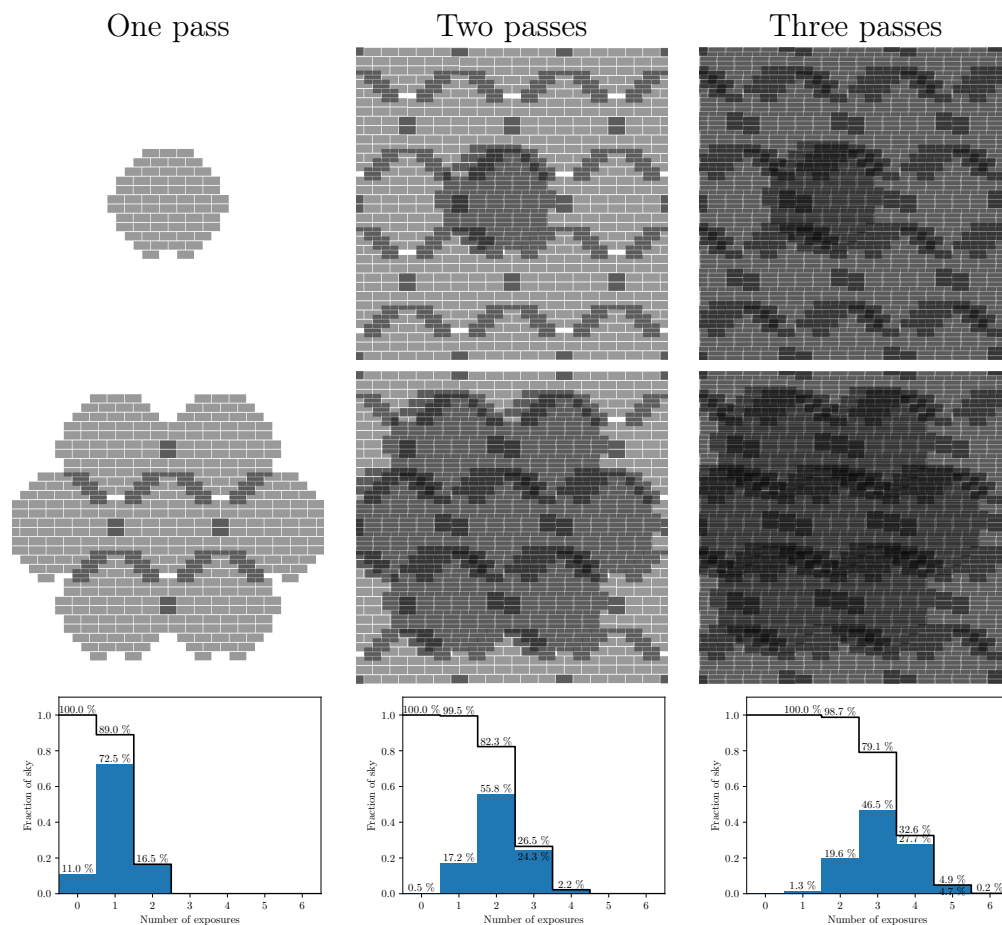
Figure 2.2: Tiling strategy in the DECaLS survey. DECam has 62 science CCDs, but during the course of the survey, one or more CCDs have been inoperative. In the example exposure shown, CCD N30 is inoperative, leaving a hole in the edge of the hexagonal footprint. The first column shows a region of sky (about 5.5° wide) covered with our "Pass 1" tiling, with a single exposure in the top row and neighboring tiles in the second row. The second and third columns show the coverage after our "Pass 2" and "Pass 3" tilings have been added, respectively. The bottom row shows the approximate coverage statistics for the entire sky.
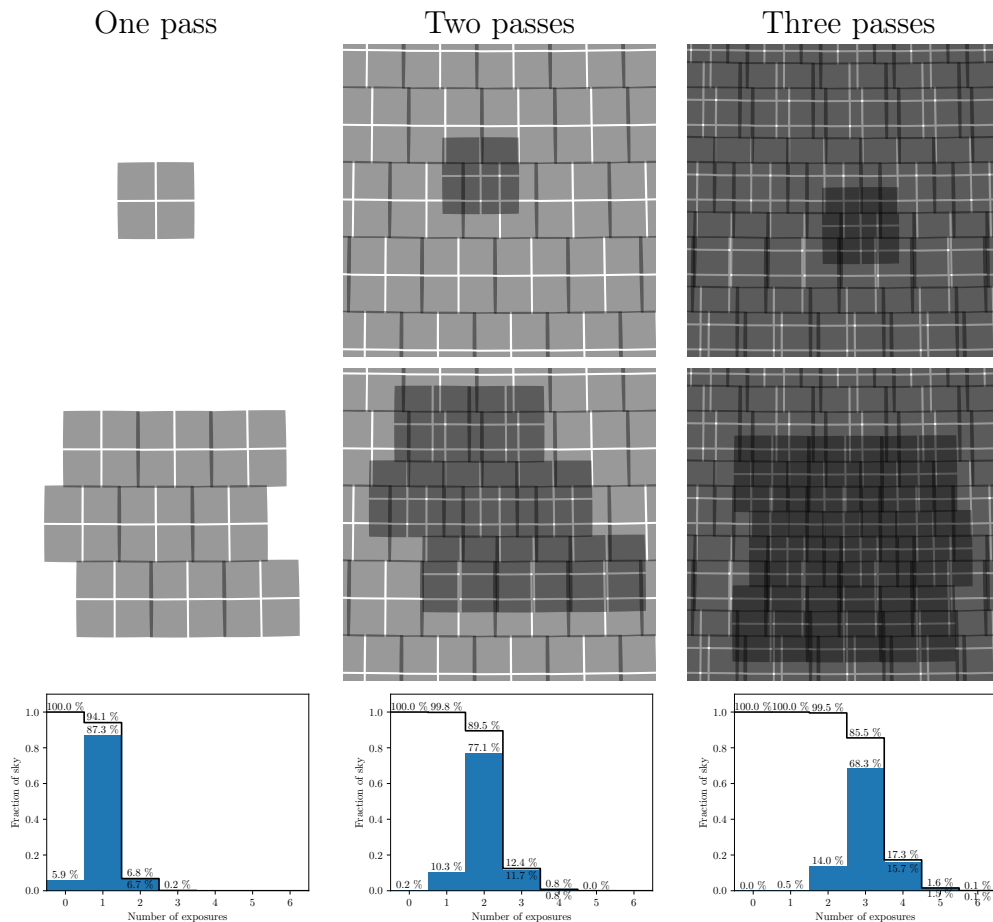
Figure 2.3: Tiling strategy in the MzLS survey. The Mosaic3 camera has 4 CCDs, each with a field of view about $0.3° \times 0.3°$, with small gaps between the CCDs. The first column shows a region of sky (about 2.5° wide) covered with our "Pass 1" tiling, with a single exposure in the top row and neighboring tiles in the second row. The second and third columns show the coverage after our "Pass 2" and "Pass 3" tilings have been added, respectively. The bottom row shows the approximate coverage statistics for the entire sky.

2.4.3   Implementation for MzLS

Mosaic3 has an approximately square on–sky footprint with a field of view of $35.89' \times 36.06'$ (Table 2.4.1; see also Dey et al. 2016b). Given the smaller size and roughly square footprint, we settled on a tiling pattern that was aligned along rows of constant declination, with adjacent frames separated by a distance that ensures overlap on all four sides. The resulting map has 122,765 tile centers in a single pass. The tiling for MzLS is shown in Figure 2.3 along with the as–observed coverage statistics.

2.5 Observing Strategy

2.5.1 Optimizing for Photometric Calibration and Image Quality

Three passes, each a complete tiling of the footprint, were chosen to maximize the scientific uniformity, image quality, and utility of the survey. In order to ensure that a given survey could be photometrically calibrated, we reserved the first tiling of the footprint (hereafter "Pass 1") for times with photometric conditions when the seeing was good (i.e., $<1.3''$). We reserved the second tiling (defined as "Pass2") for times with *either* photometric conditions *or* good seeing. We reserved the third tiling ("Pass 3") for times when neither of these conditions were met. This strategy was designed to ensure that every point within the survey footprint had at least one image that could be photometrically calibrated, and at least one image that had good seeing.

2.5.2 Optimizing the Nightly Plan

As much as possible, we scheduled observations during bright time (i.e. when the Moon was above the horizon, or the Sun's altitude was between -10 deg and -15 deg) in z–band and reserved dark time for g and r because the sky is brightest in g and r. With these constraints on the Sun and Moon imposed, dark time and bright time observations were then planned independently.

In addition, at all times, we restricted observations to airmass ≤ 2.4 and to pointings that were separated from the Moon by at least 40 deg to 50 deg, with the exact separation determined by the Moon's phase. We also avoided placing bright planets within 1.2 deg of our observed fields. We used minimum and maximum exposure times in the ranges g [56,175], r [40, 125], and z [80,250] sec. The minimum exposure times ensure that we achieve depth without wasting extra time when observing conditions were excellent, while the maximum exposure time prevents saturation and curtails long exposures when conditions were bad.

The basic logic is as follows:

1. Collate lists of unobserved tiles and tiles with bad exposures.

2. Rank order tiles by RA and split unobserved tiles by filter.

3. Remove tiles that are too close to the median position of the Moon and planets (Mars – Neptune) over the night.

4. Rank order the list of future observing nights, starting with the desired night, by Local Mean Sidereal Time (LMST) and then split each night into 1–minute–spaced moments in LMST.

5. Split the LMST list into dark and bright time.

6. Assign each tile to a particular time and night by matching the rank–ordered RA and LMST lists and minimizing the time difference between them. Do this for bright and dark time, respectively.

7. Retain LMSTs that are within 5 deg of each RA.

8. Use an annealing process to reduce the total airmass of the observations: Randomly swap the LMST of two tiles. Accept the new positions if the total airmass is reduced. Repeat 400 times.

9. *For DECaLS only*: Prioritize the tiles for building that night's plan. Observations are chosen preferentially at declinations near dec = 0, with a penalty of $1/100.0$ per deg away from the equator. Also prioritize selecting tiles near the last observation, with a penalty of $1/10.0$ per deg for distances more than 2 deg away. Priorities are doubled for observations of tiles that have been previously observed in at least one other filter. Increase priority for observations of the same tile. This should preferentially schedule pairs of $g + r$ exposures in dark time. Priorities set to 0 for tiles within 1.20 deg of Mars–Neptune.

10. Build the plan for the night. If run out of Pass 1 tiles, use Pass 2 tiles. If run out of Pass 2 tiles, use Pass 3.

11. Observations begin and end at 12 deg twilight for DECaLS, and 10 deg for MzLS.

12. The "untangling" process. Reduce slews by splitting tiles into blocks (consecutive tiles having slews > 5 deg) and then trying all permutations of the blocks. After this the tiles are split again, using blocks of 8 consecutive tiles, and the best permutation is chosen.

13. Create a list of reserve tiles for bright and dark time from the list of observed and unobserved tiles that are closest to transit and sufficiently far from the Moon and planets.

14. Observe tiles at their assigned LMST.

2.6   Astrometric and Photometric Calibration

We now describe how we compute per–CCD astrometric and photometric statistics, using our `LegacyZpts` code.[6]   This is a pre–processing step for our image reduction pipeline. `LegacyZpts` does not use the raw images from each telescope, but the calibrated versions provided by the NOAO Community Pipeline (`CP`) code (Valdes et al. 2014). Figs. 2.4 – 2.14 were made using all DECaLS and MzLS exposures through May 22, 2017 and September

---

[6]https://github.com/legacysurvey/legacyzpts

27, 2017, respectively. The median of each statistic, and its fiducial value assumed before the DECaLS or MzLS programs began, are listed in Table 2.6. Additionally, Table A.2 gives the read noise and coefficients for atmospheric and galactic extinction we used.

2.6.1 Sky Background

DECam and Mosaic3/90Prime CP images have units of ADU and e-/sec, respectively. The `LegacyZpts` code converts all images to e- so that all CCD statistics share the units shown in Table 2.6, independent of camera. Each statistic is computed for all CCDs. The sky level ($N_{\mathrm{sky,\,e-}}$) and sky RMS (σ_{sky}) are determined from the central 1000×1000 pixels of each CCD, after sigma clipping. $N_{\mathrm{sky,\,e-}}$ is the median and is subtracted from the image. σ_{sky} is the standard deviation about the sky level, which is the per–pixel Poisson noise in the sky dominated limit. Sky brightness (m_{sky}) is then,

$$m_{\mathrm{sky,AB}} = -2.5 \log_{10} \left(\frac{N_{\mathrm{sky,\,e-}}}{t_{\mathrm{exp}} P_{\mathrm{sc}}^2} \right) + ZP_0, \tag{2.1}$$

where P_{sc} is the pixel scale (arcsec / pixel) and ZP_0 is our camera– and band–dependent fiducial zeropoint (see Table 2.6). ZP_0 was determined from a photometric night at the beginning of the survey and is the AB magnitude of a source for which the camera detected 1 e-/sec on that night. Fig. 2.4 shows the Probability Distribution Functions (PDFs) of m_{sky} for DECaLS and MzLS. A PDF is defined so that area under the curve represents the fraction of the sample in that region. In this case, the total area under the curve is one.

The median z–band sky being brighter for DECaLS than MzLS (roughly by 0.6 AB mag / arcsec^2) does not imply that KPNO is darker than CTIO. The brighter sky is at least partially an observing strategy effect: DECaLS only uses z–band when the moon is up, while MzLS uses z–band regardless.

Next we use the Python package `Photutils` (Bradley et al. 2017) to perform aperture photometry on the sky–subtracted image.

2.6.2 Source Detection

We detect sources by cross correlating the image with a 2–dimensional Gaussian that has a FWHM of 5 pixels, (a "matched filter") and flagging pixels with S/N $\geq 10\,\sigma_{\mathrm{sky}}$. Aperture photometry is carried out for these (unresolved or "star–like") sources using an aperture with diameter $7''$ (constant pixel scale) and a sky annulus with diameter 14–$20''$ (constant pixel scale). The source counts ($N_{\mathrm{e-}}$) are then counts in the object aperture minus the mode of sky annulus times the area of the object aperture. In AB magnitudes this is

$$m_{\mathrm{AB}} = -2.5 \log_{10} \left(\frac{N_{\mathrm{e-}}}{t_{\mathrm{exp}}} \right) + ZP_0. \tag{2.2}$$

where t_{exp} is the exposure time. The following restrictions are applied to ensure a clean sample of sources:

Table 2.4: CCD Statistics

Statistic	Symbol	Units	DECam g	DECam r	DECam z	MOSAIC3 z
Zeropoint	ZP	e-/sec	26.55	26.76	26.37	26.25
Zeropoint (fiducial)	ZP_0	e-/sec	26.610	26.818	26.484	26.552
Sky Brightness	m_{sky}	AB mag/arcsec^2	21.81	20.80	18.61	19.22
Sky Brightness (fiducial)	$m_{sky,0}$	AB mag/arcsec^2	22.04	20.91	18.46	18.46
Seeing	FWHM	arcsec	1.29	1.19	1.09	1.07
Seeing (fiducial)	$FWHM_0$	arcsec	1.3	1.3	1.3	1.3
Airmass	X	–	1.29	1.32	1.37	1.06
Airmass (fiducial)	X_0	–	1.3	1.3	1.3	1.3
Sky Level	$N_{sky,e-}$	e-/sec/pixel	5.71	17.53	97.00	58.95
Sky RMS	σ_{sky}	e-/sec/pixel	0.27	0.50	0.95	0.76
Transparency	T_{rel}	–	1.00	0.99	0.92	0.76
RA Offset	raoff	arcsec	−0.03	−0.01	−0.00	0.01
Dec Offset	decoff	arcsec	−0.10	−0.11	−0.11	−0.00

Note. — Median quantities for each band and camera. Upper quantities are compared to their fiducial values. Lower quantities don't have fiducials.
Transparency: the fraction of light that penetrates the Earth's atmosphere relative to a good night at the start of the survey (i.e., relative atmospheric transparency).
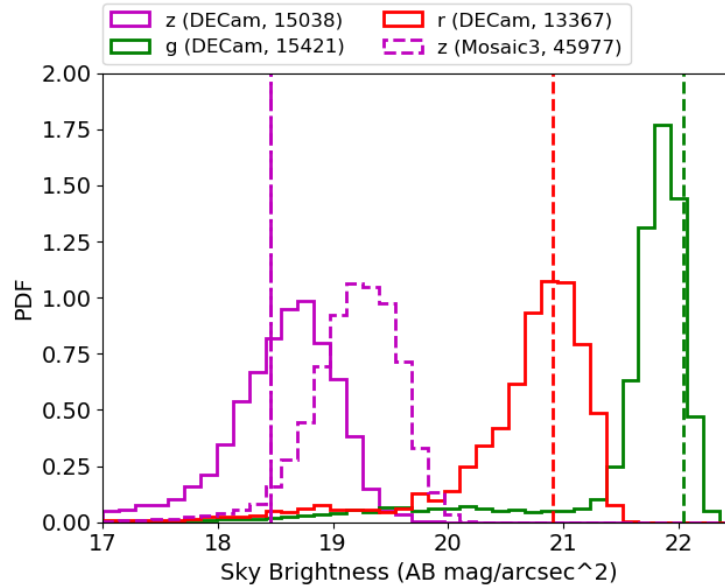
Figure 2.4: Sky brightness for DECaLS (solid) and MzLS (dashed). The fiducial values from Table 2.6 are the vertical lines, dashed (DECaLS) and dot–dashed (MzLS). The number of exposures is shown in the the legend.

- $N_{e^-} > 0$.

- $12 < m_{AB} < 22$.

- at least $11''$ from CCD edges and other sources.

- no bad pixels within 5 pixels of the centroid.

We estimate the FWHM by fitting a circular 2–dimensional Gaussian to all sources with $10 < S/N < 100$, where noise includes both the Poisson noise from sky and from the source. Only the FWHM is allowed to vary. The FWHM we record is the median of the best–fit FWHM values. Note, the standard deviation of a Gaussian with FWHM, (σ_{see}), is $\sigma_{see} = FWHM/\sqrt{8\ln 2} \approx FWHM/2.35$. Fig. 2.5 shows the FWHM and airmass distributions for DECaLS and MzLS. In z–band, the median seeing is nearly the same for DECaLS and MzLS, but the median airmass is about 25% lower for MzLS (1.37 versus 1.06).

2.6.3 Photometry

We compute photometric zeropoints relative to the PS1 catalogs, and astrometric offsets from the Gaia DR1 catalogs (Gaia Collaboration et al. 2016b,a). We use a single PS1–Gaia catalog, created using a $1''$ matching radius. Due to gaps in Gaia DR1 survey coverage, some
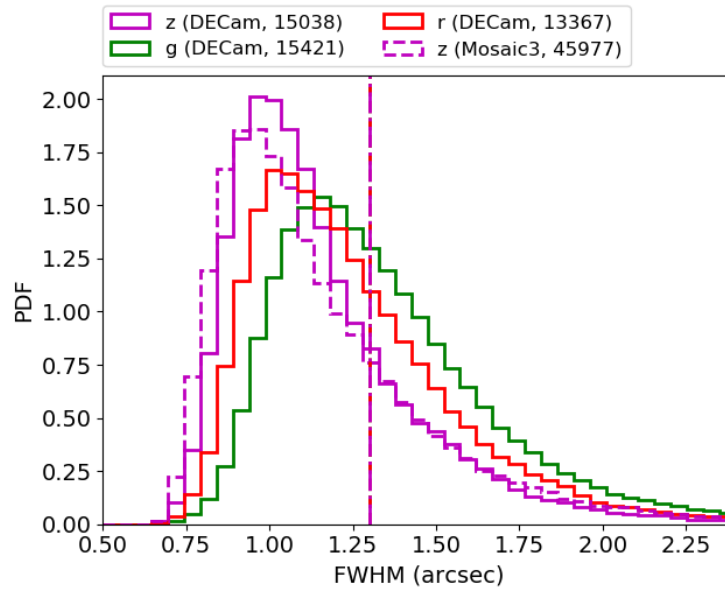
(a)
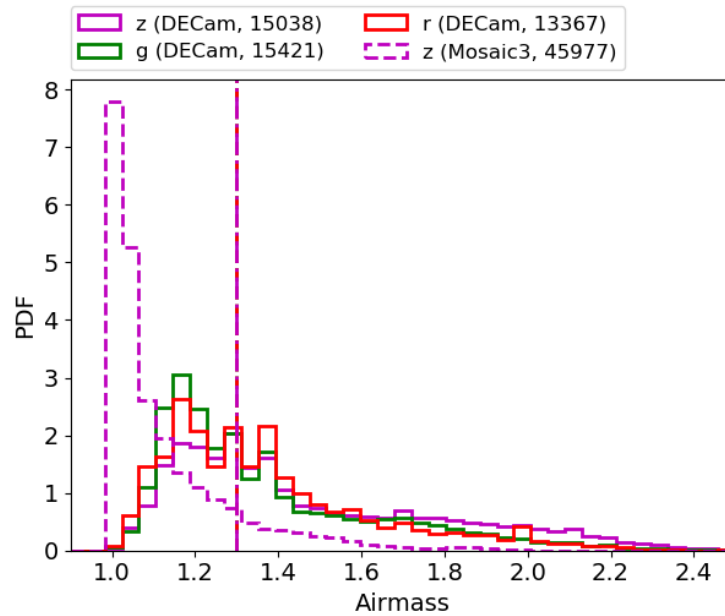
(b)

Figure 2.5: Seeing and airmass distributions. (Top) Seeing for DECaLS (solid) and MzLS (dashed). All cameras and bands have the same fiducial seeing of 1.3″. (Bottom) Airmass for DECaLS (solid) and MzLS (dashed). All cameras and bands have the same fiducial airmass of 1.3.

regions have almost no Gaia stars but plenty of bonafide PS1 star. Our astrometry falls back
to PS1 in these regions. We apply to the following cuts to the PS1–Gaia catalog:

- exactly 1 match the PS1 catalog

- the PS1 catalog indicates that at least one measurement of the source, in each g, r,
  and z–band, occurred during good conditions (i.e., in a good part of the CCD and on
  a photometric night)

- stellar color: $0.4 < g - r < 2.7$

where the $g - r$ is the PS1 median PSF magnitude color.

The instrumental zeropoint is the median absolute deviation (MAD) of the differences
between the PS1 magnitude (m_{PS1}) and our measured aperture magnitude (m_{AB}) for each
source in the CCD,

$$ZP = \mathrm{Med}\,(m_{\mathrm{PS1}} - m_{\mathrm{AB}}) + ZP_0. \tag{2.3}$$

The PS1 to DECam color correction is described in Section A.1. ZP_0 is a band–dependent
fiducial zeropoint we obtained during nights with excellent conditions near the start of DE-
CaLS and MzLS observations. It is related to the fraction of light that penetrates the Earth's
atmosphere relative to a good night at the start of the survey (the relative atmospheric trans-
parency),

$$T_{\mathrm{rel}} = 10^{-0.4[ZP_0 - ZP - K(X-1)]}, \tag{2.4}$$

where K is the atmospheric extinction coefficient. Figs. 2.6 and 2.7 show the zeropoint and
relative atmospheric transparency distributions, respectively, for DECaLS and MzLS.

2.6.4 Biases and Systematics

Fig. 2.6 shows that the zeropoint distribution for DECaLS and MzLS exhibit two surpris-
ing features: a 0.1 mag offset between the largest MzLS zeropoint and its fiducial value, and
a bimodal distribution for DECaLS. The relative atmospheric transparency (Fig. 2.7) inher-
its these bias and/or systematics due to its dependence on the zeropoint (Eqn. 2.4). The
0.1 mag offset is a systematic introduced by the CP pipeline because the raw image–derived
zeropoints do not have this offset. The larger DECaLS zeropoint mode is unphysical as it is
larger than the fiducial value, and Fig. 2.8 shows that it is purely made up of "CPDES82"
program images. The CP pipeline is handling these images differently from the other pro-
grams ("DECaLS", "NonDECaLS") and introducing a $0.1 - 0.2$ mag systematic. This explains
why the maximum MzLS transparency can be > 1. Those are "CPDES82" images.

While investigating the surprising features in Fig. 2.6, we found even more DECaLS and
MzLS zeropoint systematics with MJD. Fig. 2.9 shows that the night–averaged zeropoint for
DECaLS has steady decreased by about 0.4 mag over four years, which is about a 30% change
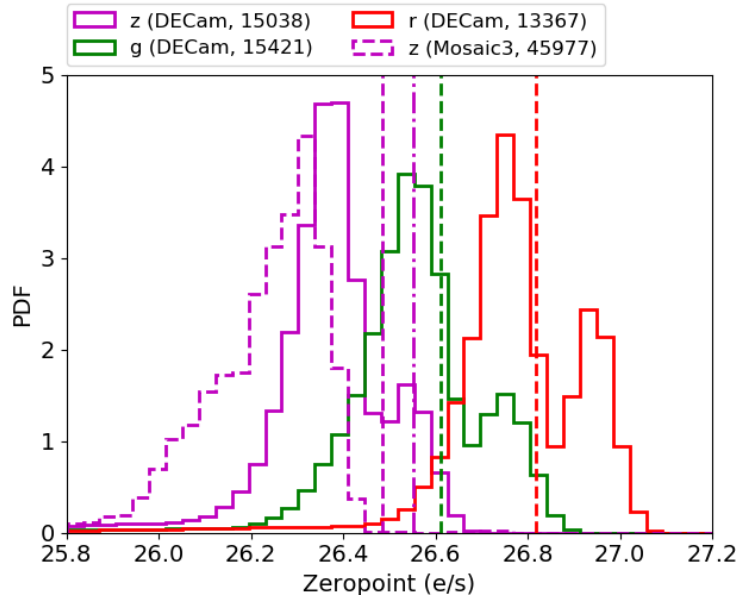
Figure 2.6: Zeropoint PDFs for DECaLS (solid) and MzLS (dashed), with fiducial values (Table 2.6) shown as vertical dashed (DECaLS) and dot–dashed (MzLS) lines. There are two surprising features: a 0.1 mag offset between the larger MzLS zeropoint and its fiducial value, and a bimodal distribution for DECaLS. The 0.1 mag offset is a systematic introduced by the CP pipeline because the raw image–derived zeropoints do not have this offset. The larger DECaLS zeropoint mode is unphysical as it is larger than the fiducial value, and is due to the CP pipeline handling "CPDES82" program images differently.

in flux. This is way too large to be due to accumulating dust on the mirror, degradation of the mirror coating, or some instrument specific effect, so we conclude that it is due to the CP pipeline. Fig. 2.9 shows the same night–averaged plot for MzLS, and the systematic is even larger. For the first half–year of data (MJD < 57600), the zeropoint decreased by at least 0.4 mag, then reset to its original value at MJD of about 57800 and decreased by about 0.3 mag over the next year.

    We now move onto astrometric offsets.

2.6.5   Astrometry

    We use the CP pipeline's WCS solution to compare the positions for stars we detect with their positions in the Gaia catalog. We refer to the median difference (our positions minus Gaia's) in RA and Dec as ΔRA and ΔDec, respectively. First, we plot the DECaLS night–averged ΔRA and ΔDec versus MJD in Fig. 2.10. ΔRA is well described by a least squares fit sinusoid with one–year period and 0.1″amplitude, at least until ΔRA goes to zero for MJD > 57750. The CP pipeline used the Two Micron All Sky Survey (2MASS)
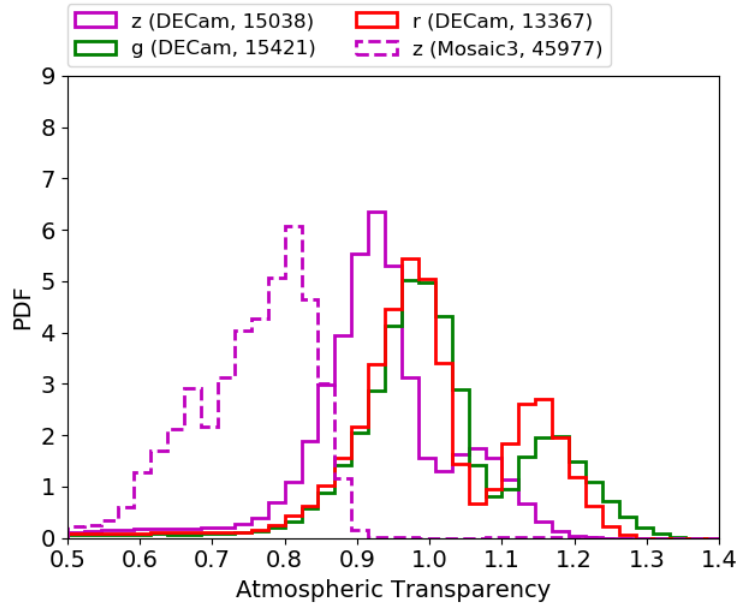
Figure 2.7: Atmospheric transparency, relative to a good night at the start of the survey, for DECaLS (solid) and MzLS (dashed). The bimodal distribution is inherited from the DECaLS zeropoints. The number of exposures are shown in the the legend.

(Skrutskie et al. 2006) for its WCS solution before MJD 57750, and Gaia afterwards, so the 0.1″amplitude is the average offset between 2MASS and Gaia. The year–period has to do with observing the NGC and SGC over the course of a year, and it means that the direction of the offset between 2MASS and Gaia is reversed for the NGC and SGC. ΔDec versus MJD is much easier to understand. It is the 0.1″offset between 2MASS and Gaia until it becomes zero after MJD 57750. Note, the CP pipeline for MzLS has only ever used Gaia for its WCS solution, so these ΔRA and ΔDec trends do not exist for MzLS.

Fig. 2.11 shows the 2–dimensional histograms for night–averaged ΔRA and ΔDec offsets for DECaLS and MzLS. In the DECaLS panels, there are three lobes. The lobe with zero–offset corresponds to MJD > 57750, while the other two lobes have the Dec and RA offsets seen in Fig. 2.10 for 2MASS relative to Gaia. For MzLS, the distribution of offsets agree with the zero–offset lobe in DECaLS, which is about ±0.05″.

2.6.6   5σ Depth

Based on the information provided thus far, we can compute the 5σ depth for each CCD. The 5σ AB magnitude depth, with Galactic extinction $AE(B-V)$ removed, is

$$m_{\text{depth}} = -2.5 \log_{10}\left(\frac{5\,\sigma_{\text{sky,eff}}}{t_{\text{exp}}}\right) + ZP - AE(B-V) \tag{2.5}$$
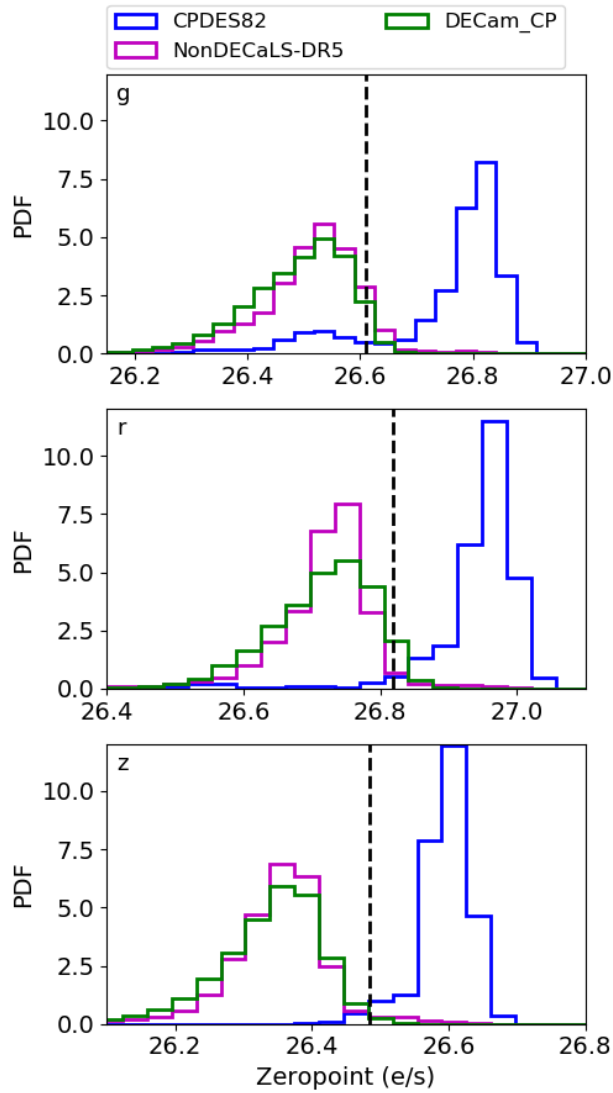
Figure 2.8: PDFs of DECaLS zeropoints for images coming from different observing programs (e.g., "DECaLS", "NonDECaLS–DR5", "CPDES82"), compared to the fiducial value (vertical dashed lines). The larger zeropoint mode is purely made up of "CPDES82" program images. The CP pipeline is handling these images differently from the other programs and introducing a $0.1 - 0.2$ mag systematic.

where $\sigma_{\mathrm{sky,eff}}$ is the square root of sky counts from a region having the size of the source,

$$\sigma_{\mathrm{sky,eff}} = \sqrt{\sigma_{\mathrm{sky}}^2 N_{\mathrm{eff}}}. \tag{2.6}$$
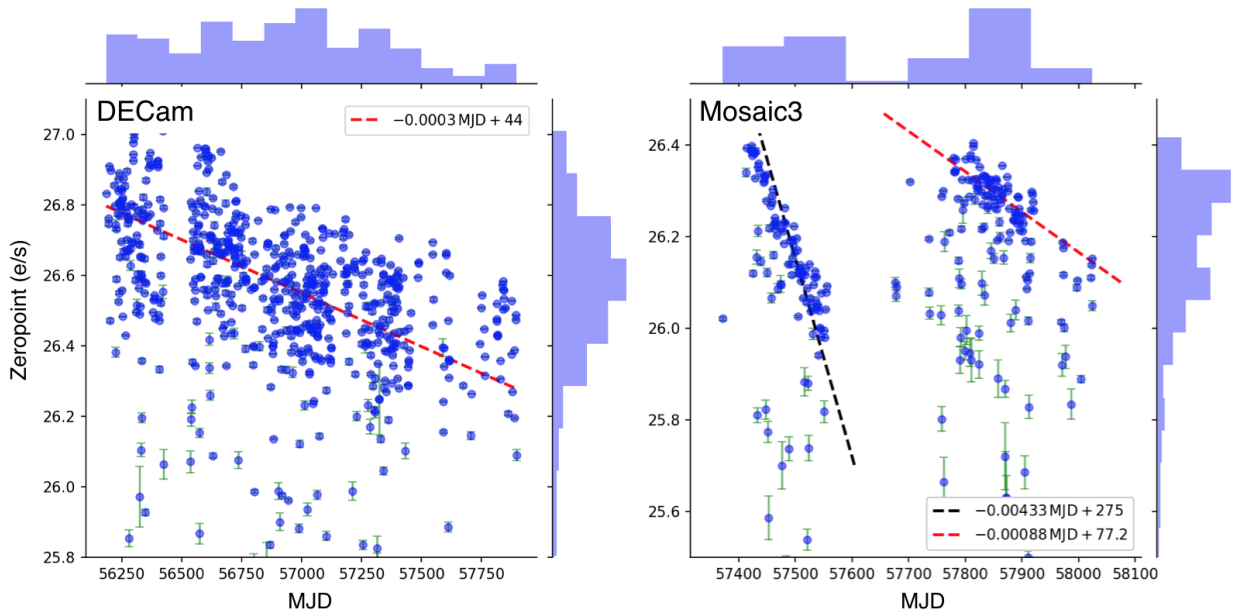
Figure 2.9: Average zeropoint per–night versus MJD. Error bars are the standard deviations for each night. The dashed lines are least squares fits to the data. (Left) DECam, the zeropoint decreased by about 0.4 mag over four years, which is about a 30% change in flux. This is too large to be due to an instrumental throughput so we conclude that it is due to the CP pipeline. (Right) Mosaic3, the black and red dashed lines, respectively, are least squares fits to the data before and after MJD 57600. In both cases, the zeropoint change is too large to be due to instrumental throughput.

N_{eff} is the noise equivalent area, i.e., the effective number of pixels of an astrophysical source on the CCD. It is

$$N_{\mathrm{eff}} = \left(\sum_i v_i\right)^2 \Big/ \sum_i v_i^2, \tag{2.7}$$

where v_i is the value of the PSF at each pixel. If the source is an extended object, then v_i is the value of the PSF convolved with the object's surface brightness profile. The Legacy Survey Data Releases use the quantities `psfnorm` and `galnorm`, instead of N_{eff}, but these are related to N_{eff} by

$$N_{\mathrm{eff}} = \frac{1}{[\mathrm{psf,gal}]\mathrm{norm}^2}. \tag{2.8}$$

`LegacyZpts` does not compute N_{eff} since `The Tractor` does not need it as input, so we use an estimator for N_{eff} instead. We use the same estimator as `Copilot` does (see Section 2.7.2),

$$\hat{N}_{\mathrm{eff}} \approx 4\pi\sigma_{\mathrm{see}}^2 + 8.91r_{\mathrm{half}}^2 + P_{\mathrm{sc}}^2/12, \tag{2.9}$$
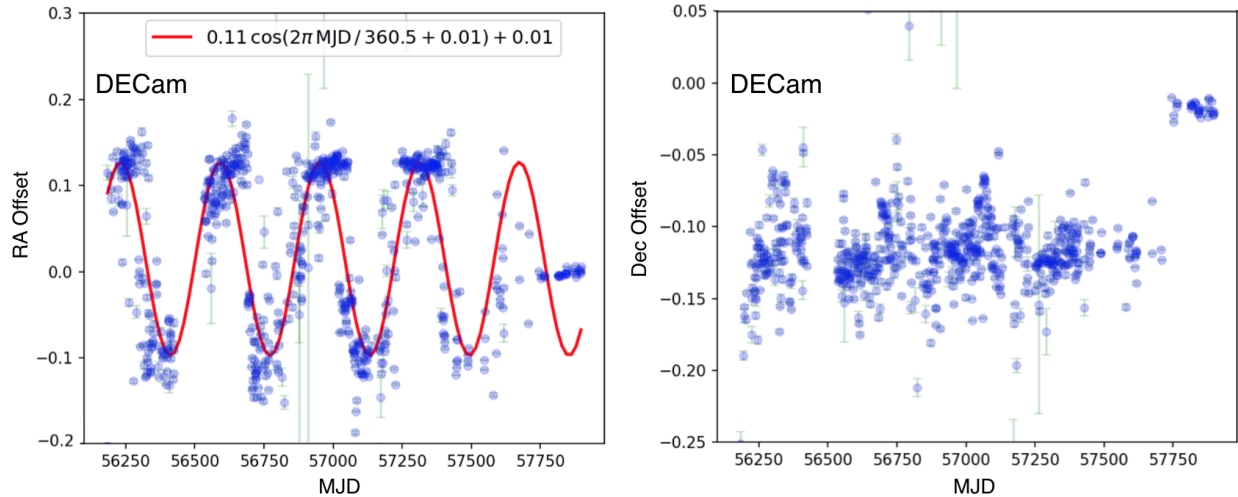
Figure 2.10: Nightly average of the median offsets in RA and Dec for DECam versus MJD. The offsets are relative to Gaia applying the CP pipeline's WCS solution to our measured positions. Red is the least square fit cosine. ΔRA is sinusoidal with one–year period and 0.1″amplitude. The CP pipeline used 2MASS for its WCS solution before MJD 57750, and Gaia afterwards, so the 0.1″amplitude is the average offset between 2MASS and Gaia. The year–period has to do with observing the NGC and SGC over the course of a year, and it means that the direction of the offset between 2MASS and Gaia is reversed for the NGC and SGC. ΔDec versus MJD is much easier to understand. It is the 0.1″ offset between 2MASS and Gaia until it becomes zero after MJD 57750.

where P_{sc} is the pixel scale, σ_{see} is the seeing and is related to the FWHM by $\sigma_{see} = $ FWHM/2.35 < 7, $r_{half} = 0.45$" for extended sources and $r_{half} = 0''$ for point sources. By comparing the $\hat{N}_{eff}$, using our `LegacyZpts` outputs, to N_{eff} using the values from DR3 and DR4, we find that a simple model $(A\hat{N}_{eff} + B)$ reproduces N_{eff} well. Fig. 2.12 shows a 2–dimensional histogram of the residual versus the N_{eff}. We fit a model for each camera and psfnorm/galnorm pair. Fig. 2.13 shows the residuals between the true galdepth and the value predicted using our model for N_{eff}. Our predictions have RMS of about 0.1 mag, which is roughly constant over both cameras, all bands, and galdepth. A slight majority of the predictions have positive residuals, so our model tends to underestimate the depth. We now determine whether the depths pass the DESI requirements.

Fig. 2.14 presents the PDFs for CCD depth (AB mag, extinction–corrected) for 5σ 0.45″exponential galaxies. These are all data for DECaLS and MzLS through May 22, 2017 and September 27, 2017, respectively. Vertical lines are the DESI requirements. For DESI, 90% of the footprint should reach or exceed the 0.45″exponential galaxy depth requirement. Fig. 2.14 considers the single pass case, so the 10th percentile depth (indicated by the filled regions) must be at or to the right of the DESI requirement. For example, the 10th percentile MzLS z depth is 0.35 mags deeper than required, while the 10th percentile DECaLS g, r, and
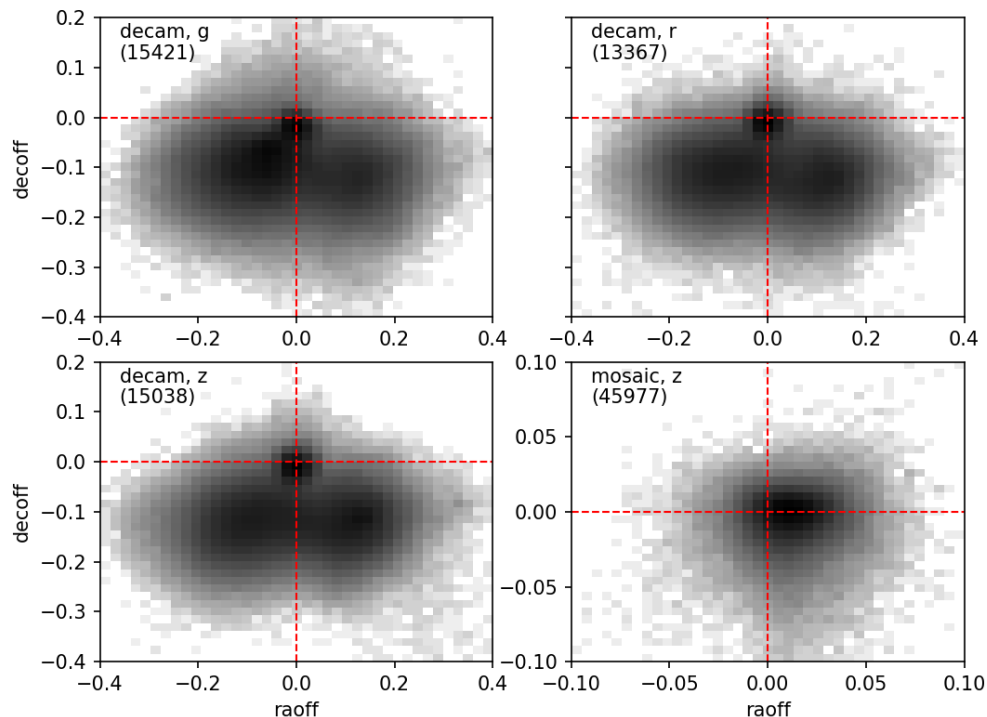
Figure 2.11: 2–dimensional histograms for the distributions of the average RA and Dec offsets, per night, for MzLS (bottom right) and DECaLS (otherwise). In the DECaLS panels, there are three lobes. The lobe with zero–offset corresponds to MJD > 57750, while the other two lobes have the Dec and RA offsets seen in Fig. 2.10 for 2MASS relative to Gaia. For MzLS, the distribution of offsets agree with the zero–offset lobe in DECaLS, which is about $\pm 0.05''$. This implies that all the MzLS CP images use Gaia for their WCS solution.

z depths are too shallow by 0.6, 0.4, and 0.3 mag, respectively. This reveals the importance of depth uniformity (i.e., a narrower depth distribution). The above is true despite DECaLS and MzLS having median depth $0.3-0.8$ mags deeper than the 10th percentile requirement. MzLS z passes the 10th percentile requirement because it is noticeably more uniform than DECaLS g, r, and z.

2.7   Dynamic Observing

2.7.1   General Concepts

Observing conditions at ground–based observatories change due to the temporal and spatial changes in the atmospheric transparency and stability, thermal imbalances between the telescope, dome and ambient environment, and the spatial location of celestial objects
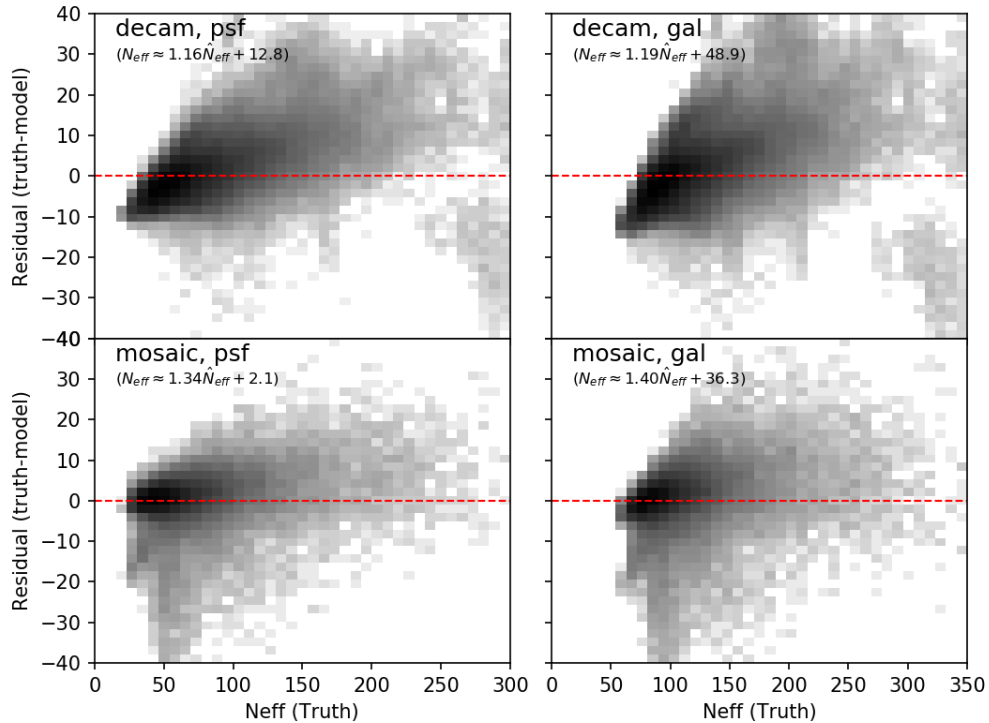
Figure 2.12: 2–dimensional histogram of the residuals between N_{eff} (Eqn. 2.7) and our model for $N_{\text{eff}} \approx A\hat{N}_{\text{eff}} + B$ (see Eqn. 2.9). We fit a model for each camera and psfnorm/galnorm pair.

at the time during which they are observed.

In an ideal world, observing conditions can be monitored during each on–sky integration while it is in progress, and the total duration of the ongoing exposure can be modified in real time to ensure that the image being taken reaches the appropriate depth. We will refer to this as a "perfect exposure time." This could be accomplished using, say, non–destructive reads to monitor the actual image data as it is being collected, or alternatively using some proxy to estimate the current conditions in the region (e.g., a guide or photometric camera co–located with the telescope and pointed at the same spot in the sky).

The hardware realities of the Mosaic3 and DECam instruments prevented us from implementing any real–time exposure control. However, we were able to implement the next best option: to analyze each image as soon as it was taken, estimate the image quality, transparency, resulting depth and telescope pointing offset, and then correct these as soon as possible, typically with a lag of 1 or 2 images or 2–3 minutes.
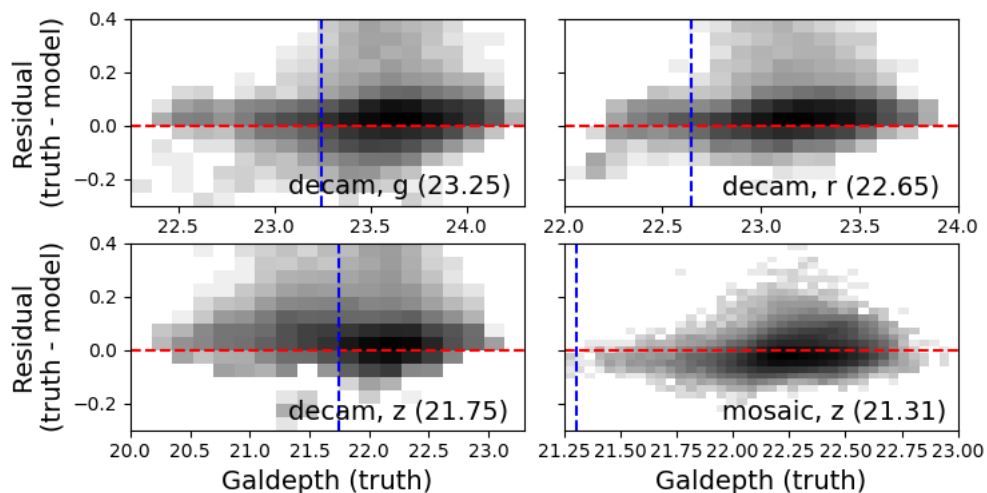
Figure 2.13: Residuals between the true galdepth and the value predicted using our model for N_{eff}. Our predictions have RMS of about 0.1 mag, which is roughly constant over both cameras, all bands, and galdepth. A slight majority of the predictions have positive residuals, so our model tends to underestimate the depth.

2.7.2 Implementation for DECaLS and MzLS

At both the Mayall and Blanco telescopes, we implement dynamic exposures using two (Python) software "bots":[7] both monitor the observing conditions and telescope pointing offsets, with one (`Copilot`) providing a graphical view of the derived estimates and the other (`decbot/mosbot` in the cases of DECam/Mosaic3, respectively) writing the required scripts and interfacing the instrument to modify the exposure time.

For each raw image, `Copilot` measures the seeing, sky brightness, atmospheric transparency, and photometric zeropoint. It computes CCD statistics following the same procedure as `LegacyZpts` (see Section 2.6) but with the following differences:

- The raw image, not CP processed image, is used

- Only the central 1000x1000 pixels of a single CCD or amplifier are analyzed for each exposure. This is CCD N4 for DECam and amplifier IM4 for MOSAIC3.

- The source detection threshold is S/N> 20 (whereas `LegacyZpts` uses S/N> 10)

- The WCS solution for raw images is not as well known so matching to the Gaia–PS1 catalog uses a $3''$ search radius (not $1''$)

For the observers, `Copilot` displays running plot of seeing, sky brightness, transparency, and RA and Dec offsets. Fig. 2.15 shows the plot from March 30, 2017.

---

[7]https://github.com/legacysurvey/obsbot
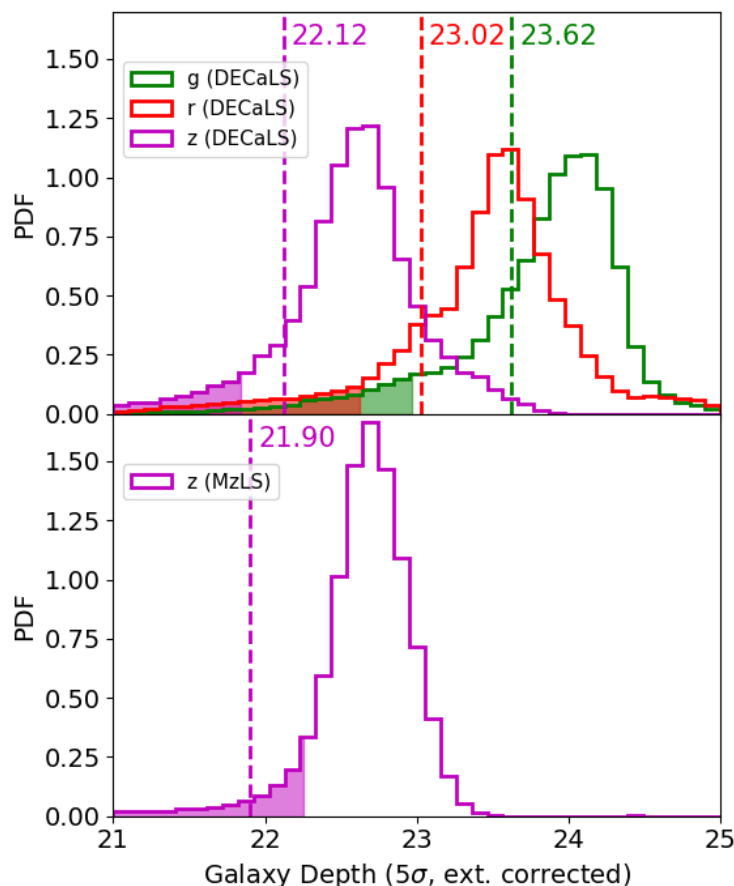
Figure 2.14: Per–CCD 5σ AB mag extinction–corrected galaxy depths for all DECaLS (top) and MzLS (bottom) exposures to date. Each band is a different color: g(green), r(red), and z(magenta). The colored numbers and dashed lines are the single pass DESI depth requirements (see Table 2.6.6), which depend on camera and filter. Transparent fill shows all CCDs with 10th percentile depth or less. DESI requires that 90% of the imaging reach galaxy depth, so the transparent fill needs to be at or to the right of the dashed line.

2.7.3 Perfect Exposure Times

This remainder of this Chapter determines the maximum possible impact that achieving perfect exposure times (exposing precisely long enough to reach depth) would have on DE-CaLS and MzLS. We asses the amount of telescope time that perfect exposures would save, relative to fixed exposure times, not the amount of telescope time we actually saved using our Python bots.

Given N_{eff} we estimate the exposure time needed to reach a desired point–source or galaxy depth (i.e., the perfect exposure time). The S/N is the variance of photo–electrons

Table 2.5: DESI Imaging Requirements

Camera	Filter	galdepth		
		q10	q50	pass 1
DECam	g	22.97	23.92	23.62
DECam	r	22.62	23.52	23.02
DECam	z	21.84	22.59	22.12
MOSAIC3	z	22.25	22.68	21.90

Note. — galdepth: galaxy extinction–corrected 5σ AB mag depth for a single pass. q10: 10th percentile for CCDs. q50: 50th percentile for CCDs. pass 1: DESI single pass requirement on galdepth DESI Collaboration (2016a).

from astrophysical sources divided by the standard deviation of photo–electrons from all sources (assuming an underlying Poisson distribution for the photo–electrons and negligible dark current),

$$S/N = \frac{N_{\text{src}}}{(N_{\text{src}} + N_{\text{sky}} + N_{\text{out}})^{1/2}}. \tag{2.10}$$

N_{src} is the number of photo–electrons from astrophysical sources, N_{sky} is number from the sky, and N_{out} is the number from reading out the CCD (i.e., the read noise squared). Rewriting this in terms of the flux from astrophysical sources F_{src} [e- sec^{-1} cm^{-2}], and from the sky F_{sky} [e- sec^{-1} cm^{-2} arcsec^{-2}], we have

$$S/N = \frac{F_{\text{src}}A_{\text{tele}}t_{\text{exp}}}{(F_{\text{src}}A_{\text{tele}}t_{\text{exp}} + F_{\text{sky}}A_{\text{tele}}N_{\text{eff}}t_{\text{exp}} + R_{\text{out}}N_{\text{eff}}N_{\text{exp}})^{1/2}}, \tag{2.11}$$

where A_{tele} [cm^2] is the effective area of the telescope's primary mirror, t_{exp} [sec] is the exposure time, R_{out} [e- pixel^{-1}] is the read noise (see Table A.2), and N_{exp} is the number of exposures.

We can now ask, what exposure time gives us S/N = 5 for our fiducial galaxy? Assuming the sky noise limit ($F_{\text{src}} \ll F_{\text{sky}}$) and solving for t_{exp}, we find

$$t_{\text{exp}} = \frac{S/N^2 N_{\text{eff}}(F_{\text{sky}}/F_{\text{src}}^2)}{A_{\text{tele}}} \left(\frac{1}{2} + \sqrt{\frac{1}{4} + \frac{N_{\text{exp}}(R_{\text{out}}/F_{\text{sky}})}{S/N^2 N_{\text{eff}}^2(F_{\text{sky}}/F_{\text{src}}^2)}} \right). \tag{2.12}$$

Eqn. 2.12 does not account for instrument throughput, such as filter transmission, light lost to corrector optics, and quantum efficiency, but it does show the scaling relationships we

need in order to implement automated dynamic exposure times. Readout noise is negligible relative to sky noise (see Table 2.6), so Eqn. 2.12 simplifies to,

$$\frac{t_{\text{exp}}}{t_{\text{exp},0}} = \frac{N_{\text{eff}}}{N_{\text{eff},0}} \frac{1}{\text{transp}^2} 10^{0.8[K(X-1)+AE(B-V)]-0.4\left[m_{\text{sky}}-m_{\text{sky},0}\right]}. \tag{2.13}$$

where K is the atmospheric extinction coefficient, X is airmass, $AE(B-V)$ is galactic extinction, and subscript "0" indicates our fiducial values (see Tables 2.6 and 2.7.4).

2.7.4   Survey Inefficiency

Now that we know our CCD depths, we can estimate how much telescope time we would save by using perfect exposure times. We are interested in the minimum observing time required to reach depth in every exposure. The minimum total telescope time needed, per night, to take N exposures (T_{need}) is

$$T_{\text{need}} = \sum_{i=1}^{N} t_{\text{need},i} + t_{\text{overhead}}, \tag{2.14}$$

where $t_{\text{need},i}$ is the perfect exposure time for each exposure and t_{overhead} is the time to readout the CCD (t_{read}), slew to the next tile (t_{slew}), and align the optical elements of the camera (t_{hexapod}). Read out and slew happen simultaneously. $t_{\text{slew}} < t_{\text{read}}$, so t_{overhead} is $t_{\text{overhead}} = t_{\text{read}} + t_{\text{hexapod}} \approx 21 + 11 = 32$ sec for DECam and $t_{\text{overhead}} \approx 30 + 0 = 30$ sec for MOSAIC3. Note, this is the expected overhead but controller timeouts, flushing the CCDs, and various hardware/software failures can make it significantly larger.

The time we actually spend observing per night (T_{obs}) is

$$T_{\text{obs}} = \sum_{i=1}^{N} t_{\text{exp},i} + t_{\text{overhead}}; \tag{2.15}$$

where $t_{\text{exp},i}$ is the exposure time we actually took. The time to re–observe K underexposures (T_{reobs}) should be added to Eqn. 2.15, which is at least

$$T_{\text{reobs}} = \sum_{i=1}^{K} (t_{\text{need},i} - t_{\text{exp},i}) + t_{\text{overhead}}. \tag{2.16}$$

We can now compute the survey inefficiency (S_{ineff}), the fraction of time we save by using perfect exposure times instead of t_{exp},

$$S_{\text{ineff}} \geq \frac{T_{\text{obs}} + T_{\text{reobs}}}{T_{\text{need}}} - 1 \geq 0 \tag{2.17}$$

In other words, S_{ineff} is the fraction of time that is "wasted" on over– and under–exposing.

We apply the following cuts motivated by how we carry out our survey. We enforce a minimum exposure time since CCDs with $t_{\text{need}} > t_{\text{max}}$ are probably not science quality (see Section 2.5.2).

Table 2.6: Fiducial Exposure Times

Band	Date	$t_{\mathrm{exp},0}$ (sec)	$t_{\mathrm{exp,min}}$ (sec)	$t_{\mathrm{exp,max}}$ (sec)	K	A
g	02/25/16	50	40	125	0.178	3.303
	04/07/16	50	40	250	0.178	3.303
	07/20/16	70	56	175	0.170	3.214
	02/02/17	70	56	175	0.170	3.214
r	02/25/16	50	40	125	0.094	2.285
	04/07/16	50	40	250	0.094	2.285
	07/20/16	50	40	125	0.10	2.165
	02/02/17	50	40	125	0.10	2.165
z	02/25/16	100	80	250	0.06	1.263
	04/07/16	100	80	250	0.06	1.263
	07/20/16	110	80	250	0.06	1.562
	02/02/17	100	80	250	0.06	1.562

Note. — K is the atmospheric extinction coefficient. The values for A are according to the Fitzpatrick (1999) extinction curve and the analysis of Schlafly & Finkbeiner (2011). The same z–band values are used for DECaLS and MzLS.

- $t_{\min} \le t_{\exp} \le t_{\max}$

- if $t_{\mathrm{need}} < t_{\min}$, then $t_{\mathrm{need}} = t_{\min}$

- drop $t_{\mathrm{need}} > t_{\max}$

and to remove outliers

- $20 < ZP < 30$

- transp < 2 (DECam), $0.4 <$ transp < 2 (Mosaic3)

Note that we occasionally changed the values for $t_{\min}$ and $t_{\max}$ as DECaLS and MzLS progressed, as shown in Table 2.7.4.

2.7.5 Implications

We plot the per–night S_{ineff} for DECaLS (green) and MzLS (magenta) in Fig. 2.16. MzLS is about 10% more efficient than DECaLS and has almost no high S_{ineff} ($> 50\%$) nights. The median S_{ineff} for DECaLS and MzLS is $23 \pm 1\%$ and $12 \pm 1\%$ (see Table 2.7.5). DECaLS has a S_{ineff} tail that extends beyond 100%, which means that the majority of exposures from

Table 2.7: Survey Inefficiency for DECaLS and MzLS, if we had used fixed exposures

	Camera	Filters	Median S_{ineff}	Nights
Per Night	DECam	g, r, z	23(1)	35(2)
	MOSAIC3	z	12(1)	29(2)

Note. — Uncertainties are the standard error on the median. The number of nights assumes 150 nine–hour nights for DECaLS and 240 for MzLS.

those nights were exposed at least twice as long as necessary. This is due to two effects. Until about a year ago, DECaLS was systematically overexposing in r–band by up to factors of 2, and the majority of $S_{\mathrm{ineff}} > 100\%$ nights are these. The other nights are highly variable, often not photometric and with few exposures taken, where `Copilot`'s predictions do more harm than good.

About 1/4 of both DECaLS and MzLS exposures are at least slightly underexposed. Assuming the awarded nights in Table 2.3, the median survey inefficiencies correspond to a potential savings of 35 nine–hour nights for DECaLS and 29 nine–hour nights for MzLS. Note, this is an underestimate because we assume that each underexposure is reobserved with t_{overhead} plus a perfect exposure time.

2.8 Conclusions

We presented the observing strategy for the DECaLS and MzLS surveys, our astrometric and photometric calibrations, and the implementation of dynamic exposure and the impact of perfect exposure times for DECaLS and MzLS. To our knowledge, DECaLS and MzLS are the first surveys to use automated dynamic exposure times. Dynamic exposure times are crucial to ground based surveys because they conserve telescope time and increase depth uniformity. We estimated that the median survey inefficiency of DECaLS and MzLS is at least 23% and 12%, respectively. The implications for future surveys like DESI is not clear. Naively extrapolating from the DECaLS/MzLS average savings in telescope time of 18% yields 0.9 years saved for DESI. However, DESI will take a small number of long (~ 20 min) exposures so the overhead from slew and readout is small, and other inefficiencies come from fiber positioning and effects unrelated to the observing conditions. If either survey decided to pursue perfect exposure times, DESI could do so with its Guide, Focus, and Alignment (GFA) sensors.
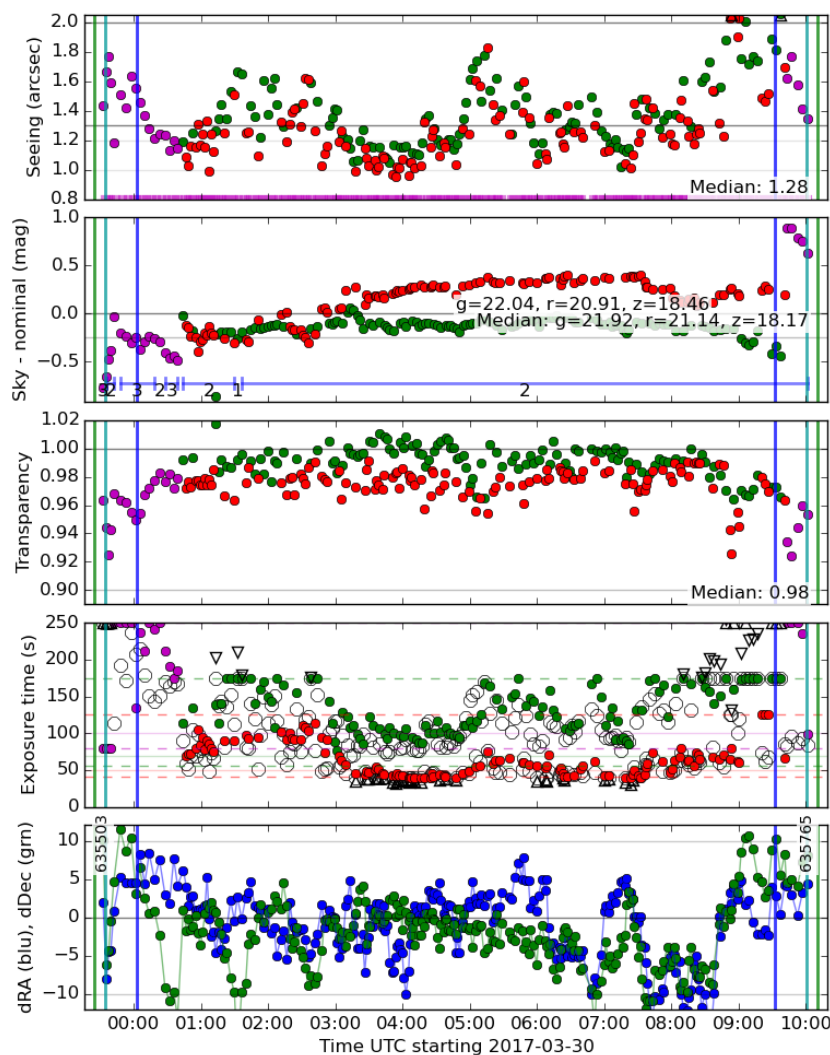
Figure 2.15: `Copilot` plot of the real time conditions for the night of March 30, 2017 for DECaLS. From top to bottom are the seeing, sky brightness (larger values are darker sky), transparency, and RA and Dec offsets between telescope and tile centers (in arcsec). Colors (green, red, magenta) represent the different filters (g, r, z), except in the bottom panel, where blue is RA offset and green is Dec offset. Vertical lines are 10, 12, and 18 degree twilight. In the seeing panel, the horizontal line at $1.3''$ is the decision boundary between pass 1 (below the line) and pass 2. In the sky brightness panel, the horizontal line at -0.25 is the decision boundary between pass 1 sky brightness (above the line) and pass 2. The numbers at the bottom with blue scale bars are the pass number we thought the image would be. In the exposure time panel, solid circles are the actual exposure times we performed while the open circles are the perfect exposure times for the images. The dashed horizontal lines are the maximum and minimum exposure times for each band. Triangles pointing up are images having the minimum exposure time that also exceeds the needed exposure time, while triangles pointing down are images having the maximum exposure time and are still too shallow. In the bottom plot, the horizontal lines at ± 10 arcsec indicate when observers pause observing to perform a pointing correction.
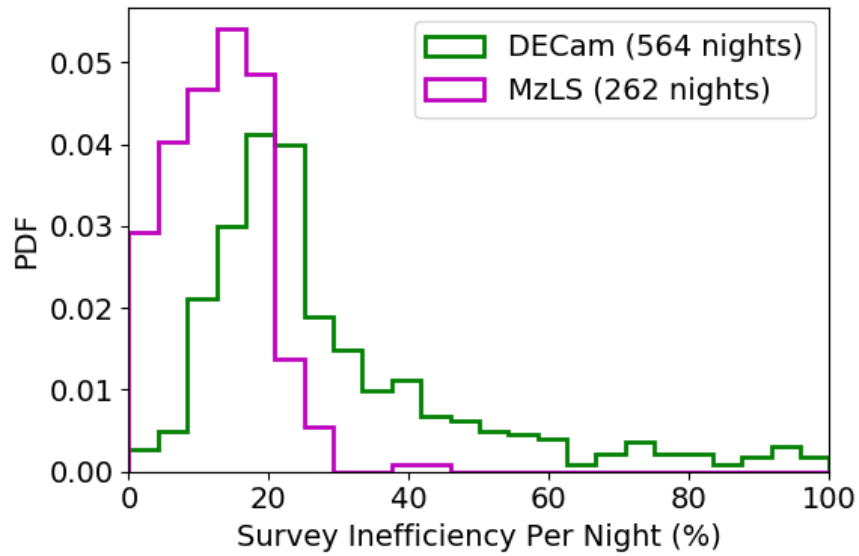
Figure 2.16: Per–night Survey Inefficiency (S_{ineff}) for DECaLS (green) and MzLS (magenta). MzLS is about 10% more efficient than DECaLS and has almost no high S_{ineff} ($> 50\%$) nights. DECaLS has a S_{ineff} tail that extends beyond 100%, which means that the majority of exposures from those nights were exposed at least twice as long as necessary.

Chapter 3

Implications of Dynamic Exposure Times for Large-Scale Surveys

The work in this Chapter is in preparation and will be published as Nugent & Burleigh (2018 in prep.).

3.1 Chapter Abstract

Here we explore the effect that dynamic exposure times can have on other wide-field surveys that have recently been conducted, or will be coming on-line soon, including PTF, iPTF, DES, ZTF and LSST. We summarize how DECaLS benefits from its use of dynamic exposure times, which we discussed in Chapter 2, and comment on how such an approach could be optimized for these future surveys. Given that most surveys begin with a nominal model of fixed exposure times, the benefits of such an approach are quite impressive.

3.2 Introduction

Astronomers have been optimizing telescope schedules for decades, though typically this has been at a very coarse level: IR observations and high-resolution spectroscopy are carried out during bright while optical imaging and low-resolution spectroscopy occur during dark or grey time. During a night with variable seeing a spectroscopist may switch from a wide slit to a narrower one to maximize signal-to-noise and/or add additional exposures to achieve a given signal-to-noise ratio. In addition, potential target lists may include a wide range of object brightnesses to handle poor transparency and/or seeing conditions. The latter has been used to great effect on those telescopes with queue observing modes.

However, as far as we know, DECaLS is the first survey to implement dynamic exposure times on an image-by-image basis (though usually the updates to the exposure time lag 4-5 images behind). In Figure 3.1 we see how this approach, not used in the first year of the survey, impacted subsequent observational efficiency. Here the we can see that the

introduction of `Copilot` was able to decrease the effect of the sky conditions by over 50% on the dispersion in the achieved limiting magnitude. As stated in the previous Chapter, given the actual data and the limitations of `Copilot`, the survey efficiency was improved by 20%. For a 100-night survey this is an impressive improvement.
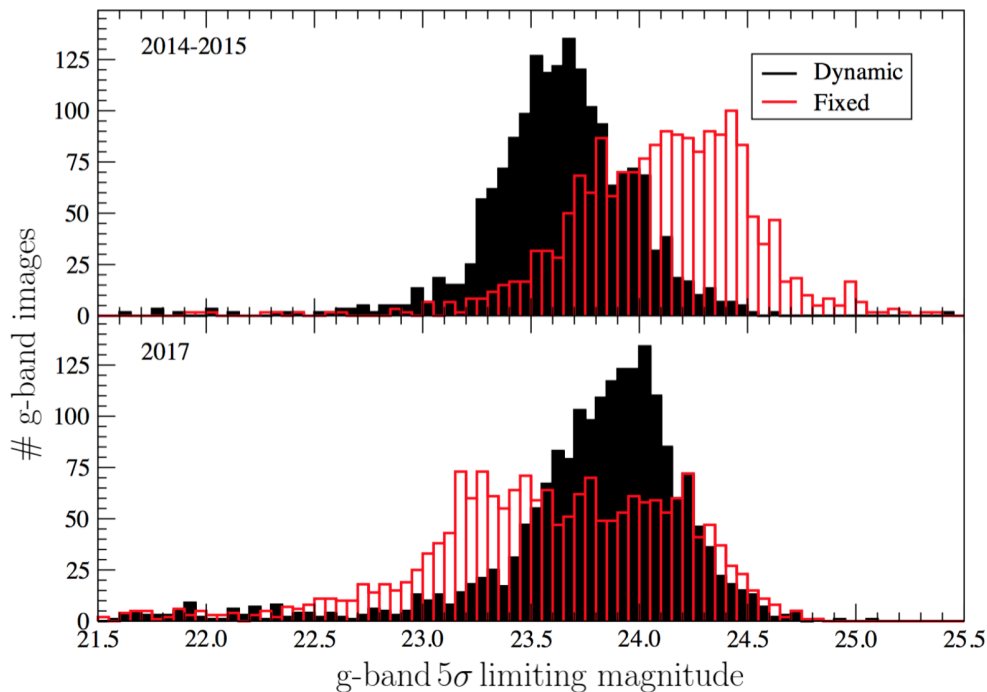
Figure 3.1: 5σ *g*-band limiting magnitudes where the exposure times are, as observed, adjusted dynamically by the observer (black) or fixed at nominal 130 seconds (red). DECaLS looks to achieve a 3σ limiting magnitude of 24.0 with 3 exposures (or ~ 23.5 in any individual exposure). *Top:* From 2014–2015 the exposures were adjusted by the observer periodically due to an eye-ball estimate of the current conditions. Note that while the desired shift to a median slightly below 24th magnitude was achieved, the FWHM is only reduced by 25% (from 1.0 mag to 0.75 mag). *Bottom:* By 2017 `Copilot` was well established and dynamically adjusting the exposure times based on seeing, sky brightness, and MW extinction. Here the reduction in the FWHM goes from 1.3 mag to 0.6 mag, an improvement > 50%.

Co-Pilot is limited by the fact that the prediction for the current exposure time is based on analysis of images that were taken several minutes earlier. Therefore it doesn't account for more rapid changes in sky conditions nor in even simpler shifts such as when one moves from lower to higher airmass under excellent conditions. In the following sections we will explore the effect such an approach would have on upcoming surveys such as ZTF and LSST, making just nominal changes based simply on MW extinction and airmass, to an idealized one where it would be possible to use the guide cameras to exactly determine the

sky conditions "on–the–fly" and adjust accordingly in real-time.

3.3   Optimization

In any survey, what one is trying to optimize on is the number of objects found. Thus, in reality, it comes down to a question of how much volume one can survey efficiently. Since the volume is simply:

$$V = \frac{4}{3}\pi d^3, \tag{3.1}$$

then converting to magnitudes through:

$$m - M = 5\log_{10}(d) + 25 \tag{3.2}$$

the volume is:

$$V \propto 10^{0.6m}. \tag{3.3}$$

In general, observers are not trying to maximize the total number of objects they find. If this was the case then, assuming a Gaussian dispersion in limiting magnitude for a fixed exposure time, the number of objects lost due to images with limiting magnitudes brighter than the median would be compensated for by objects found in those images which go fainter than the median limiting magnitude. Rather, astronomers like to optimize the total number of objects to a given magnitude, typically based upon limitations of their follow-up resources.

An example of this can be found in the DECaLS imaging survey where the focus is on delivering targets for the DESI spectroscopic survey. Here the limitations on the instrument are on achieving a $S/N > 5$ in the O II lines. Since O II is at a restframe wavelength of 3727 Å and the red cutoff in the instrument is at 1 μm, this translates to having a cut in both redshift ($z \leq 1.7$) and brightness due to the fact that the Mayall is only a 4-m telescope. This is achieved through a color cut and a limiting r-band magnitude of < 23.4 (see Fig 3.2).

In the Palomar Transient Factory (PTF) and the subsequent Zwicky Transient Facility (ZTF) there are several optimizations one needs to consider given the wide variety of science goals. They include seeing mmag variations in M-stars to search for planets via occultation, maximizing the number of supernovae found several magnitudes before peak brightness, or maximizing the total number of superluminous supernova found in the survey (see Law et al. 2009). Not only is such a survey impacted by the limiting magnitude of an individual image but, given the requirement that several images spanning weeks to months, go into characterizing a transient, the survey cadence and the ensemble of limiting magnitudes for a given object have a direct impact on the science.
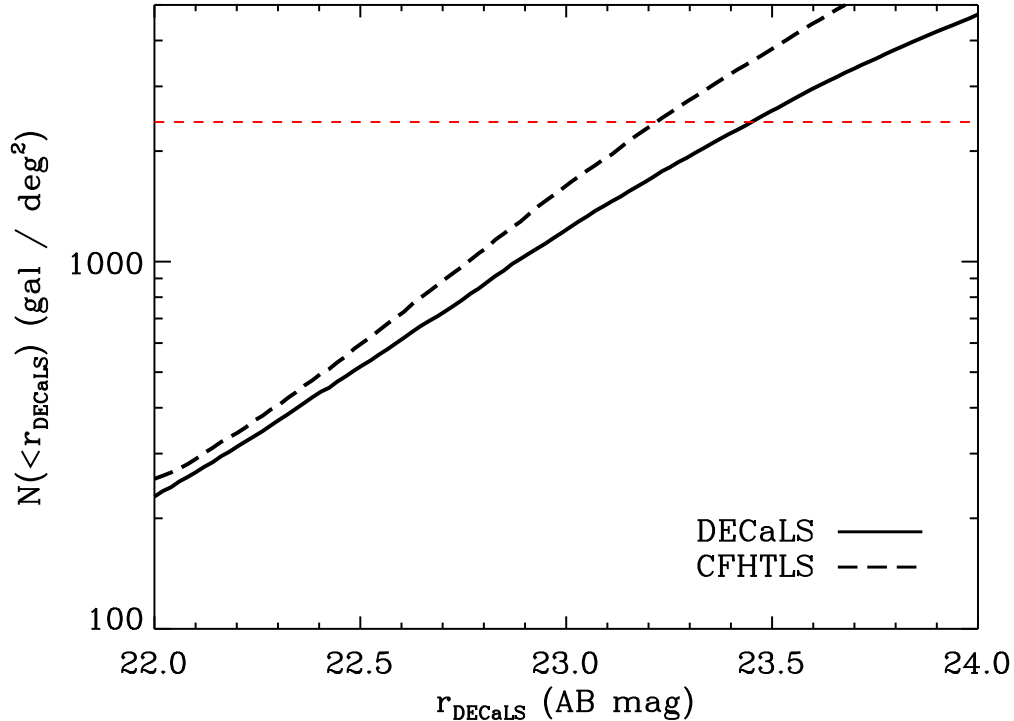
Figure 3.2: Surface density of ELGs as a function of limiting *r*-band magnitude. The solid black line shows the surface density of objects which lie within the DESI color cuts as a function of r_{AB} magnitude based on a 35 deg^2 region of DECaLS observed to the final survey depth. For comparison, the dashed line is the set of objects selected from CFHTLS-Deep photometry which has been transformed and degraded to the anticipated depth of DECaLS (difference between the two are due to photometric calibration). The horizontal dashed red line shows the DESI ELG target density goal of 2400 targets/deg^2 achieved at $r_{AB} = 23.4$. Adopted from DESI Collaboration (2016a).

In Fig. 3.3 we can see the potential for optimizing such surveys. For the idealized case where there is no loss in time due to readout, slew or filter exchanges, by cutting down on both the dispersion and the depth of the limiting magnitude one can simultaneously increase the completeness factor while decreasing the total time spent on the survey. In the more complicated case of some fraction of the time lost due to the instrument, t_{inst}, for any exposure with an exposure time t_{exp} we have the following with a survey with N_{tot} images:

$$Total\ Time = \sum_{i=1}^{N_{tot}} t_{exp_i} + t_{inst} \qquad (3.4)$$

Given the nominal survey for PTF with its 60 sec exposures and ∼30 sec spent on readout and slew, a survey of 300 images would require 7.5 hours. This was a typical night during the
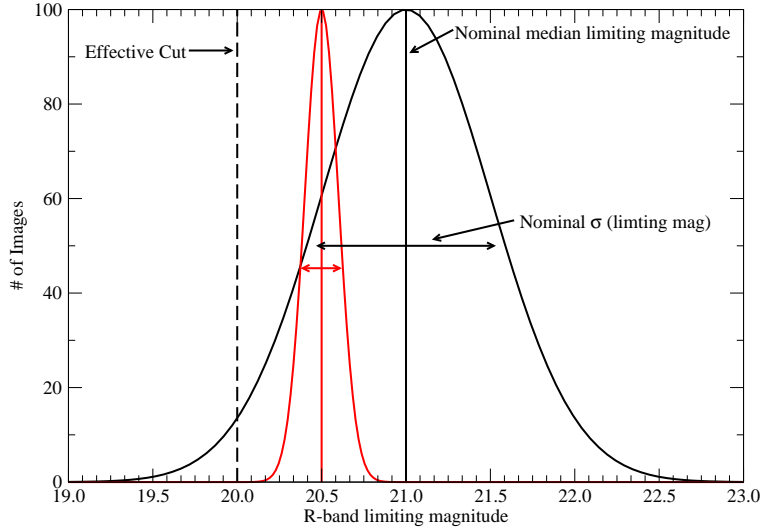
Figure 3.3: A toy plot of the typical dispersion in the limiting magnitude for an imaging survey (in black) with a nominal effective cut in brightness for objects to be 90% complete. Such cuts are important for optimized follow-up and/or limiting the systematics in the rates of discovered objects. A more ideal survey is shown (in red) for comparison with a brighter limiting magnitude and a tighter dispersion about it. Such a survey, assuming that there is no loss in time for readout, slew, etc.) and drawn from the nominal survey depths, would take only 33% of the time spent on the original survey being 0.5 mag shallower. Additionally, it would be nearly 100% complete given the effective cut in brightness compared to the 90% completeness achieved in the nominal survey.

survey and provided a median 5σ limiting magnitude depth of $g = 21.08$ and $R = 20.80$ (see Fig. 3.4). Note the very broad range in limiting magnitudes as well as the 90% completeness achieved at $R = 19.8$ and $g = 20.2$ magnitudes. This was, however, not an ideal use of resources. If it was possible for the survey to "on-the-fly" adjust exposure times to achieve a nominal depth of 20th mag. in R-band with a $\sigma = 0.05$ mag., then given that for sky-limited observations a constant SNR is achieved when:

$$t \propto 10^{0.8m}, \tag{3.5}$$

we get, based on Eq. 3.4 and using the observed distribution of limiting magnitudes, that the total time for the same survey would be 4.0 hours. This is a savings of 45%. Since one could then use the remaining 3.5 hours to survey additional fields (coupled with the fact that the average exposure time in the revised survey is 16 sec), another 273 images could be

taken to the same depth. This increases the volumetric rate by almost a factor of 2.
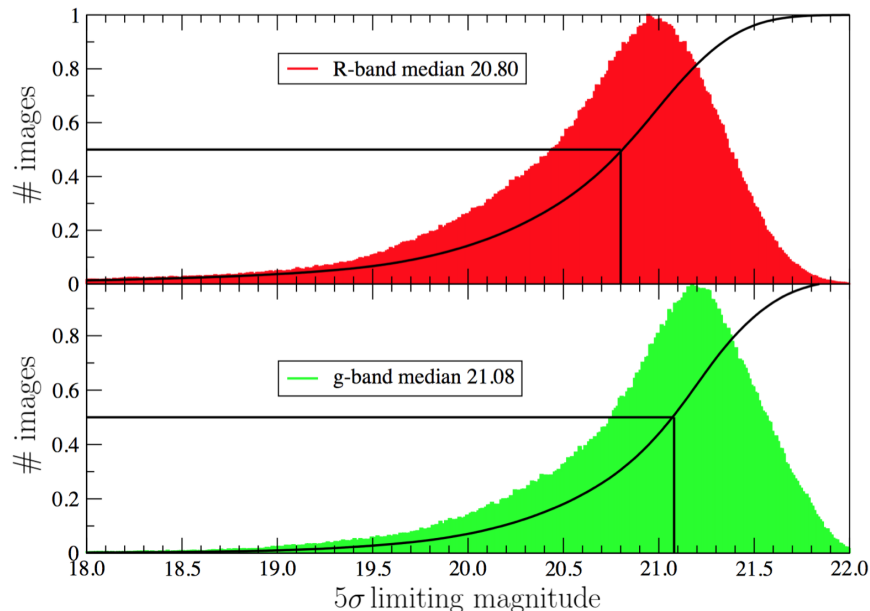
Figure 3.4: A plot of the *R*-band (top) and *g*-band 5σ limiting magnitudes for PTF. The distributions show a FWHM dispersion about the median in excess of 1.0 mag with a long tail towards shallower depths due to clouds, proximity to the moon and poor sky conditions.

3.4 Future Possibilities

So, is such an "on-the-fly" survey even possible? The designs of ZTF and LSST should be able to achieve something akin to these savings. Given that each instrument has guide camera which can read out at sub-second rates it should be relatively simple to design software to measure the seeing, sky brightness and even the transparency for each pointing and adjust the final exposure time accordingly. Coupled with the location on the sky to correct for MW extinction for extra-galactic objects, the revised surveys would be dramatically more efficient. However, there are some limitations to such a survey which are not explicitly acknowledged in this analysis.

First, there are limits for how short an exposure we should take due to factors like read noise and the ability to transmit large images to their respective data processing centers.

Second, a cap on the exposure time would have to be placed as extremely poor sky conditions lead to other issues which can not be corrected for by increasing the exposure time alone (such as variable transparency across the focal plane). Thus the real benefits, while still large, would be slightly diminished.

Some might argue that such a software system would, in itself, be too expensive to create and that resources would be better spent elsewhere. Even here, savings can be had without *real-time* intervention. Consider just the effect of airmass on the observations as shown in Ivezić et al. (2008) one can look at the change in magnitude as a function of airmass (X) as:

$$\Delta m = -0.1(X - 1) - 1.5 log(X) - S(X - 1), \tag{3.6}$$

where the first term is the loss due to atmospheric extinction and the second term is due to the increase in seeing with airmass, assuming seeing $\propto X^{0.6}$. The final term is due to the increase in sky brightness. In Fig 3.5 we plot the PTF limiting magnitudes as a function of airmass over the entire survey. We can see that it is well fit by the above equation with $S = 0.22$.
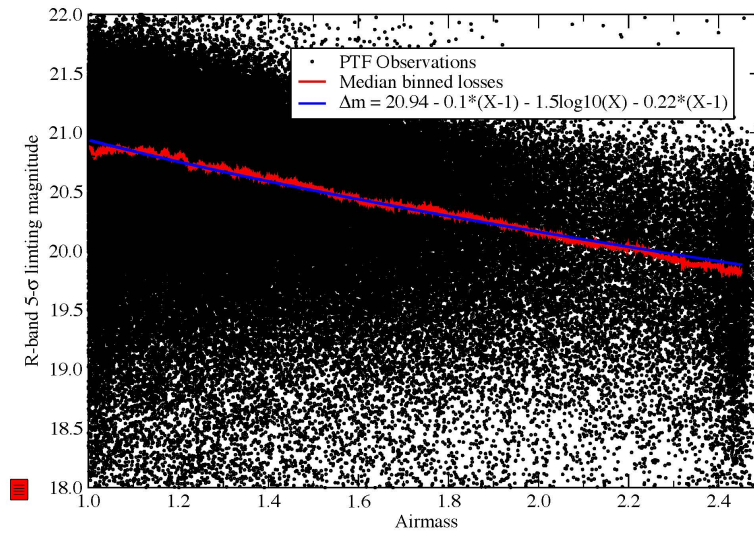
Figure 3.5: A plot of the R-band 5σ limiting magnitudes as a function of airmass for PTF. A boxcar median over 3000 points is well fit by Eq. 3.6. The 1σ dispersion about the median is ~0.6 mag.

Correcting for this term alone decreases the overall dispersion by 0.22 mag given the observing conditions seen in PTF, a net increase of 30% in volume assuming that one targets hitting the same depth achieved for the median airmass ($X = 1.29$).

Similarly, one can adjust the exposure times for MW extinction. In Fig. 3.6 we plot a histogram of the observed galactic extinction in R-band as seen by PTF. With no change in total exposure time, >80% of the extragalactic fields can be corrected to the same limiting

magnitude as achieved for the median pointing in PTF ($A_R = 0.12$). This results in a net increase of 23% in survey volume.
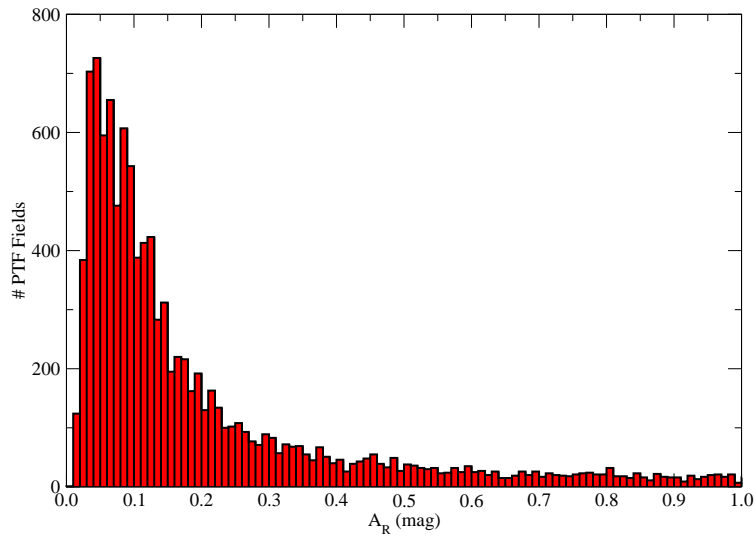
Figure 3.6: A histogram of the MW extinction in R-band for the PTF fields visible from Palomar with < 1 mag of extinction. The median extinction is $A_R = 0.12$

While it is certainly true that larger gains could be had by adjusting for sky brightness, seeing, and transparency, even these nominal adjustments for airmass and galactic extinction can pay substantial dividends.

Chapter 4

`Obiwan`, A New Hope: Characterizing Astronomical Imaging Systematics with Forward Modeling and Monte Carlo Simulations of Galaxies

The work in this Chapter is in preparation and will be published as Burleigh et al. (2018b in prep.).

4.1 Chapter Abstract

We present a new method for characterizing imaging systematics in a joint analysis of astronomical images from multiple telescopes. A major challenge for future and ongoing galaxy surveys will be to understand the inevitable biases and systematics in their galaxy sample(s). For example, the Legacy Surveys will combine g, r, and z imaging from three telescopes to provide 30M galaxy targets for the Dark Energy Spectroscopic Instrument (DESI). Our Monte Carlo method adds simulated sources to random locations in astronomical images and then performs source detection and measurement, characterizing the complex selection inherent in large–scale–structure catalogs. The process is repeated until the injected source density is high enough to satisfy one's science objectives. For instance, the DESI target density for emission line galaxies (ELGs) is 2400 deg^2, so simulated ELGs should be injected at more than 10 times this density. We developed the code `Obiwan` to implement this for the Legacy Surveys pipeline, `Legacypipe`. This Chapter showcases `Obiwan`'s ability to identify biases and systematics by injecting 130k simulated galaxies into 1 deg^2 of repeat imaging of the COSMOS field.

4.2   Introduction

Astronomers perform galaxy surveys to measure how galaxies cluster at different times in the past. Clustering statistics, such as the 3–dimensional correlation function projected onto a sphere (the angular correlation function), provide a measure of the expansion rate of the universe and can answer many other fundamental questions about the universe (Peebles 1980). Some of the most widely known galaxy surveys include the APM (Maddox et al. 1996), Center for Astrophysics redshift survey (CfA, Huchra et al. 1999; Falco et al. 1999), SDSS (York et al. 2000), 2dF Galaxy Redshift Survey (2dFGRS, Colless et al. 2001b), WiggleZ (Drinkwater et al. 2010), BOSS (Dawson et al. 2013), and eBOSS (Dawson et al. 2016). Images of the night sky are transformed into a 3–dimensional large–scale–structure catalog by passing them through a pipeline that automatically detects and models galaxies, extracting a sample of galaxies that satisfy particular selection criteria, and obtaining spectra and measuring redshifts for them. Clustering statistics are then computed from the positions of the galaxies on the sky and their redshifts.

A major challenge for future and ongoing galaxy surveys will be to understand the inevitable biases and systematics in their galaxy sample(s). To make cosmological measurements, the clustering statistics of the observed distribution of galaxies must be compared to a random distribution of galaxies that incorporates all the signatures of systematic effects that impact real data. This would be easy if every galaxy could be detected, but a large number of instrumental effects can make the observed and actual distributions of galaxies very different. For example, two galaxies that appear near each other on the sky will often be detected as a single galaxy; the fainter galaxy often being lost. Similarly, bright stars make the detection of nearby faint galaxies challenging. Variations in observing conditions, especially for a multi–year survey, create unobserved or poorly sampled regions of the sky and consequently fewer galaxy detections. These biases and systematics, which come in at the few percent–level, must be accurately characterized in order for the next generation of galaxy surveys to measure cosmological parameters to sub–percent accuracy. However, describing which galaxies are and are not detected in the vicinity of a bright star requires knowing how source detection and measurement proceed, which is encoded in a piece of software with more than ten thousand lines of code.

This Chapter presents a new method capable of characterizing the above process. We add simulated sources, with properties closely matched to the galaxies of interest, to random locations in the images and then run the source detection and measurement software. By measuring how the simulated sources are lost and recovered we can estimate how a galaxy survey generates large–scale–structure catalogs. This enables us to create a random distribution of galaxies that incorporates all the signatures of systematic effects that impact real data, which we can compare to the observed galaxy distribution. We call our method `Obiwan`, since it may be *the only hope*[1] of accounting for the aforementioned biases and systematics.

We specifically built `Obiwan` for the Legacy Surveys (Dey et al. 2018) because its imaging

---

[1]In Star Wars: Episode IV, A New Hope (Lucas 1977), Princess Leia says, "help me Obi-Wan Kenobi you're my only hope"

data provided 255k emission line galaxy (ELG) targets for eBOSS (Raichoor et al. 2017) and will provide 30M galaxy targets for the Dark Energy Spectroscopic Instrument (DESI) (DESI Collaboration 2016a,b). The Legacy Surveys require a joint analysis of images from three telescopes. Each telescope obtains multi– and same–band imaging of the same part of the sky with month to year intervals between exposures. The g, r, and z filters for the three cameras are similar DESI Collaboration (2016a), but the electronics, local mountain top conditions, and survey strategies are very different (see Zou et al. 2017 and Chapter 2).

The remainder of this Chapter presents `Obiwan` and a small proof of concept simulation using DECaLS data. All data products are available at NERSC (see Section B.2). See Chapter 5 for a much larger simulation to characterize biases and systematics in eBOSS ELGs with `Obiwan`. This Chapter is structured as follows. In §4.3, we summarize how `Obiwan`, `Legacypipe`, and `Tractor` work and their most important algorithms. In § 4.4, we describe the DECaLS imaging data we use for our `Obiwan` runs. In §4.5, we present our results from running `Obiwan`and discuss the biases and systematics in `Legacypipe` and `Tractor` that we find. We conclude in §4.6. The Appendix presents documentation and performance details for `Obiwan`.

4.3   Methods

4.3.1   `Obiwan`

Fig. 4.1 schematically shows how `Obiwan` works. Every time `Legacypipe` reads an image, `Obiwan` modifies it and its associated inverse variance map by adding simulated sources with appropriate noise. `Legacypipe` does not know about the simulated sources and source detection and measurement continue as usual. We also add Galactic extinction to each source based on its RA and Dec, using the SFD98 E(B−V) maps of Schlegel et al. (1998). Blending between simulated sources is prevented by temporarily setting aside all simulated sources that would be within 5″ of another simulated source, and injected those set–aside sources during the next Monte Carlo iteration. Blending between real and simulated sources is allowed (and needed to fully simulate the angular selection function). This 5″ criterion only applies to pairs of simulated sources. `Obiwan` is unique because it adds sources to individual exposures and model parameters are determined maximum likelihood estimation (MLE). Although the likelihood of the data is only approximate, MLE is better than heuristic algorithms.

`Obiwan` models stars in exactly the same way as `Tractor` by using the same pixelized PSF model files; however, it models galaxies in a slightly different way. `Tractor` approximates Sérsic profiles with mixtures of Gaussians, but `Obiwan` uses actual Sérsic profiles for galaxies (i.e., Sérsic profiles convolved with the pixelized PSF). We chose to avoid more complicated (and probably more realistic) galaxy profiles so that we could test how well `Tractor` performs in the best case scenario (e.g., sources with profiles nearly identical to the models it is fitting). Relatively simple galaxy profiles may also be sufficient for DESI, as its primary galaxy

Figure 4.1: Example of `Obiwan` adding 4 simulated galaxies to three 200x200 pixel DECam images, one image per *g*, *r*, and *z*-band, respectively. The original image (top left) is modified by adding 4 simulated galaxies (top middle) to create the new image (top right), on which `Tractor` operates. The model and residual images are the bottom panels. The top and bottom galaxies are de Vaucouleurs and the left and right are exponential.

target (emission line galaxies) are faint and not resolved. All convolutions and rendering is performed with the Python package GalSim.[2]

The simulated sources should inherit the Galactic extinction of the region we add them to, so we make each source fainter by the amount appropriate for its RA and Dec. Chapter 5 shows examples of relatively bright real and simulated exponential galaxies with similar *g*–band magnitudes (see Fig. 5.2). Based on inspection of the full sample, the simulated galaxies are visually indistinguishable from their real counterparts.

4.3.2 `Legacypipe`

The Legacy Surveys use the `Legacypipe` pipeline[3] to detect and model stars and galaxies in the imaging data. `Legacypipe` has six stages: read the images (`tims`), apply bright star and bad pixel masks (`mask junk`), co–register the images and perform source detection (`srcs`), run `Tractor` (Lang et al. in prep) to maximize the likelihood of the data

---

[2]https://github.com/GalSim-developers/GalSim
[3]https://github.com/legacysurvey/legacypipe

(`fitblobs`), write out coadded images for the images, models, and residuals, and write out the measurement catalog (`writecat`). Profiling `Legacypipe` shows that `fitblobs` is the most time consuming step by about a factor of ten (see Fig. B.1). We now discuss the critical algorithms in `Legacypipe`.

Calibrating the Raw Images

`Legacypipe` uses the calibrated images provided by the NOAO Community Pipeline (CP, Valdes et al. 2014), not the raw images from the telescope. The CP performs the usual calibration steps: bias subtraction, flat fielding, sky subtraction, flagging of pixels containing artifacts or transient sources (e.g., bleed trails, saturated pixels, cosmic rays), creation of a weight map for the uncertainty in counts for each pixel, and astrometry (mapping between pixel position and location on the sky).

Source Detection

`Legacypipe` uses a matched filter to detect sources having signal–to–noise (S/N) > 6. A matched filter cross correlates the data with the expected signal (the Point Spread Function or PSF for astronomical images), which means that a matched filter is a S/N image. Each part of the sky can have multiple observations at multiple band passes. All images are co–registered and images with the same band pass are combined as a weighted average, where the weights are the per–pixel inverse variances. The underlying assumptions are that the images are sky dominated (i.e., the sky–noise limit), pixels are independent, the counts in each pixel (i.e., number of photo–electrons) are Poisson distributed, and that there are always sufficiently many counts that we can approximate the distribution as Gaussian with equal variance to the Poisson variance. There is a matched filter for each each band pass, and these are combined as a weighted sum, with weights equal to the Spectral Energy Distribution (the relative flux of a source in each band pass, SED) for the sources of interest. A flat SED, $(g, r, z) = (1, 1, 1)$, is equally bright in g, r, and z, so the final matched filter is the sum of the g, r, and z matched filters. `Legacypipe` uses 5 SEDs to create 5 matched filters. Any pixel value > 6 in any of the matched filters is flagged as a real source. There is one SED per band g (1, 0, 0), r (0, 1, 0), and z (0, 0, 1), a red SED (2.5, 1, 0.4) for detecting red elliptical galaxies, and a flat SED (1, 1, 1) for star–forming spiral galaxies.

A S/N of 6 and the 5 SEDs are the hyper–parameters chosen based on what worked well in the past for most sources. `Obiwan` could inject a specific source of interest, such as emission line galaxies for DESI, and grid–search for the optimal S/N and SEDs combination for that source.

"Blobs"

Blobs are contiguous regions of S/N > 6 pixels and each blob can contain multiple sources. `Legacypipe` is parallelized over blobs, so that the maximum number of embarrassingly parallel tasks is equal to the number of blobs. This scales poorly when there are only a

few blobs, which happens for large objects (bright stars, galaxies close to our Milky Way) and very deep imaging (the DES supernovae fields, COSMOS, etc.). Fitting models to each source (`Tractor`) is the most time–consuming stage in `Legacypipe`, so full–depth processing of deep fields is computationally challenging.

Tractor

`Tractor` models stars (i.e., point sources) with a pixelized PSF, created by the code `PSFex` (Bertin 2011), normalized to a $7''$ aperture. Galaxies are modeled as a Sérsic profile convolved with the pixelized PSF model. `Tractor` saves time by approximating Sérsic profiles as Gaussian mixtures (Lang et al. in prep). Astronomers have characterized the surface brightness of a galaxy by Sérsic profiles for some time (Sersic 1968; Rowe et al. 2015),

$$I(r) = \frac{F}{2\pi n \Gamma(2n) r_0^2} e^{-(r/r_0)^{1/n}}, \tag{4.1}$$

where Γ is the Gamma function, r_0 is the scale radius, and n is called the Sérsic index. The most commonly used types are exponential ($n = 1$),

$$I(r) = \frac{F}{2\pi r_0^2} e^{-r/r_0} \approx \frac{F}{2.231 r_{\text{half}}^2} e^{-1.678 r/r_{\text{half}}}, \tag{4.2}$$

where $r_{\text{half}} \approx 1.678 r_0$ is the half–light radius (the radius that encloses half the flux), and de Vaucouleurs ($n = 4$) profiles (de Vaucouleurs 1948),

$$I(r) = \frac{F}{7! \, 8\pi r_0^2} e^{-(r/r_0)^{1/4}} \approx \frac{F}{0.011 r_{\text{half}}^2} e^{-7.670(r/r_{\text{half}})^{1/4}}. \tag{4.3}$$

`Tractor` uses the exponential and de Vaucouleurs profiles to define four different galaxy models. "REX" is a round exponential profile ($e1 = e2 = 0, n = 1$) with variable r_{half}; "EXP" is the exponential profile; "DEV" is the de Vaucouleurs profile, and "COMP" is a weighted combination of exponential and de Vaucouleurs with the same centroid.

For a given model $m(\theta)$ for a star or galaxy, `Tractor` estimates the parameters θ by maximizing the negative log likelihood $\mathcal{L}$ of the data x,

$$-\ln \mathcal{L}(x|m, \theta) = \sum_{i=1}^{N} \frac{(m(\theta)_i - x_i)^2}{2\sigma_i^2} \tag{4.4}$$

where N is the number of pixels in all g, r, z images overlapping the source, x_i is the per–pixel counts, and $1/\sigma_i^2$ is the per–pixel inverse variance. `Tractor` estimates model

parameters using maximum likelihood estimation. `Tractor` also assumes that there is no covariance between model parameters (i.e., the non–diagonal elements of the covariance matrix are zero), so the variance of each parameter estimate is estimated as,

$$-\mathrm{E}\left[\frac{\partial^2 \ln \mathcal{L}(x|m,\theta)}{\partial\theta^2}\right] \le \frac{1}{\mathrm{var}(\theta)}. \qquad (4.5)$$

We place very conservative constraints on the half–light radius ($\ln r_{\mathrm{half}} < 5$) and the variance of the ellipticity parameters (e1 and e2 are Gaussian distributed with $\sigma^2 = 0.25^2$), which are applicable to galaxies. The final step is model selection. After optimizing the parameters for each model, we compute a reduced χ^2 over all the pixels and select the model with the lowest reduced χ^2 per degree of freedom.

Many biases and systematics in model fitting and selection are possible. Pixels may not be independent, parameter uncertainties may be underestimated or biased in some way, various blending issues occur, such as not detecting the fainter of two sufficiently close sources, resolved galaxies and bright stars with diffraction spikes and ghosts are hard to model, etc. All of these biases and systematics may also depend on the type of source. `Obiwan` can test for each of these; for instance, we can inject simulated sources at random locations in the survey footprint and look at the distribution of parameters, comparing measured values (`Tractor`'s parameter estimates) to truth (the parameters of the sources we injected).

4.3.3 Optimizing `Obiwan`

Model fitting is the most time consuming stage of `Legacypipe`, so any optimizations must improve that stage. We get a factor of ~ 2 speedup by skipping all blobs that do not contain at least one injected source. Specifically, we tell `Tractor` the list of blobs to process, so skipping blobs only affects whether a source has a best–fit model not whether it was detected. `Obiwan` only cares about blobs containing injected sources, so this is a safe optimization.

4.4 Data

4.4.1 The Cosmic Evolution Survey (COSMOS)

The Cosmic Evolution Survey (COSMOS) used 600 orbits of the Hubble Space Telescope (HST) to image a two square degree patch of sky, at RA = 150.12 deg and Dec = 2.21 deg, to unprecedented depth (Scoville et al. 2007). Since then the COSMOS region has been observed at almost all wavelengths and is often used as reference truth for astronomical studies. The Dark Energy Camera Legacy Survey (DECaLS) (Dey et al. 2018) took many g, r, z exposures of the COSMOS region, exceeding the required depth many times over. The DECaLS Team grouped these exposures into independent g, r, z data sets and added

Table 4.1: Properties of the COSMOS subsets

Subset	Avg Seeing ($''$)		
	g	r	z
60	1.1	1.2	1.0
64	1.3	1.3	1.25
69	1.8	1.9	1.7

just enough noise to each to bring them to the DECaLS depth requirement. We make use of the independent data sets with the best, average, and worst seeing (subsets 60, 64, and 69, respectively) and refer to them as the COSMOS subsets (see Section 4.5).

4.5   Results

As a proof of concept of `Obiwan`'s ability to characterize biases and systematics in the Legacy Survey imaging data and the `Legacypipe` pipeline, we inject exponential and de Vaucouleurs galaxies with $r_{half} = 0.5''$ into each of the COSMOS subsets (see Section 4.4.1). Fig. 4.2 shows the footprint for each subset. These galaxies are of particular interest because the DECaLS depths are defined for exponential $r_{half} = 0.5''$ galaxies.

Table 4.5 lists the properties of these COSMOS subsets. These runs allow us to answer questions like, is `Legacypipe` successfully detecting sources that are as faint as expected? How accurate are the uncertainties on galaxy model parameters? Do these uncertainties depend on model selection? Are the ellipticity measurements good enough for weak lensing studies?

To sample the full parameter space, the simulated sources have a continuous uniform distribution of g, r, z AB magnitude 2 mag brighter and 0.5 mag fainter than each band's depth limit. The galaxies have fixed $r_{half} = 0.5''$, continuous uniform distributions for position angle and minor–to–major axis ratio, and an equal chance of having an exponential or de Vaucouleurs profile. Table 4.5 lists all of these properties.

4.5.1   Simulated Galaxies with $r_{half} = 0.5''$

Into each Cosmos subset, we inject 256k galaxies per deg^2 (71k per arcmin^2) via 16 independent Monte Carlo simulations of 16k galaxies per deg^2. Fig. 4.3 shows the g, r, and z magnitude histograms for the simulated galaxies (blue), and the shift to fainter magnitudes (green) from adding Galactic extinction (COSMOS is intentionally a low–extinction region, so these distributions are almost indistinguishable). The distribution of position angles (pa), minor to major axis ratios (ba), and corresponding ellipticity components (e2, e1) are shown in Fig. 4.4. Note, the uniform distribution in g, r, z will lead to simulated galaxies with colors unrepresentative of real galaxies. Chapter 4 uses a realistic joint distribution for emission line galaxy properties.

Table 4.2: Simulated Source Properties

Parameter	Distribution	Range
g	uniform	[22.0, 24.5] AB mag
r	uniform	[21.4, 23.9] AB mag
z	uniform	[20.5, 23.0] AB mag
r_{half}	–	0.5 arcsec
Sérsic n	binary	1 or 4
p.a.	uniform	[0. 180)
b.a.	uniform	[0.2, 1.0]

Note. — Properties below the dividing line only apply to extended sources.
p.a.: position angle.
b.a.: minor to major axis ratio.

For the best seeing Cosmos subset, Fig. 4.5 compares the number of injected galaxies to the number recovered by `Legacypipe`. This shows that `Legacypipe` is equally good at recovering exponential and de Vaucouleurs sources. The injected population is 50% exponential and 50% de Vaucouleurs, and `Legacypipe` recovers 37% of the exponentials and 37% of the de Vaucouleurs. Fig. 4.6 is a confusion matrix that shows the fraction of true exponential or de Vaucouleurs galaxies that Tractor models as type PSF, REX, EXP, DEV, or COMP sources. `Tractor` is biased towards exponential sources because 96% of true exponential sources are modeled as such (e.g., EXP or REX), while only 12% of truly de Vaucouleurs source are modeled as de Vaucouleurs. The other 88% of truly de Vaucouleurs sources are classified as REX (77%), EXP (6%), and PSF (4%). This bias is surprising because `Tractor` model selection penalizes EXP and DEV sources equally. These numbers are similar for the other Cosmos subsets.

`Obiwan` provides an independent measurement of depth: it is the magnitude of the source for which the chance of recovery (i.e., detecting it then deciding that it is a bonafide astrophysical source) is 50%. Fig. 4.7 shows the fraction of exponential $r_{\text{half}} = 0.5''$ galaxies that are recovered by `Legacypipe` versus source magnitude for the Cosmos subsets. Depth depends on more than just seeing so it is not surprising that the median seeing subset (subset 64) is slightly deeper than the best seeing subset (subset 60). The recovered fractions are ~ 75–80% for the brightest sources, which means that ~ 20–25% of the easiest to detect sources are lost to image quality, e.g., a combination of bright stars, bad pixels, source detection, etc. At the depth limits (horizontal lines), the recovered fractions are still high (~ 70–75%), which means that all three subsets exceed the required depth by at least 0.5 mag in all bands.

We use the Cosmos subset with the best seeing for the remainder of this analysis (e.g., Figs. 4.8 - 4.10). We test the accuracy of `Tractor`'s parameter estimates by comparing

the `Tractor` measured values for g, r, z flux, r_{half}, and ellipticity e1 and e2, to the true parameters of the sources we inject. We find that `Tractor`'s underestimates the true variance of its parameter estimates. Fig. 4.8 shows the number of standard deviations (N_σ) away from truth for each parameter that `Tractor` estimates. To get a crude estimate for how much `Tractor` underestimates the true variance, we assume that N_σ is Gaussian distributed and compare the sample standard deviation (σ_s) to unity. If `Tractor`'s estimate of the true variance is unbiased, then $\sigma_s \sim 1$. Fig. 4.8 shows that a Gaussian with $\sigma = \sigma_s$ (solid black) is considerably wider than the standard normal distribution (dashed black), for all parameters. Using the σ_s values, we conclude that `Tractor`́s measurement errors are underestimated by factors of ~ 1.7–2.0x for g, r, z flux, ~ 2.5–3.0x for r_{half}, and ~ 3.0–3.5x for ellipticity e1 and e2.

Fig. 4.8 also reveals a very large systematics offset in flux (~ 0.25 mag in all bands) and r_{half} ($\sim$4–5$''$ for EXP and DEV sources), which we remove by subtracting the mean. `Tractor` fluxes are too faint while `Tractor` r_{half} is too large. There is no systematic offset for the ellipticity e1 and e2 measurements. Reasons for these offsets are discussed in Section C.1.2.

We now compare the true g, r, z fluxes for the $r_{\mathrm{half}} = 0.5''$ galaxies with those measured by `Tractor`. Fig. 4.9 shows a 2D histogram of true and measured magnitude residuals versus the true magnitude, per–band, for all simulated galaxies recovered. `Tractor` measurements are systematically 0.25 mag fainter than truth. We suspect that this very large offset is due to either too small a stamp size for simulated sources (by `Obiwan`) or imperfect sky subtraction (by `Legacypipe`). Ignoring the offset, the interquartile range (yellow lines) shows that `Tractor`'s magnitude measurements have a standard deviation of about 0.25 mag for $r_{\mathrm{half}} = 0.5''$ galaxies at the DECaLS depth requirement.

Fig. 4.10 shows the same 2D histograms from Fig. 4.9 but with the number of standard deviations between the true flux and what `Tractor` measured (assuming `Tractor` inverse variances for the flux uncertainties), instead of residual magnitude. Unlike Fig. 4.9, fainter galaxies have less scatter (normalized by flux errors) than brighter ones. `Tractor`'s flux variances are accurate for galaxies at the DECaLS depth requirement, but should be at least 2x larger for galaxies 2 mag brighter than the depth requirement. `Tractor` fluxes are systematically smaller so we see the same offset as in Fig. 4.9.

4.6 Conclusions

We summarize our conclusions as follows:

1. We presented a new Monte Carlo method for characterizing imaging systematics in a joint analysis of astronomical images from multiple telescopes. We implemented this method for the Legacy Surveys image reduction pipeline, `Legacypipe`. We call our code `Obiwan` because it may be *the only hope*[1] for removing the anticipated suite of imaging systematics.

2. Our method adds simulated sources at random locations in astronomical images and then performs source detection and measurement, characterizing the complex selection inherent in large–scale–structure catalogs. The process is repeated until the injected source density is high enough to satisfy one's science objectives. For instance, the DESI target density for emission line galaxies (ELGs) is 2400 deg^2, so simulated ELGs should be injected at more than 10 times this density. We built `Obiwan` for the Legacy Surveys, but it is a general tool for analyzing multi–wavelength imaging data that is much needed by the astronomical community. Please visit its ReadTheDocs page: http://obiwan.readthedocs.io/en/latest/

3. `Obiwan` is unique because it adds sources to individual exposures and uses parametric likelihoods (no apriori knowledge of imaging systematics is needed).

4. We summarized the algorithms in `Legacypipe` and `Tractor` that are most susceptible to biases and systematics. We identified various biases and systematics by injecting 256k sources per deg^2 (71k per arcmin^2) with $r_{\mathrm{half}} = 0.5''$ and either exponential and de Vaucouleurs profiles into the COSMOS subsets. We found that `Tractor`'s measurement errors are underestimated by factors of ~ 1.7–2.0x for g, r, z flux, ~ 2.5–3.0x for r_{half}, and ~ 3.0–3.5x for ellipticity e1 and e2.
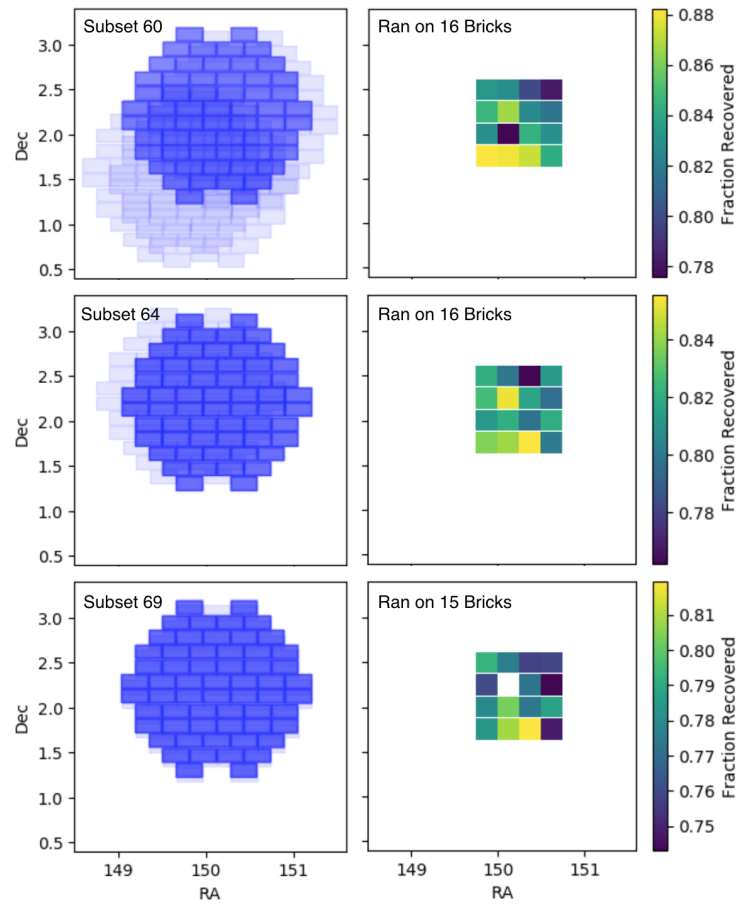
Figure 4.2: (Left Column) Footprint for the Cosmos subsets (dark blue regions) for $r_{\mathrm{half}} = 0.5''$ galaxies. (Right Column) The subset of the dark blue footprint that we ran `Obiwan` on (16 bricks). Colors correspond to the fraction of simulated galaxies recovered by `Legacypipe`. Note, there is a blank square in the bottom right panel because of an issue running one of the 16 regions in subset 69.
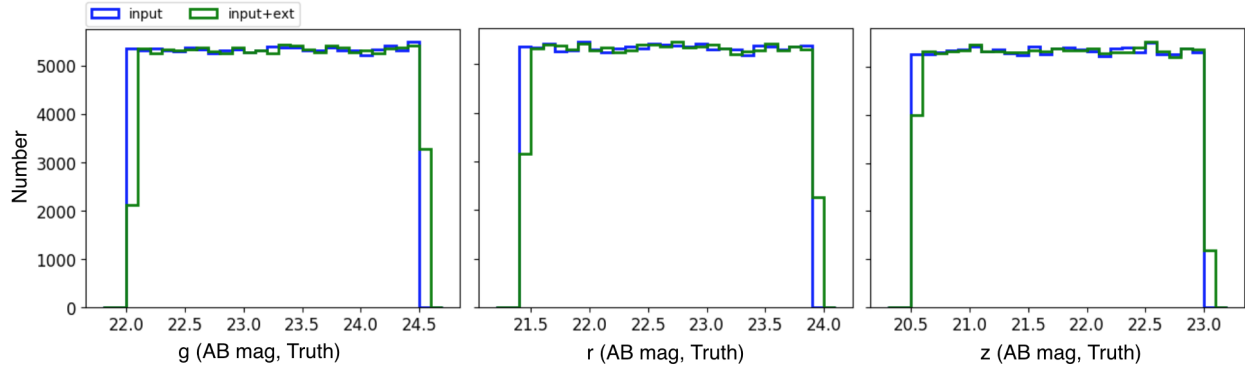
Figure 4.3: *g*, *r*, *z* magnitude of simulated galaxies with (green) and without (blue) Galactic extinction. Extincted sources are fainter, especially for bluer bands.

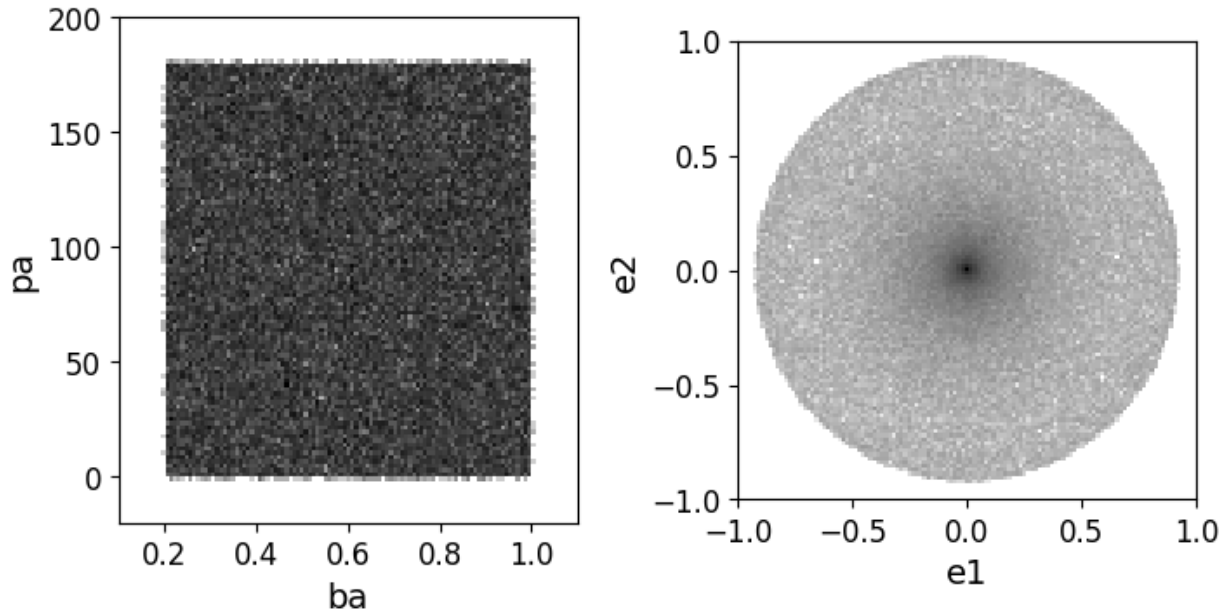*Figure 4.4*: Uniform distribution of position angle (pa) and minor to major axis ratio (ba) for simulated galaxies. The corresponding of ellipticity components (e2, e1) are on the right.
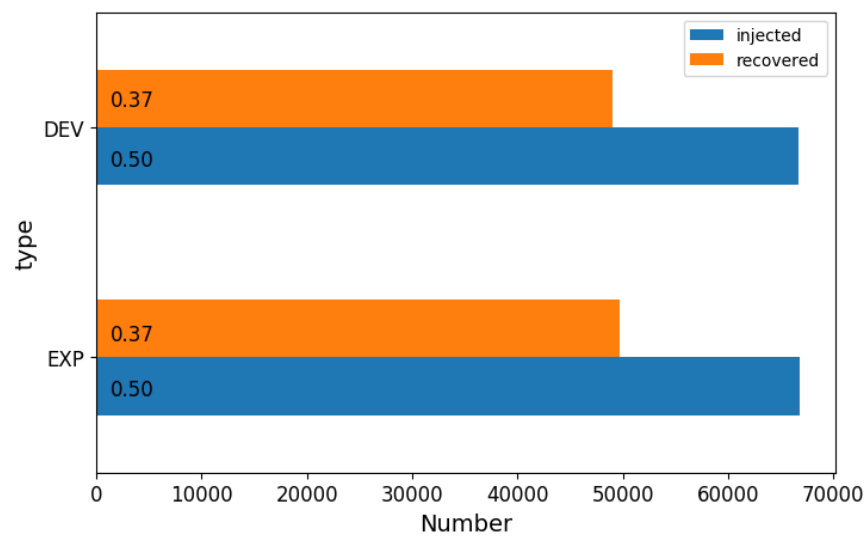
Figure 4.5: Barplot comparing the number of injected galaxies to the number recovered by `Legacypipe`. The plot suggests that `Legacypipe` is equally good at recovering exponential and de Vaucouleurs sources.
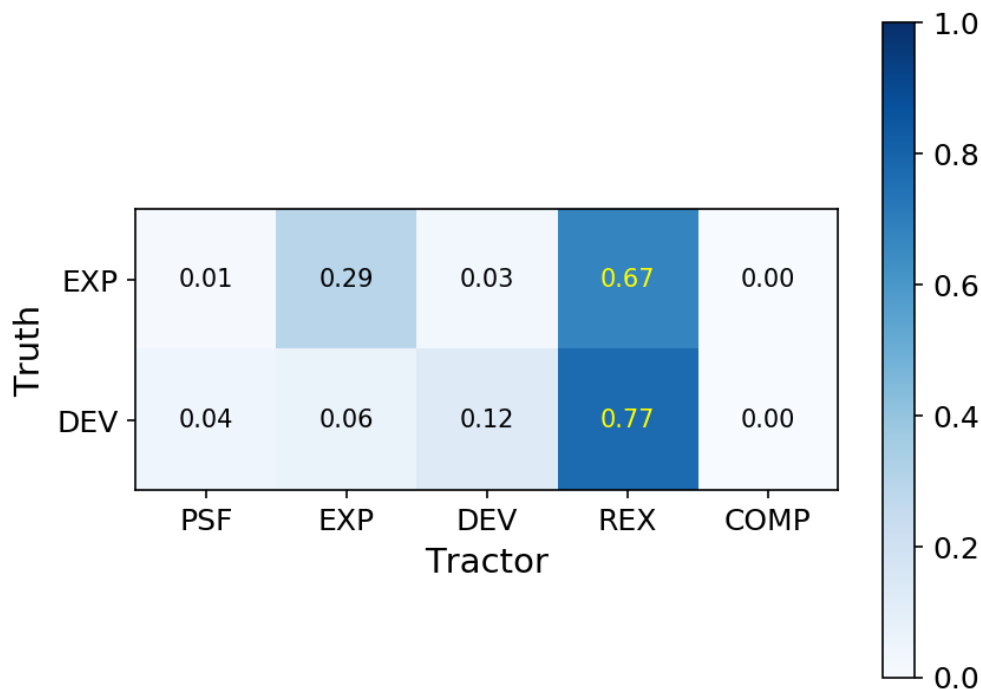
Figure 4.6: Confusion matrix showing the fraction of truly exponential or de Vaucouleurs galaxies that Tractor models as type PSF, REX, EXP, DEV, or COMP sources. `Tractor` is biased towards exponential sources.
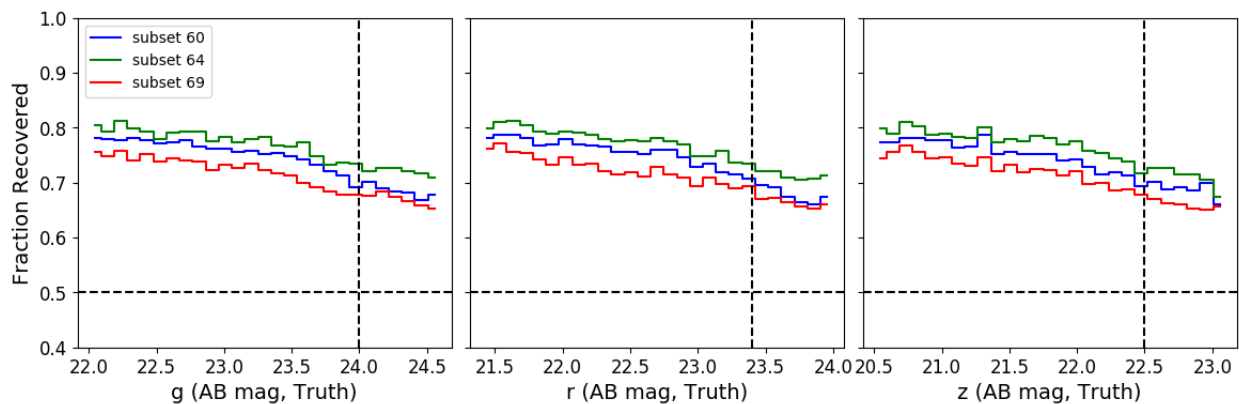
Figure 4.7: Fraction of simulated $r_{half} = 0.5''$ galaxies recovered by `Legacypipe` for the Cosmos subsets. A `Tractor`–independent measurement for depth is the magnitude at which the fraction (or chance of recovery) decreases to 0.5. This never happens, which means that all three subsets exceed the required depth in all bands by at least 0.5 mag.
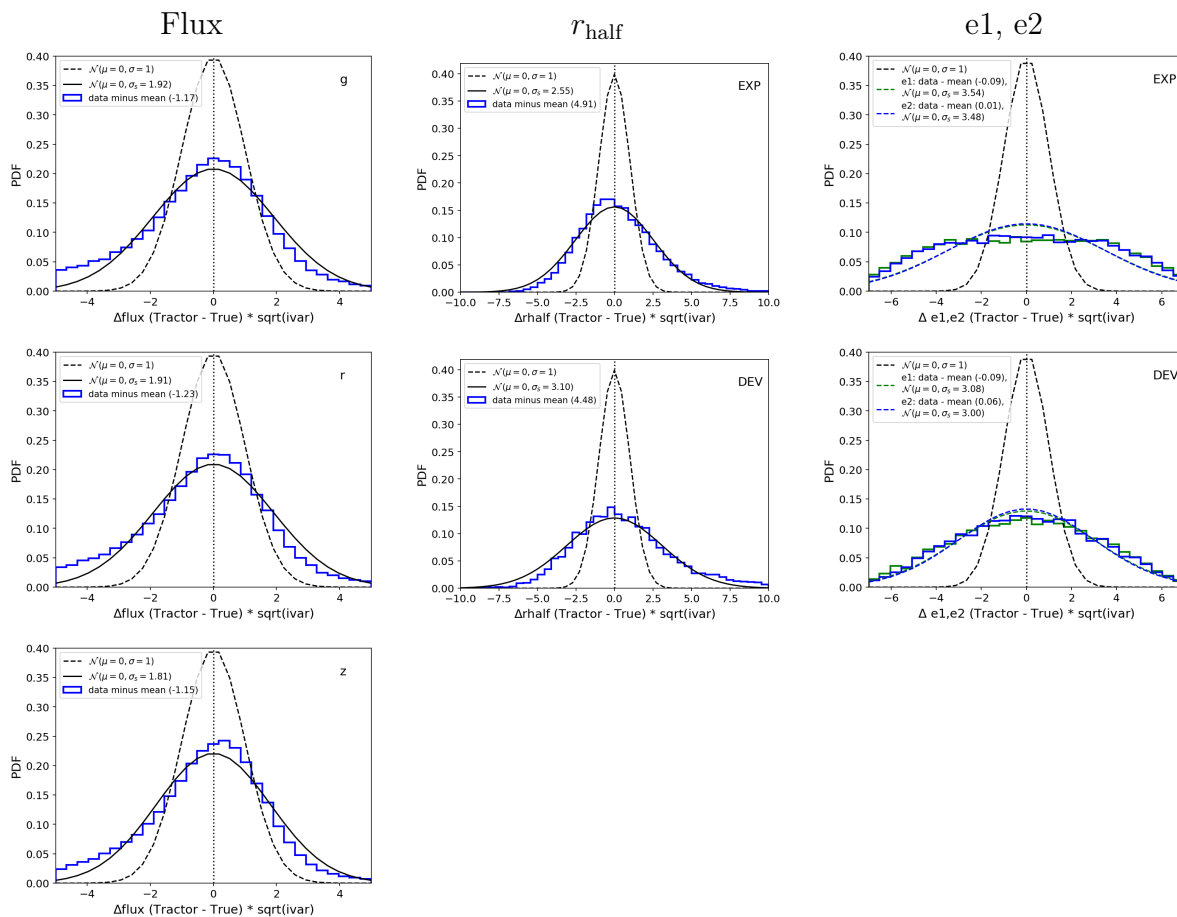
Figure 4.8: Number of standard deviations away from truth (N_σ) of the `Tractor` measured flux, r_{half}, and ellipticity. "ivar" is the inverse variance that `Tractor` estimates for each of its parameters. The mean of each distribution has been subtracted. To get a crude estimate for how much `Tractor` underestimates the true variance, we assume that N_σ is Gaussian distributed and compare the sample standard deviation (σ_s) to unity. (Left) N_σ for g, r, z flux. (Middle) N_σ for r_{half} for sources `Tractor` classifies as EXP and DEV. (Right) N_σ for ellipticity e1 and e2 for sources `Tractor` classifies as EXP and DEV.
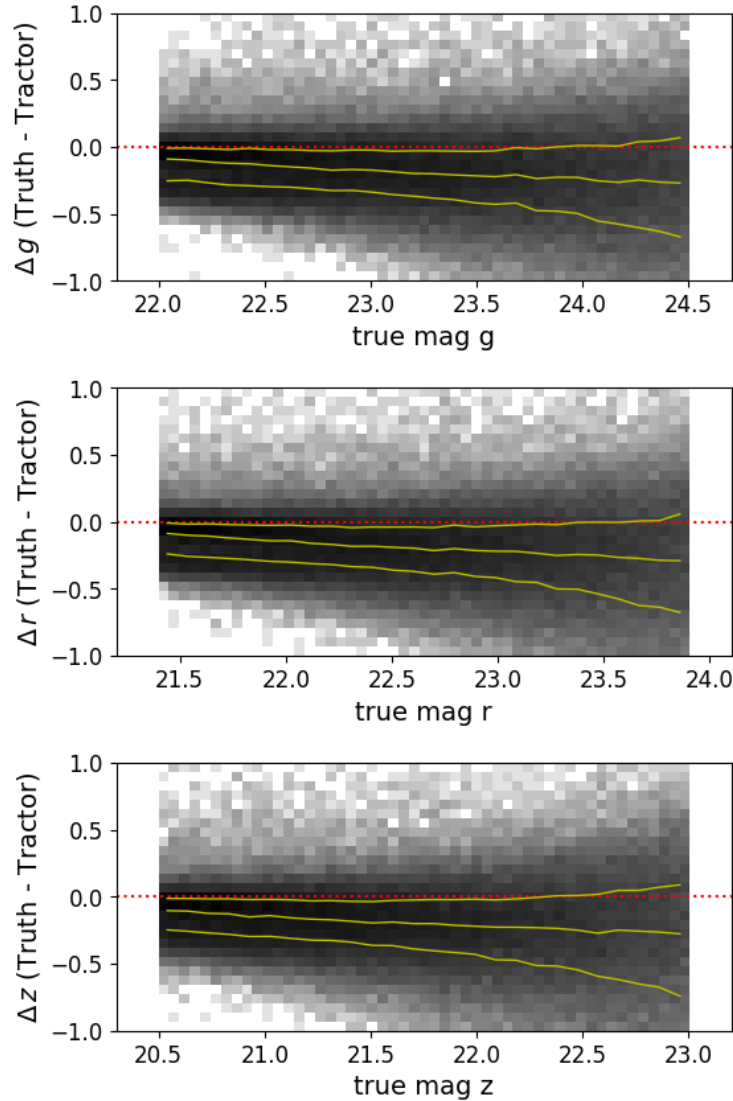
Figure 4.9: The 2D histogram of true and measured magnitude residuals versus the true magnitude, per–band, for all simulated galaxies recovered. Yellow lines correspond to the 25th, 50th, and 75th percentiles. `Tractor` measurements are systematically 0.25 mag fainter than truth, and we suspect that this is either too small a stamp size for simulated sources (by `Obiwan`) or imperfect sky subtraction (by `Legacypipe`). Ignoring the offset, the interquartile range shows that `Tractor`'s magnitude measurements have a standard deviation of about 0.25 mag for $r_{\mathrm{half}} = 0.5''$ galaxies at the DECaLS depth requirement.
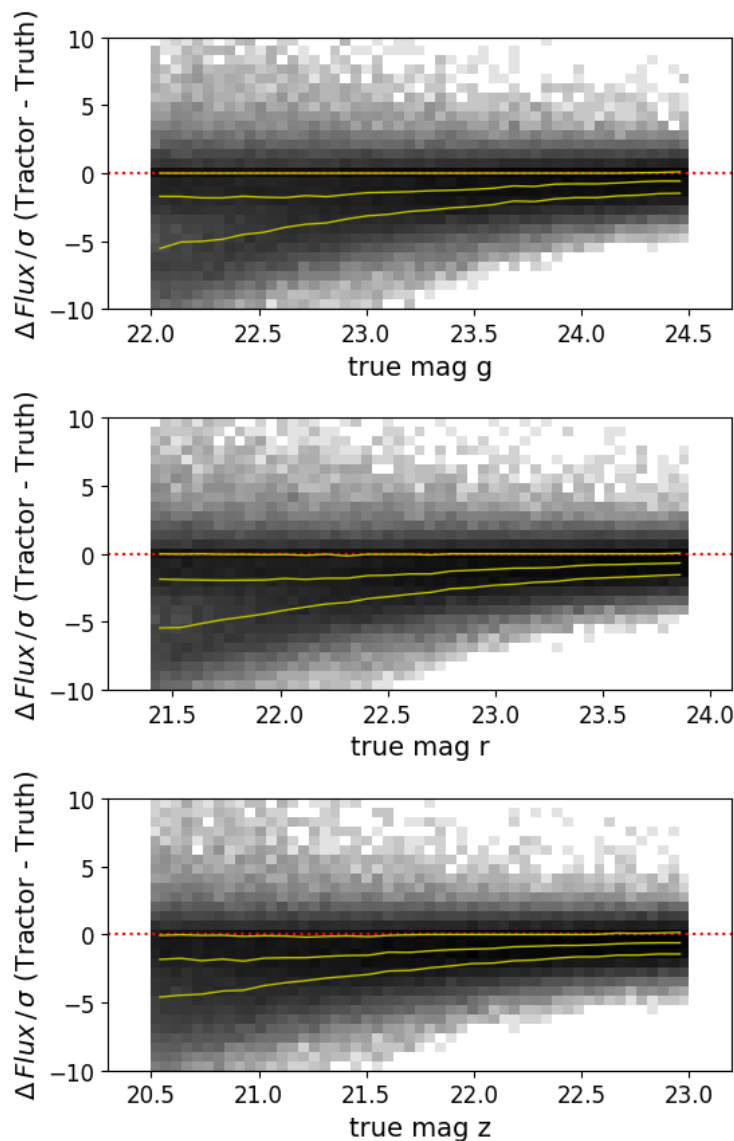
Figure 4.10: Number of standard deviations between the true flux and what `Tractor` measured (assuming `Tractor` inverse variances for the flux uncertainties) versus the true magnitude of the source. Yellow lines correspond to the 25th, 50th, and 75th percentiles. Fainter $r_{\mathrm{half}} = 0.5''$ galaxies have less scatter than brighter ones. `Tractor`'s flux variances are accurate for galaxies at the DECaLS depth requirement, but should be at least 2x larger for galaxies 2 mag brighter than the depth requirement. `Tractor` fluxes are systematically smaller so we see the same offset as in Fig. 4.9.

Chapter 5

Removing Imaging Systematics from the eBOSS ELG Sample with `Obiwan`

The work in this Chapter is in preparation and will be published as Burleigh et al. (2018c in prep.).

5.1 Chapter Abstract

Images of the night sky are transformed into a 3-dimensional large–scale–structure catalog by passing them through a pipeline that automatically detects and models galaxies and then obtaining spectra and measuring redshifts for a sample of the galaxies. Clustering statistics computed from large–scale–structure catalogs, such as the two–point correlation function, provide a measure of the expansion rate of the universe and can answer many fundamental questions about the universe. Biases and systematics in the large–scale–structure catalogs, due to the imaging data, must be removed to compute these clustering statistics; however, the current methods for removing them (e.g., map–based methods) are ill suited for the next generation of galaxy surveys, such as the Legacy Surveys. We propose a new method for removing imaging systematics that does not require maps of imaging systematics or foregrounds. We apply to this method to the eBOSS ELG sample using the `Obiwan` code (see Chapter 4), and derive an angular correlation function that both reproduces previous ELG correlation functions (Favole et al. 2016) and extends the correlation function to larger θ. This analysis is a preparatory step for analyzing imaging and spectroscopic data for the Dark Energy Spectroscopic Instrument (DESI)

5.2 Introduction

Astronomers perform galaxy surveys to measure how galaxies cluster at different times in the past. Clustering statistics, such as the three dimensional correlation function projected onto a sphere (the angular correlation function), provide a measure of the expansion rate of

the universe and can answer many other fundamental questions about the universe (Peebles 1980). Some of the most widely known galaxy–redshift surveys include the APM (Maddox et al. 1996), CfA (Huchra et al. 1999; Falco et al. 1999), SDSS (York et al. 2000), 2dFGRS (Colless et al. 2001b), WiggleZ (Drinkwater et al. 2010), BOSS (Dawson et al. 2013), and eBOSS (Dawson et al. 2016). Images of the night sky are transformed into a 2–dimensional large–scale–structure catalog by passing them through a pipeline that automatically detects and models galaxies and stars in the calibrated images. This becomes a 3–dimensional catalog by selecting galaxies that satisfy particular selection criteria and obtaining spectra and measuring redshifts for them. Clustering statistics are then computed from the positions of the galaxies on the sky and their redshifts.

Removing biases and systematics due to the imaging data (imaging systematics) is critical for measuring unbiased clustering statistics like the angular correlation function. Map–based methods, such as template subtraction and mode projection (Elsner et al. 2016), have successfully removed imaging systematics from the SDSS, WiggleZ, BOSS, and eBOSS surveys; however, it is unlikely that these methods, in their current state, will be able to handle the complexities of future and ongoing galaxy surveys, such as the Legacy Surveys. Map–based methods use a pixelization scheme, such as HEALPIX (Górski et al. 2005), to subdivide the sky into equal–area pixels and then compute various per–pixel quantities: the number of galaxies in the large–scale–structure catalog (data), the average seeing, sky brightness, exposure time, etc. (imaging meta–data) and galactic extinction (foregrounds). The non–data maps are potential imaging systematics and are turned into pixel weight maps (in configuration space) or mode weights (in Fourier space). The weights mimic how the angular selection function samples the true distribution of galaxies yielding the observed large–scale–structure catalog (Elsner et al. 2016).

The two most popular map–based methods are "template subtraction" (Myers et al. 2006a,b; Ross et al. 2011; Ho et al. 2012; Ross et al. 2012, 2017; Blake et al. 2010; Delubac et al. 2017; Laurent et al. 2017; Prakash et al. 2016; Myers et al. 2015; Elvin-Poole et al. 2017) and "model projection" (Rybicki & Press 1992; Tegmark et al. 1998; Slosar et al. 2004; Elsner et al. 2016; Leistedt et al. 2013). Template subtraction is a model for how the number of galaxies depends on each systematic. In pixel space, the data is divided by the model; in Fourier space, the model is subtracted from the data. To avoid modeling chance correlations, only the systematic maps with the largest data cross correlation are modeled. Mode projection treats the systematic maps as adding noise to each mode in Fourier space or pixels in configuration space, so that values in the data covariance matrix are increased for modes where each systematic map is large. It robustly models the impact of the linear combination of the systematics, but does not include non–linear effects from the systematics.

These map–based methods are ill suited for the next generation of galaxy surveys, such as the Legacy Surveys (Dey et al. 2018). For example, a substantial fraction (2–10%) of the data is removed because the number of observed galaxies deviates significantly from the mean due to regions near bright stars, observations at high airmass or particularly bad seeing. There are many systematics to test for, only the systematics known apriori can be modeled, and it is unclear how to make systematics maps for regions of the sky with varying

amounts of repeat imaging. For example, Elvin-Poole et al. (2017) created 21 systematic maps to model systematics in their DECam imaging data. Such methods also ignore biases or systematics introduced by the pipeline that created the large–scale–structure catalog. Large–scale–structure catalogs from the Legacy Surveys require a joint analysis of images from three telescopes. Each telescope will obtain multi– and same–band images of the same part of the sky that are separated by month to year time baselines. The CCD detectors also have similar angular size (0.5 to 2 deg) to the BAO signal signal (~ 5 deg at redshift of 1).

We present a new method for removing imaging systematics at the individual exposure level from future and ongoing surveys that does not require maps of imaging systematics, foregrounds, or other apriori knowledge, and that corrects for biases and systematics in the software pipeline that produced the large–scale–structure catalog. We apply our method to DECam data from the Legacy Surveys using the `Obiwan` code (Burleigh et al. in prep.). We inject realistic emission line galaxies (ELGs) into the DECam images used to create for DR3–era `Tractor` catalogs, which the eBOSS Team used to select ELG targets (Raichoor et al. 2017). We use `Obiwan` to perform Monte Carlo simulations of how the `Legacypipe`/`Tractor` pipeline (Lang et al. in prep) detects and models eBOSS ELG–like galaxies. `Obiwan` is very similar to the `BALROG` (Suchyta et al. 2016), which injects sources into coadded DECam images and builds a large–scale–structure catalog using `Source Extractor`; however, `Obiwan` is unique in that it operates on individual exposures and (by virtue of `Legacypipe` and `Tractor`) maximizes the likelihood of the data to find the best model parameters for its sources. Benefits of using individual exposures and maximum likelihood (not heuristic) techniques are discussed in Burleigh et al. (in prep.).

Our goal is compute the angular correlation function for eBOSS ELGs, with and without `Obiwan`, to estimate the impact of this method on eBOSS science requirements. This is also a preparatory step towards future analysis of the Dark Energy Spectroscopic Instrument (DESI) ELG sample, because DESI will select targets using Legacy Surveys data and its five–year survey is significantly more complicated than eBOSS (DESI Collaboration 2016a,b). All data products are available at NERSC (see Section C.3).

This Chapter is structured as follows. In § 5.3, we describe the imaging and spectroscopic data we use and the eBOSS ELG target selection criteria. In § 5.4, we summarize how `Obiwan` and `Tractor` work, the algorithms we use for removing imaging systematics, and the angular correlation function is estimated from a large–scale–structure catalog. In § 5.5, we present our `Obiwan` Monte Carlo simulations of the imaging data used to select eBOSS ELGs, and the resulting angular correlation functions. We conclude in § 5.7. The Appendix presents biases and systematics in the Legacy Surveys image reduction pipeline, and the additional information needed to reproduce our `Obiwan` Monte Carlo simulations.

5.3 Data

5.3.1 The DECam Legacy Survey (DECaLS)

The DECaLS is a g, r, z-band survey of 9,000 deg^2 of the southern sky using the Blanco 4-m telescope and DECam camera[1] in Cerro Tololo, Chile. DECam has a field of view of 3.18 deg^2 and is a mosaic of 62 CCDs, each having 4096x2046 pixels, with pixel scale of 0.262″ pixel^{-1}. The DECaLS depth requirements are 1–2 mag deeper than the SDSS. For more details see Dey et al. (2018) and Chapter 2.

The first round of eBOSS ELG target selection (Raichoor et al. 2017) used a combination of DR3[2] `Tractor` catalogs and a set of reprocessed DR3 `Tractor` catalogs (produced by the eBOSS team) that included DECam images observed after the DR3 March 2016 cutoff. We will refer to these as the DR3–plus catalogs. The list of DECam CCDs used to create the DR3–plus catalogs is available online.[3] Fig. 5.1 shows these CCDs and the approximate eBOSS NGC and SGC regions (blue boxes).

5.3.2 eBOSS ELG Target Selection

eBOSS selected ELGs from DR3–plus `Tractor` catalogs having clean DECaLS photometry, locations outside bright star masks, sufficient g–flux to be [O II] emitters and star forming galaxies, and $g - r$ and $r - z$ color associated with galaxies in the desired redshift range of $0.5 - 2$. The eBOSS ELG footprint is split into the two regions (blue boxes) shown in Fig. 5.1. The regions include 620 deg^2 in the South Galactic Cap (SGC) and 600 deg^2 in the North Galactic Cap (NGC). ELGs in the SGC are selected using by the following `Tractor` catalog cuts,

- `brick_primary = True`

- `decam_anymask[grz] = 0`

- $21.825 < g < 22.825$

- $-0.068\,(r - z) + 0.457 < g - r < 0.112\,(r - z) + 0.773$

- $0.218\,(g - r) + 0.571 < r - z < -0.555\,(g - r) + 1.901$

The NGC cuts are identical except for,

- $21.825 < g < 22.9$

- $0.637\,(g - r) + 0.399 < r - z$

---

[1]http://www.ctio.noao.edu/noao/content/DECam-Observing-Manual
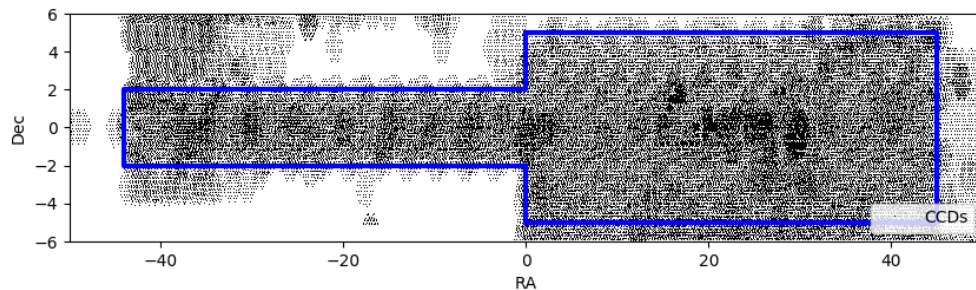[2]http://legacysurvey.org/dr3
[3]http://portal.nersc.gov/project/desi/users/kburleigh/obiwan/legacysurveydir_ebossdr3
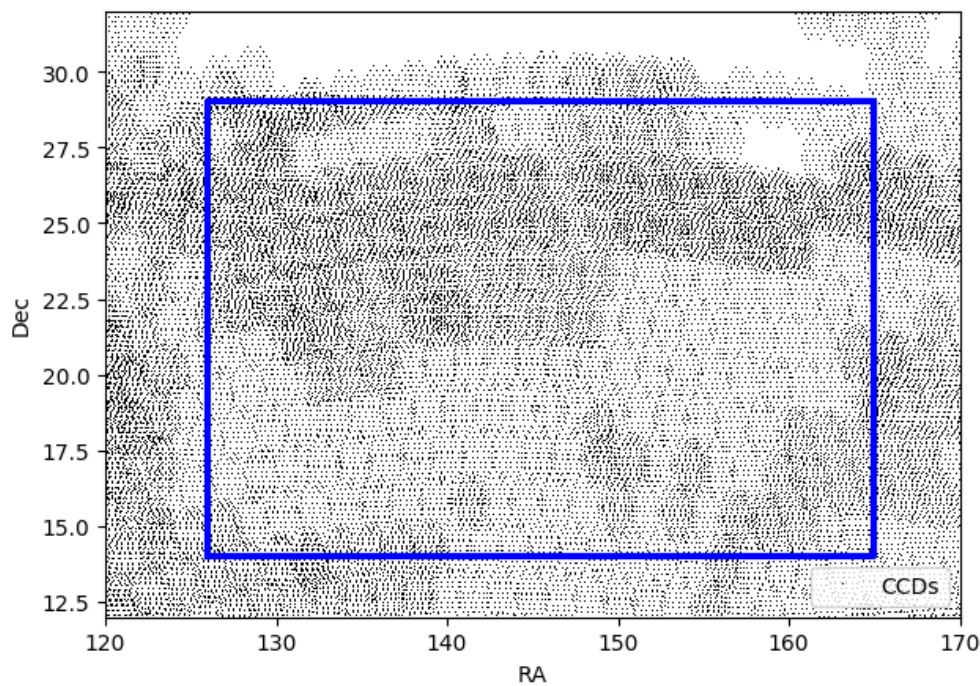
(a) NGC

(b) SGC

Figure 5.1: The eBOSS NGC and SGC footprints (blue boxes) and the DECaLS CCDs used to create the DR3–plus `Tractor` catalogs.

Bright star masks are also applied. For more details see Raichoor et al. (2017).

It was later discovered that `decam_anymask[grz] = 0` is magnitude dependent and removes many good ELG candidates. `decam_allmask[grz] = 0` should have been used instead. Identifying and removing the biases and systematics introduced `decam_anymask[grz] = 0` has proven difficult; fortunately, our `Obiwan` Monte Carlo simulations will resolve this problem because they estimate the angular selection function for ELGs in the given set of DE-CaLS images, and `decam_anymask[grz] = 0` can be trivially applied (or not) to the resulting large–scale–catalogs.

5.3.3 Joint Tables of eBOSS Spectra and `Tractor` catalog Measurements

To build a representative sample of eBOSS ELG galaxies (see § 5.4.2), we use the following joint tables of eBOSS 21, 22, 23 spectra and associated DR3–plus `Tractor` catalog measurements,

- `eBOSS.ELG.obiwan.eboss21.v5_10_4.fits`

- `eBOSS.ELG.obiwan.eboss2122.v5_10_7.fits`

- `eBOSS.ELG.obiwan.eboss22.v5_10_4.fits`

- `eBOSS.ELG.obiwan.eboss23.v5_10_4.fits`

- `eBOSS.ELG.obiwan.eboss23.v5_10_7.fits`

We cut to spectroscopically confirmed galaxies (`z_flag` = 1), and drop NGC sources (about 30% of the sample) because the NGC `Tractor` catalogs are incomplete at $g \sim 23.8$ mag (see Fig. C.10). We will refer to these as the eBOSS–`Tractor` tables.

5.3.4 The DEEP2 Galaxy Redshift Survey (DEEP2)

DEEP2 obtained about 50,000 high resolution (R $\sim$ 6000) spectra of redshift ~ 1 galaxies using the DEIMOS multi–object on Keck 2 (Newman et al. 2013). The DEEP2 footprint is 2.8 deg^2, split into four disjoint regions: Field 1 (14hr), Field 2 (16h), Field 3 (23h), and Field 4 (02h). We create a DEEP2 (DR4) and DECaLS DR3 matched table by finding the nearest DR3 `Tractor` catalog source within a $1''$ search radius of each DEEP2 spectrum. The DECaLS DR3 footprint does not overlap Field 1, so our table only includes Fields 2–4. We refer to it as the DR3–DEEP2 table and use it in § 5.4.2.

5.3.5 Mock Catalogs of ELG Clustering

Most ELG galaxy samples are incomplete in stellar mass and/or emission line flux, so their clustering properties are hard to model using simulations (Comparat et al. 2013). However, Favole et al. (2016) showed that this incomplete sampling of ELGs can be modeled by combining existing photometric and spectroscopic data with the latest MultiDark N–body simulations (Klypin et al. 2016) and by changing how the (Sub)Halo–Abundance Matching method (Conroy et al. 2006; Klypin et al. 2013) assigns galaxies to (simulated) dark matter halos. They conclude that their mock catalogs, which we will refer to as the ELG mock catalogs, have the correct angular and redshift–space clustering for ELGs having redshifts of $0.6 < z < 1$. In Section 5.5.2, we compare the angular correlation function of the ELG mock catalog to our `Obiwan` measurements for eBOSS ELGs.

5.4 Methods

5.4.1 `Obiwan`

We add simulated sources, with properties closely matched to the galaxies of interest, to random locations in the imaging data and then run the relevant source detection and measurement software. By measuring how the simulated sources are lost and recovered we can estimate the angular selection function of the galaxy survey. This enables us to downsample an initially random distribution of galaxies, based on the selection function, and to compare resulting distribution to the observed galaxy sample. We call our method `Obiwan`, since it may be the only hope of accounting for the aforementioned imaging systematics.

`Obiwan` modifies the g, r, z images that `Legacypipe` operates on by adding simulated sources to the individual exposures and appropriately modifying the inverse variance images. The simulated sources include poisson noise from the source itself. The power of `Obiwan` is that the injected sources inherit the sky background, systematics, or whatever else is present in the data, so nothing more than the simulated galaxy or star of interest is injected. `Legacypipe` does not know the images have been modified; source detection, model fitting, and model selection proceed as usual. For more details see Chapter 4.

Fig. 5.2 compares real and simulated galaxies that have exponential profiles and relatively bright g–band magnitudes. These are eight galaxies, out of 130k eBOSS 21, 22, 23 ELG SGC targets and 1.2M injected ELGs, that are relatively bright in g–band. Their color and high S/N are not representative of the full distribution; however, based on Fig. 5.2 and visual inspection of many more galaxies that span the full distribution, we cannot tell the difference between the real and simulated ELGs.

`Obiwan` performs a Monte Carlo Simulation by injecting the simulated galaxies at random RA and Dec, running `Legacypipe`, and repeating for the same images. Blending can occur between pairs of real–real, real–simulated, and simulated–simulated sources. Our goal is to simulate effects involving galaxies, so we prevent blending between simulated–simulated sources. We temporarily set aside all simulated sources that would be within $5''$ of another simulated source, and injected those set–aside sources during the next Monte Carlo iteration. Blending between real and simulated sources is allowed (and needed to fully simulate the angular selection function). This $5''$ criterion only applies to pairs of simulated sources. The initially random galaxy positions are modified by the geometry of the footprint, source detection, measurement, target selection, and any biases and systematics in the `Legacypipe` pipeline. We will refer to these as `Obiwan`–randoms, and the truly random galaxy positions (e.g., the RA, Dec for all the sources we tried to inject into the imaging data) as uniform–randoms.

5.4.2 Injecting Realistic ELGs

This section summarizes how we generate the representative sample of eBOSS ELG–like galaxies that we inject into the images. A representative sample is crucial to the success of
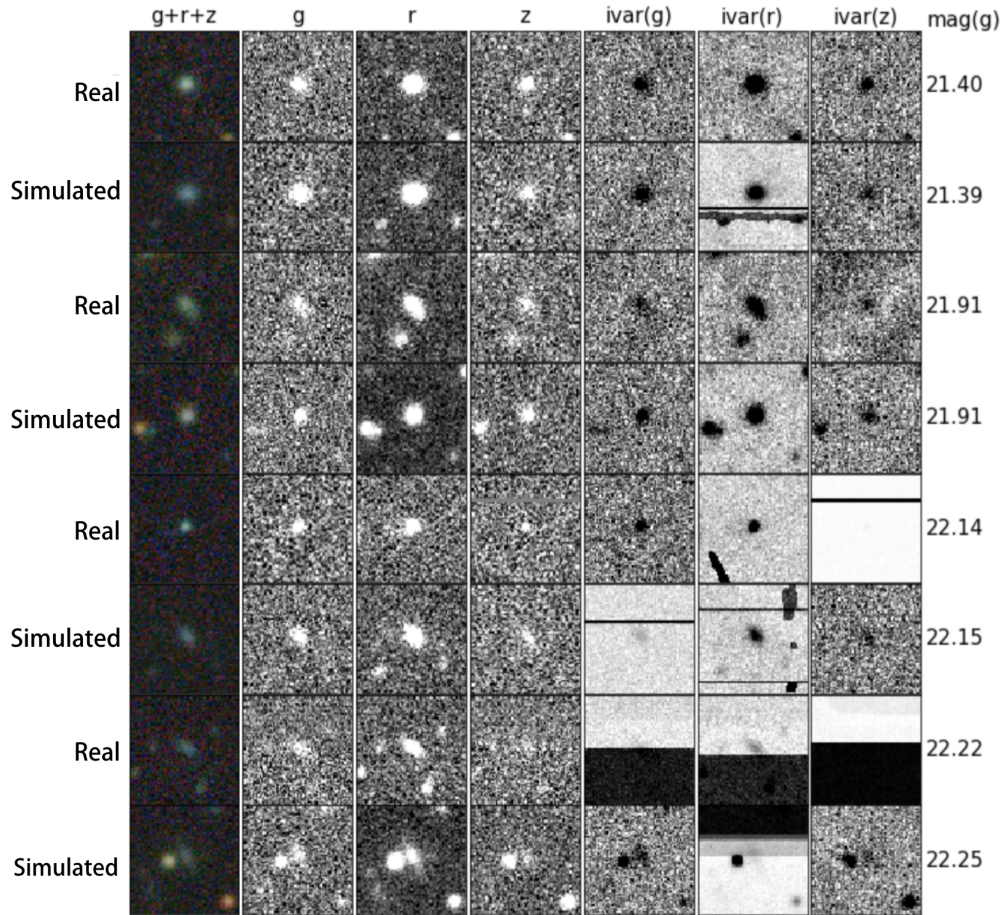
Figure 5.2: Comparison between real and simulated galaxies having exponential profiles and relatively brighter *g*–band magnitudes. The label for each image is on the left and its corresponding *g* magnitude is the number on the right. Each row is a single galaxy. The first column is a three color jpeg for easy visualization. The remaining columns are the per–band full resolution coadded *g*, *r*, *z* images and associated inverse variance maps. Consecutive rows of R and F (rows 1 and 2, 3 and 4, etc.) have similar *g* magnitude for a fair comparison.

our method because we can only use the randoms if they truly mimic the properties of the real galaxies we are interested in.

We use the eBOSS–`Tractor` tables to build a sample of eBOSS ELG targets having a redshift, shape, and *g*, *r*, *z* flux. DEV galaxies are systematically larger and about 1 mag brighter than EXP in all bands (see Fig. C.9), so we split the sample into separate DEV and EXP samples. The final "eBOSS sample" has 77,525 EXP and 7,439 DEV galaxies. See Section C.2.1 for more details.

To simulate contamination we need to inject ELGs that are just outside the eBOSS ELG color box and *g*–mag boundaries. We find that DEEP2 is a complete galaxy survey in the

sense that it contains the eBOSS ELG selection. The DR3–DEEP2 galaxies reproduces the brightness, shape, and redshift distributions of the eBOSS sample (see Section C.2.2), so we use it to construct a sample of ELGs that are within 0.2 mag of the eBOSS ELG color box and g–mag boundaries. The final "DR3–DEEP2" sample has 1,064 EXP and 85 DEV galaxies. See Section C.2.2 for more details.

We now describe our algorithm to jointly sample an eBOSS n(z) redshift and its associated brightness, shape, and size using our eBOSS and DR3–DEEP2 samples. The eBOSS n(z) is the redshift distribution of spectroscopic redshifts from the eBOSS–`Tractor` tables weighted by spectroscopic completeness (1/TSR). To sample from n(z), we intentionally over–fit a 10 component Gaussian Mixture Model (GMM).

We draw redshifts from n(z), dropping those outside the allowed redshift range [0,2], until there are N redshift samples. For each redshift, we find its nearest redshift in our (EXP–DEV combined) DR3–DEEP2 sample. By finding the nearest redshift we hope to preserve the redshift dependence on galaxy brightness, shape, and size. We decide whether each galaxy should have an exponential or de Vaucouleurs profile using the following chance model. We define an ELG as passing eBOSS ELG SGC target selection. If the redshift–brightness–shape sample is an ELG, we find its nearest redshift in the EXP eBOSS sample (90% of the time) or the DEV eBOSS sample (10% of the time); if not, we trim the DR3–DEEP2 sample to galaxies that extend beyond the eBOSS ELG selection boundaries, and find its nearest redshift in the trimmed EXP DR3–DEEP2 sample (90% of the time) or the trimmed DEV DR3–DEEP2 sample (10% of the time). This yields a sample of eBOSS ELG–like galaxies with the desired redshift distributed. See Section C.2.3.

5.4.3 Run `Obiwan` on the DECam CCDs used to Select ELG Targets for eBOSS

We use `Obiwan` to inject simulated galaxies into the DECam CCDs used to create the DR3-plus `Tractor` catalogs. We use the current version of `Legacypipe`, not the two year-old version that actually created the DR3-era `Tractor`catalogs. We do not expect this to bias our results because we find excellent agreement between DR3 and DR5 measurements for the same sources. We configure `Obiwan` to run `Legacypipe` with the `--simp` option, which uses the SIMP model instead of REX, and to explicitly use all the input CCDs (used to create the DR3-era `Tractor` catalogs and to select the eBOSS ELG targets).

5.4.4 The Angular Correlation Function

The correlation function is a statistic that measures the clustering of galaxies, relative to a uniform random distribution on the unit sphere, for a range of galaxy–galaxy separations (Peebles 1980; Hamilton 1993; Weinberg et al. 2013; Norberg et al. 2009; Sawangwit et al. 2011; Favole et al. 2016). The two–point correlation function (2PCF), $\xi(r)$, uses the 3D positions (RA, Dec, and redshift) of the galaxies, while the angular correlation function (ACF), $w(\theta)$, uses the 2D positions (RA and Dec). For $\xi(r)$, one must adopt a cosmological

model to convert RA, Dec, and redshift to comoving coordinates. A power law is often assumed for $\xi(r)$,

$$\xi(r) \propto \left(\frac{r}{r_0}\right)^{-\gamma}, \tag{5.1}$$

where r_0 is the characteristic separation between galaxies. For small angles ($\theta \ll 1\,\mathrm{rad} \approx 60\,\mathrm{deg}$) the angular correlation function is also a power law (Limber 1953),

$$w(\theta) \propto \theta^{1-\gamma}, \tag{5.2}$$

if the redshift distribution of the galaxy sample varies more slowly than other functions of redshift in Eqn. (5.1). Eqn. (5.2) is known as the Limber approximation. For ELGs, $\gamma \sim 1.6 - 1.8$ and $r_0 \sim 4$ Mpc h^{-1} (Weinberg et al. 2013; Favole et al. 2016). We will use the ACF to gauge the scientific impact of Obiwan on eBOSS science.

The joint probability of finding two galaxies in solid angle $d\Omega_1$ and $d\Omega_2$ separated by angle θ is given by (Peebles 1980; Sawangwit et al. 2011)

$$dP(\theta) = n^2[1 + w(\theta)]d\Omega_1 d\Omega_2, \tag{5.3}$$

where n is the surface density of galaxies. The ACF is how much more (or less) likely we are to find a galaxy than we would if they were uniformly randomly distributed on the unit sphere. The minimum variance estimator for the ACF is (Landy & Szalay 1993),

$$\begin{aligned} w(\theta) &= 1 + \frac{N_R(N_R - 1)}{N_D(N_D - 1)}\frac{DD}{RR} - 2\left(\frac{N_R - 1}{N_D}\right)\frac{DR}{RR} \\ &\approx 1 + \left(\frac{N_R}{N_D}\right)^2 \frac{DD}{RR} - 2\left(\frac{N_R}{N_D}\right)\frac{DR}{RR}. \end{aligned} \tag{5.4}$$

where DD is the number of real galaxy–real galaxy pairs with separation between θ and $\theta + \Delta\theta$, RR is the number of random–random pairs, and N_D and N_R are the total number of real galaxies and randoms in the data set, respectively. Computing the correlation function reduces to pair–counting three samples of points for different pair separations (θ).

We will estimate the ACF using Jackknife sampling. For each bin in θ, we estimate the average of the ACF, $\overline{w(\theta)}$, over the full survey footprint. To estimate the variance of our $\overline{w(\theta)}$ measurement, i.e., the square of the standard error, we divide the footprint into N$_{sub}$ equal area regions. This yields N$_{sub}$ different subsamples each with area $(N_{sub} - 1)/N$ times that of the footprint. The variance of our N$_{sub}$ $w(\theta)$ estimates is $\sigma^2_{\mathrm{w}(\theta),\mathrm{Jack}}$,

$$\sigma^2_{\mathrm{w}(\theta),\mathrm{Jack}} = \frac{N-1}{N}\sum_i^N (w_i(\theta) - \overline{w(\theta)})^2, \tag{5.5}$$

This is equivalent to k–fold cross validation using $k = N_{sub}$ and spatially chosen subsamples, instead of random. Too many subsamples (i.e., subsamples with too small an area) results

in dependent subsamples and limits the maximum θ that $w(\theta)$ can be measured for; too few subsamples leads to a large variance on $w(\theta)$. For a Gaussian distribution, the standard error on an estimate of the standard deviation (σ) is std. error $\approx \sigma/\sqrt{2(N-1)}$ (Rose & Smith 2002). For $N_{sub} = 50$, the relative standard error on $\sigma_{w(\theta),\text{Jack}}$ is 10% (Norberg et al. 2009). Norberg et al. (2009) tested the accuracy of various estimators for $\sigma_{w(\theta)}$, using N–body simulations, and found that Jackknife estimates are biased on small ($< 10\ h^{-1}$ Mpc) scales, overestimating $\sigma_{w(\theta)}$ by up to 25%.

Chance fluctuations (aka Poisson noise, shot noise, or cosmic variance) in $DD(\theta)$ and $RR(\theta)$ also contribute to $\sigma_{w(\theta)}$,

$$\sigma^2_{w(\theta),\text{Chance}} = \frac{1}{DD(\theta)}[1 + w(\theta)]^2. \tag{5.6}$$

There is no $RR(\theta)$ term as long as substantially more randoms than real galaxies are used when computing the correlation function (Sawangwit et al. 2011).

5.5 Results

5.5.1 Run `Obiwan` on the DECam CCDs used to Select ELG Targets for eBOSS

We inject 1.2M simulated galaxies (i.e., randoms), at a density of 2800 per deg^2 into the DR3–era CCDs for both the NGC and SGC regions. About 50%, or 1400 per deg^2, of the injected galaxies pass the eBOSS NGC ELG target selection. The eBOSS ELG target densities in the NGC and SGC are 200 and 240 per deg^2, respectively, so our randoms galaxy sample (before source detection and `Tractor`, measurement) has 7–14x the density of the real galaxy sample. Fig. 5.3 shows the histograms of injected number density including footprint geometry and removing injected sources that are within $1''$ of an existing (real) source in the DR3–era `Tractor` catalogs. The maximum injected number density is 2800 per deg^2, but the mean is less than this (~ 2200 per deg^2) because we remove simulated galaxies from our final catalog that are within $1''$ of DR3–era `Tractor` sources. The distribution is bimodal because bricks at the edge of the footprint cannot receive as many sources, and areas are computed over the entire brick.

Fig. 5.4 shows the g, r, and z mag histograms for the simulated galaxies before and after adding galactic extinction (left column), the distribution of injected r_{half} (right top), and the distribution of ellipticity components e1, e2 (right middle). Galactic extinction is strongest for bluer wavelengths and it makes g magnitudes about 0.1 mag fainter. The mode for galaxy sizes is $r_{\text{half}} = 0.5''$ because `Tractor` models most galaxies as type SIMP; ignoring this mode, the r_{half} distribution extends from 0.2 to $2''$ with mean of $0.8''$. These ellipticity components correspond uniform distributions for the position angle $[0, 180)$ and minor to major axis ratio $[0.2, 1.0]$. Fig. 5.5 shows that `Legacypipe` is equally good at recovering exponential and de Vaucouleurs sources. The injected galaxies are 89% exponential and

11% de Vaucouleurs, and `Legacypipe` recovers 76% of the exponentials and 73% of the de Vaucouleurs.

The large–scale–structure catalog, which results from running `Obiwan` on our simulated galaxy sample, contains true positives, false positives, and false negatives. True positives (recovered ELGs) are simulated ELGs that remain eBOSS ELGs using `Legacypipe`'s measurements for them. False positives (contaminants) are simulated non–ELGs that pass target selection after `Legacypipe` measures them. False negatives (lost ELGs) are simulated ELGs that are either not detected (non–detections), have sufficient `Tractor` measurement error to fail target selection (measurement error), or overlap CCD edge(s) and are removed by the `fracin` cut (edge–overlap, see Section C.1).

Fig. 5.6 shows the g, r, z magnitude distributions for the recovered ELGs, contaminants, and lost ELGs. ELGs lost to measurement error are, on average, the faintest of the simulated galaxies in g, r, and/or z. Contaminants and ELGs lost to non–detections and edge–overlap are a minority of the sample and have similar g, r, z mag distributions. Fig. 5.7 shows the colors for recovered ELGs, contaminants, and lost ELGs. The top right panel shows the eBOSS color box. Most contaminants start at top left of the color box and scatter by ~ 0.25 mag to larger $g - z$ (redder) color. measurement error is the primary way that ELGs are lost. The colors of ELGs lost to non–detections are distributed over the full color box, so non–detection does not appear to correlate with color. ELGs lost to edge–overlap appear to have the same color distribution as full sample because whether or not a source overlaps a CCD edge does not depend on flux.

We inject ELGs with the appropriate correlations among brightness, shape, and redshift. Fig. 5.8 shows how the injected n(z) is modified by `Legacypipe`. The top panel shows that redshifts $z < 0.2$ and $z > 1.4$ are lost. The bottom panel shows that contaminants primarily enter at three redshift ranges: $z < 0.25$, $0.5 < z < 0.75$, and $1.2 < z < 1.35$.

5.5.2   The Angular Correlation Function

To compute the angular correlation function with and without `Obiwan`, we select galaxies (DD) from the DR3–plus catalogs[4] and randoms (RR) from either the `Obiwan`–randoms or uniform–randoms catalogs. We apply the eBOSS ELG NGC cuts in Section 5.3.2, the veto masks from Raichoor et al. (2017), and these cuts to remove sources in low depth imaging,

- `psfdepth_g` > 62.797

- `psfdepth_r` > 30.057

- `psfdepth_z` > 11.0

We restrict the DD and RR datasets to the eBOSS 23 footprint and Dec > 14.05, since this is where the datasets overlap the most. The angular separation (θ) between a pair of points

---

[4]https://data.sdss.org/sas/ebosswork/eboss/sandbox/lss/catalogs/versions/1_1/eBOSS_ELG_full_ALL_v1_1.dat.fits

with (RA$_1$, Dec$_1$) and (RA$_2$, Dec$_2$) is,

$$\theta = \cos(\psi_1)\cos(\psi_2)\left[\cos(\phi_1)\cos(\phi_2) + \sin(\phi_1)\sin(\phi_2)\right] + \sin(\psi_1)\sin(\psi_2), \qquad (5.7)$$

where $\psi = (-\text{Dec} + 90)\,\pi/180$ and $\phi = \text{RA} \times \pi/180$. We compute the ACF using the Landy & Szalay (1993) estimator (see Eqn. 5.4). We compute $w(\theta)$ at 27 evenly spaced logarithmic θ bins, centered between 10^{-2} and 5 deg. The mean redshift of the eBOSS ELG n(z) is $z \sim 0.8$. For a ΛCDM cosmological model with $\Omega_K = 0$ and $\Omega_m = 0.3$, this corresponds to ~ 50 Mpc per degree, so our θ bins span ~ 0.5–250 Mpc.

Fig. 5.9 (top panel) compares the ACF for Obiwan–randoms (the new method proposed in this chapter) to that for uniform–randoms (when $RR(\theta)$ is only modified by the footprint geometry). The Obiwan–randoms ACF agrees well with the ELG mock catalog ACF (orange), while the uniform–randoms ACF is too large. Weighting by θ (middle and bottom panels) shows that the Obiwan–randoms ACF behaves reasonably for $\theta \le 5$ deg, while the ELG mock catalog ACF breaks down for $\theta > 1$ deg. This breakdown occurs because the mean (but not the variance) of the ELG mock catalog ACF is biased for $\theta > 0.5$ deg (Favole et al. 2016). Obiwan's improvement over uniform–randoms is particularly evident for $\theta > 0.1$ deg.

Each data point in Fig. 5.9 is the average ACF, $\overline{w(\theta)}$. We estimate the uncertainty on each point using Jackknife sampling and $N_{sub} = 20$ equal area subsamples (Healpix pixels). As discussed in Section 5.4.4, the Jackknife method is biased on small (< 10 Mpc) scales, where it overestimates $\sigma_{w(\theta)}$ by up to 25% (Norberg et al. 2009). We ignore this effect because we are interested in the correlation function on large (BAO) scales. Further, the drastic improvement in the ACF, due to Obiwan, occurs for $\theta > 0.1$ deg. This is at large scales because 0.1 deg corresponds to ~ 10 Mpc, for a ΛCDM cosmological model with $\Omega_K = 0$ and $\Omega_m = 0.3$.

5.5.3 Weight-based Methods

Although computing the angular correlation function with Obiwan does not require weight maps, various weight maps can be derived from Obiwan's results. The maps can be used by map–based methods for removing imaging systematics or to create "mocks" (i.e., mock data sets from N–body simulations for the evolution of dark matter in the universe) for estimating the variance of arbitrary ACF measurements.

We limit ourselves to the following three weight maps:

- *Recovered*: the fraction of all injected sources that `Legacypipe` detects and measures

- *Recovered NGC–ELGs*: fraction of true NGC eBOSS ELGs that `Legacypipe` detects and measures and that have `Tractor` measurements that pass NGC eBOSS ELG target selection

- *Anymask–Allmask–Ratio*: using `Tractor` measurements, the ratio of the number of sources that pass NGC eBOSS ELG target selection using `allmask_grz = 0` to the number of when using `anymask_grz = 0`

The resolution of each weight–map is the brick–scale of $\sim 0.25 \times 0.25$ deg. Fig. 5.10 shows these three weight maps from top to bottom.

In the Recovered map, lower fractions are generally due to fewer CCDs (see Fig. 5.1); however, the Recovered NGC–ELG map is more complicated as lower fractions occur in regions with few CCDs (top right) as well as in regions with many CCDs (bottom left). The Recovered NGC–ELG map shows that only 20–40% of true NGC ELGs end up passing eBOSS NGC ELG target selection. The fraction is so low because it includes all of the losses due to bright stars and bad–pixels, blending, and source detection and `Tractor` measurement error for galaxies with ELG brightness and color distributions. The Anymask–Allmask–Ratio map shows that the `anymask_grz = 0` cut always selects fewer ELGs than `allmask_grz = 0` and that this reduction is enhanced where there are more CCDs (i.e., deeper imaging does not necessarily help). On average, `anymask_grz = 0` is a 10% effect, but in regions with more CCDs it can be as large as 40%. Most concerning is that the 40% effect also occurs over the entire footprint and that it appears to be periodic on scales of ~ 1–5 deg. Remember, the BAO signal at redshift 1 is ~ 5 deg. Using just eBOSS ELG data it is unclear how to propagate the effects of the `anymask_grz = 0` cut, so `Obiwan` may prove crucial to eBOSS ELG science.

5.6   `Legacypipe` Biases and Systematics

Our `Obiwan` eBOSS data reveal many biases and systematics in the `Legacypipe` pipeline. These are high impact items for the Legacy Surveys, but they are not relevant to this study. We direct the interested reader to Section C.1.

5.7   Conclusions

We summarize our conclusions as follows:

1. We proposed a new method for removing imaging systematics from galaxy survey data that does not require maps of imaging systematics or foregrounds, and that reduces any biases and systematics in the pipeline producing the large–scale–structure catalog.

2. We applied to this method to the eBOSS ELG sample using the `Obiwan` code described in Chapter 4. The resulting angular correlation function reproduces the ELG mock catalog correlation function (Favole et al. 2016) for $\theta < 1$ deg, and extends the correlation function to $\theta < 5$ deg.

3. We estimated the g, r, z–mag distributions for recovered ELGS (true ELGs that remain ELGs after source detection and measurement), contaminants (non–ELGs that pass target selection after detection and measurment), and lost ELGs (ELGs that are not detected, fail target selection after measurement, or overlap CCD edges). We also

investigated how much scattering occurs (~ 0.25 mag) into and out of the eBOSS ELG color box and g–band mag limits.

4. We provide weight maps of imaging systematics that can be used by map–based methods to remove imaging systematics and reproduce our results. This includes a map of the ratio of the number of sources that pass ELG target selection using `allmask_grz = 0` to the number when using `anymask_grz = 0`, a result that may be crucial to eBOSS ELG science.

5. Finally, we identified numerous biases and systematics in the Legacy Surveys image reduction pipeline, `Legacypipe`. The highest impact ones are that `Legacypipe` under-estimates the uncertainty on g, r, and z flux by a factor of 1.75–2, the uncertainty on r_{half} by a factor of 3–5, and the uncertainty on e1 and e2 by a factor of 2.7–3.
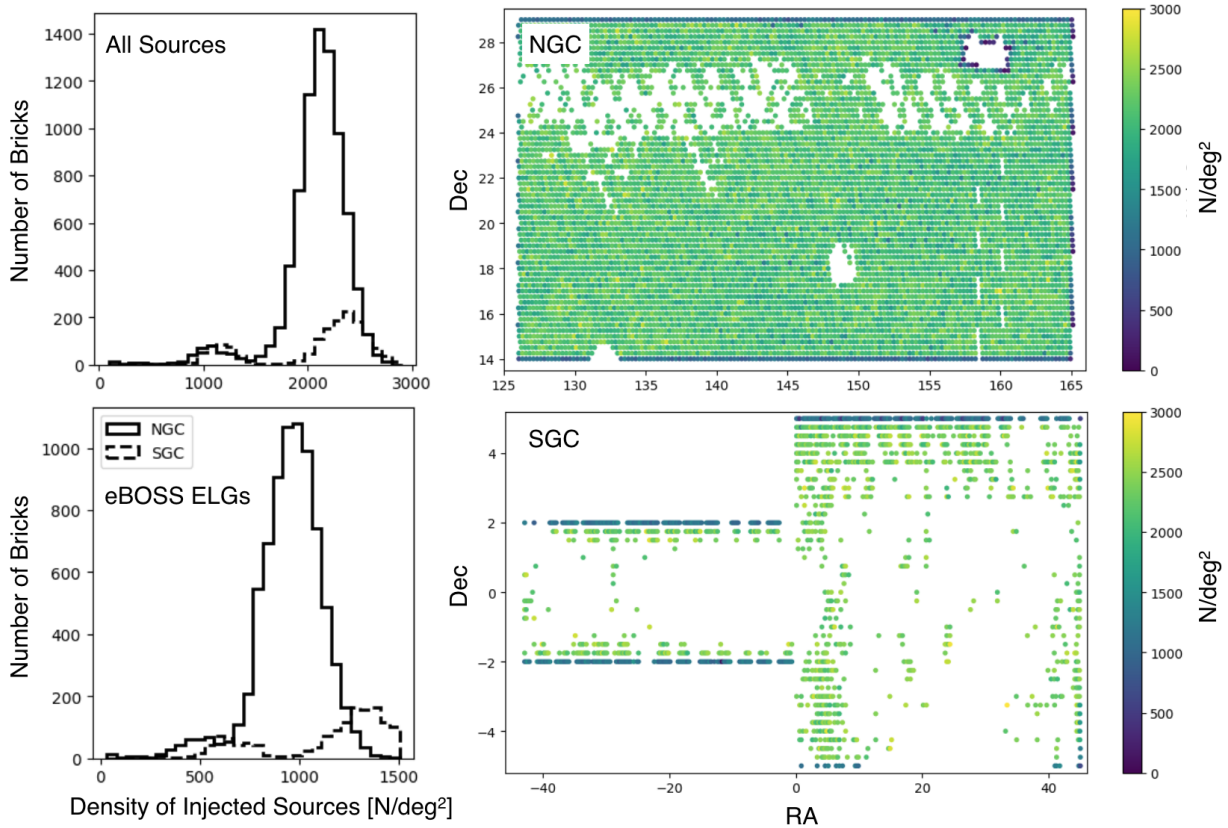
Figure 5.3: Number density of injected galaxies. (Right Column) Heatmaps showing number density of all injected sources in the NGC (top) and SGC (bottom) footprints. (Left Column) Number densities per brick of injected sources in the NGC (solid) and SGC (dashed). The panels are for all sources (top) and eBOSS ELGs (bottom). The distributions are bimodal because bricks near footprint edges or holes have fewer sources. The smaller mode corresponds to bluer points in the right column.
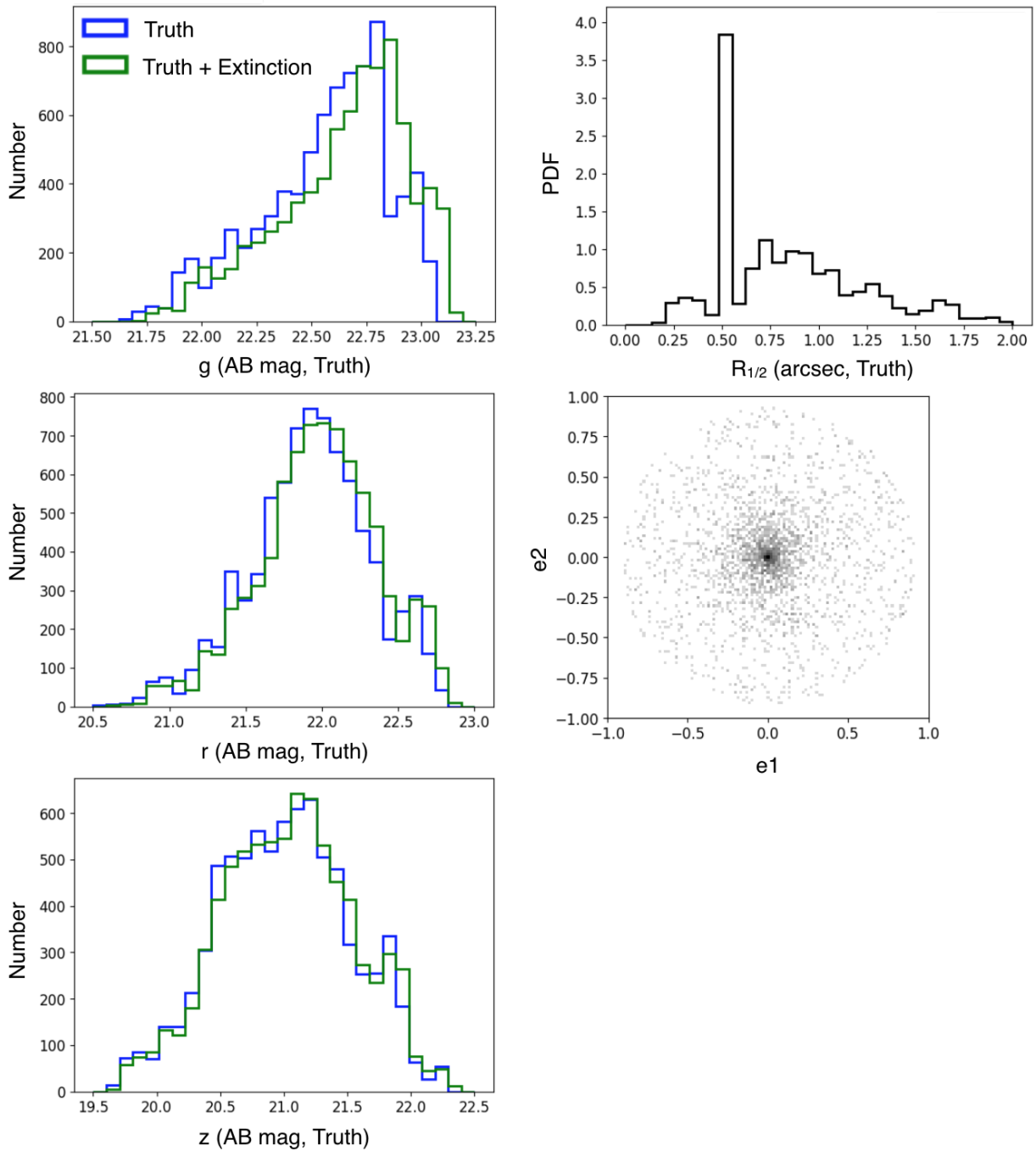
Figure 5.4: (Left Colum) g, r, z magnitude of injected sources (blue) and after adding galactic extinction to them (green). Extincted sources are fainter and the effect is stronger for bluer bands. (Right Top) r_{half} of injected sources. (Right Middle) Ellipticity components, e2 versus e1, of injected sources.
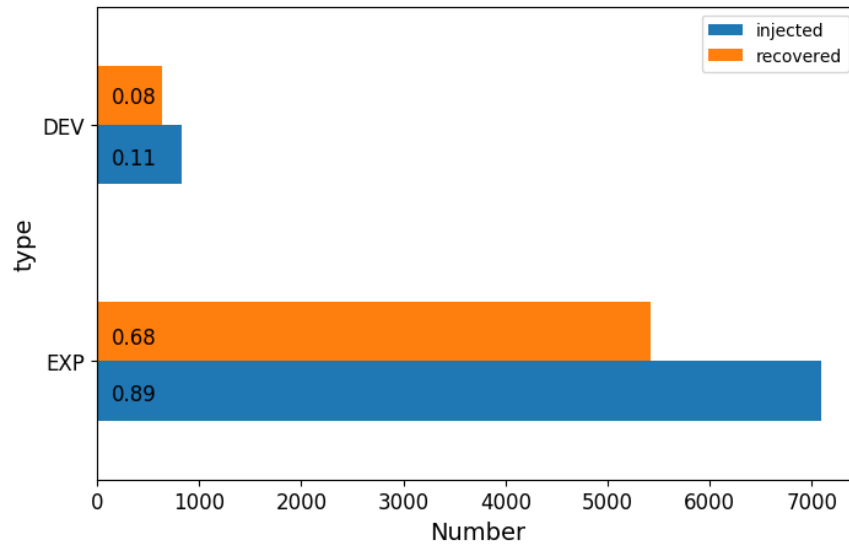
Figure 5.5: Barplot comparing the number of injected galaxies to the number recovered by `Legacypipe`. The injected population is 89% exponential and 11% de Vaucouleurs, and `Legacypipe` recovers 76% of the exponentials and 73% of the de Vaucouleurs. This suggests that `Legacypipe` is equally good at recovering exponential and de Vaucouleurs sources.
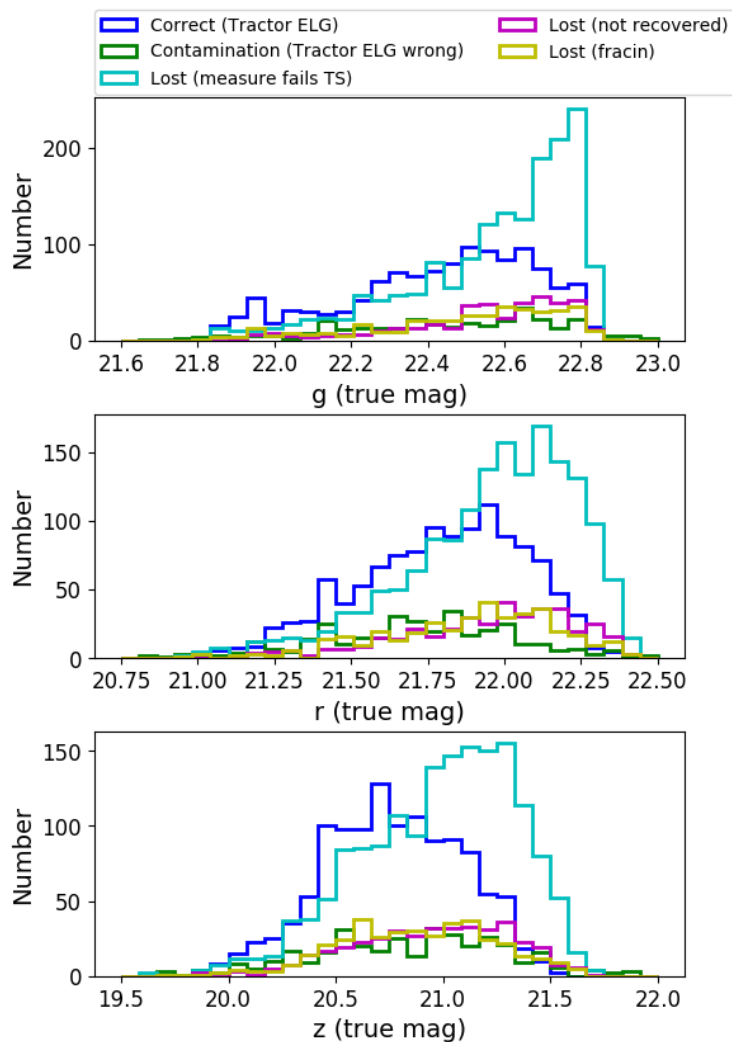
Figure 5.6: g, r, z magnitude histograms for the recovered ELGs, contaminants, and lost ELGs. ELGs lost to measurement error are, on average, the faintest of the simulated galaxies in g, r, and/or z. Contaminants and ELGs lost to non–detections and edge–overlap are a minority of the sample and have similar g, r, z mag distributions.
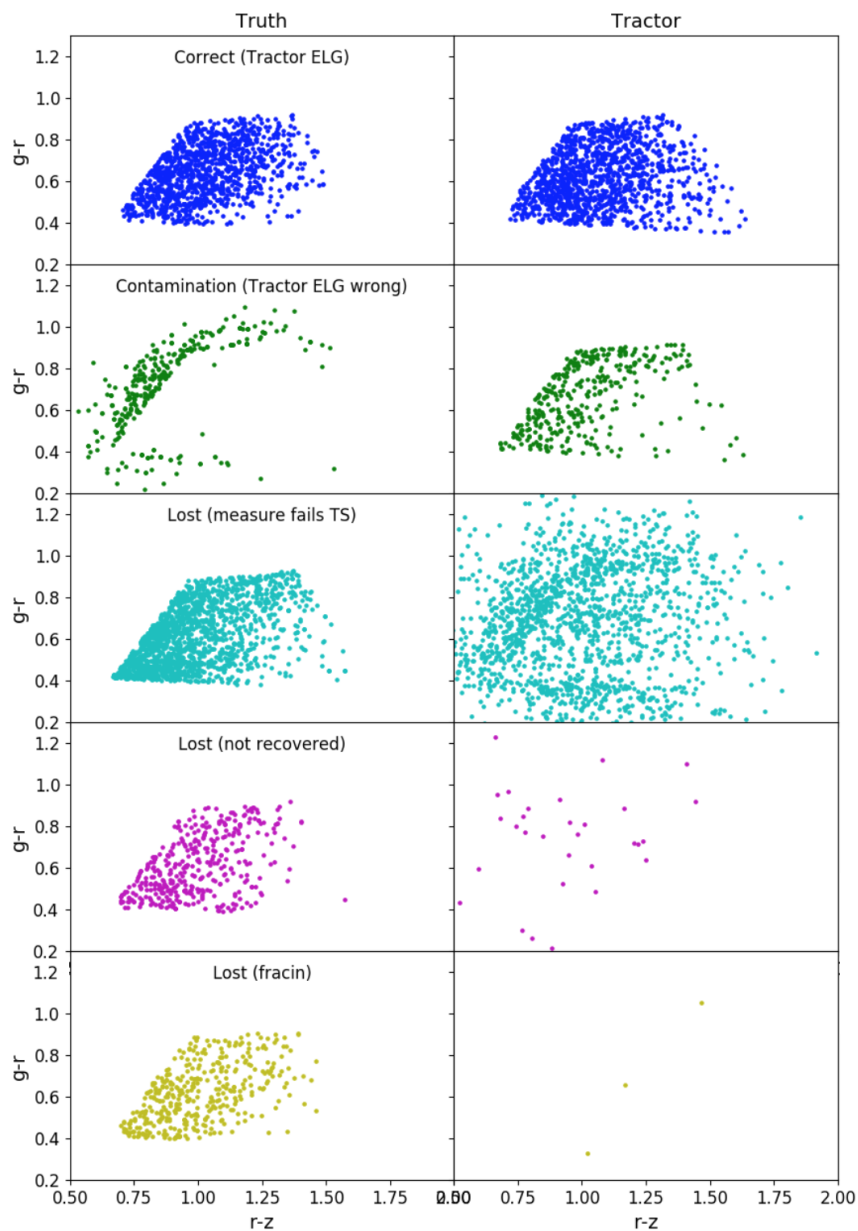
Figure 5.7: Distributions of recovered ELGs, contaminants, and lost ELGs for the eBOSS color box, using the color scheme from Fig. 5.6. (Left) true color of source. (Right) `Tractor` measured color. From top to bottom are recovered ELGs (blue), contaminants (green), ELGs lost to measurement error (cyan), ELGs lost to non–detections (magenta), and ELGs lost to edge–overlap (yellow).
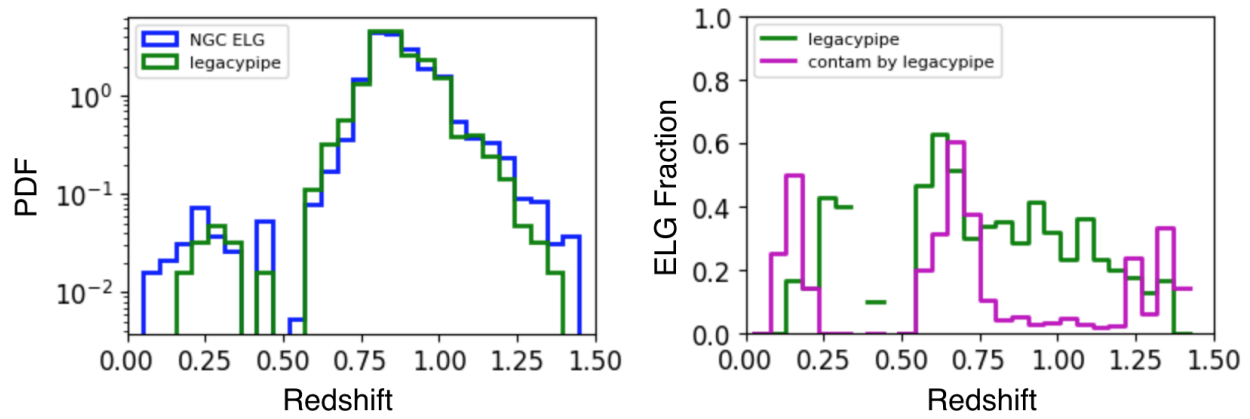
Figure 5.8: How `Legacypipe` modifies $n(z)$. (Left) Redshift PDF for injected galaxies (blue) compared to what ends up in the `Tractor` catalog created by `Legacypipe` (green). (Right) The fraction of sources in each redshift bin that are true eBOSS ELGs (green) and contaminants (magenta). Contaminants primarily enter at three redshift ranges: $z < 0.25$, $0.5 < z < 0.75$, and $1.2 < z < 1.35$.
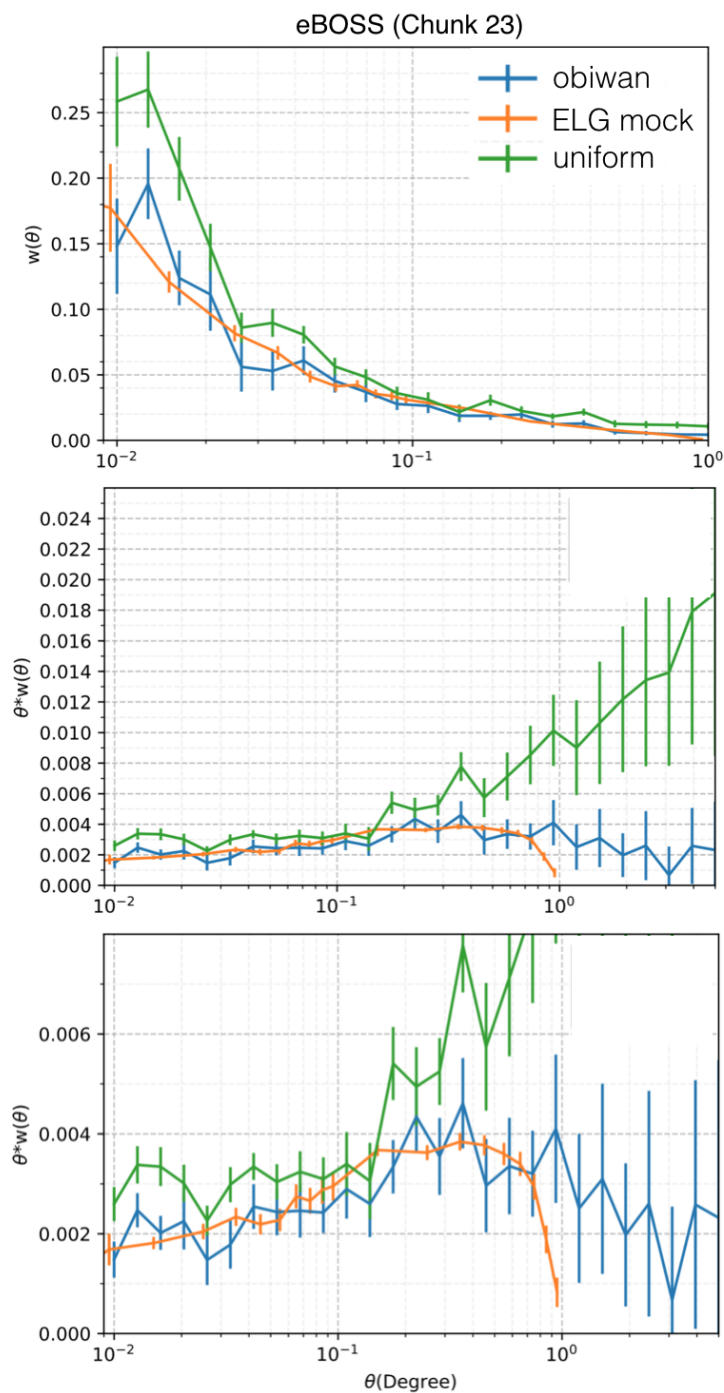
Figure 5.9: Angular correlation functions. Blue uses `Obiwan`–randoms for RR and is the new method proposed in this chapter, green uses uniform–randoms for RR, and orange is the ELG mock catalog correlation function. We use 27 evenly spaced logarithmic θ bins, centered between 10^{-2} and 5 deg. (Top) $w(\theta)$ versus θ. (Middle) $\theta \times w(\theta)$ versus θ. (Bottom) Zoom in on middle plot.
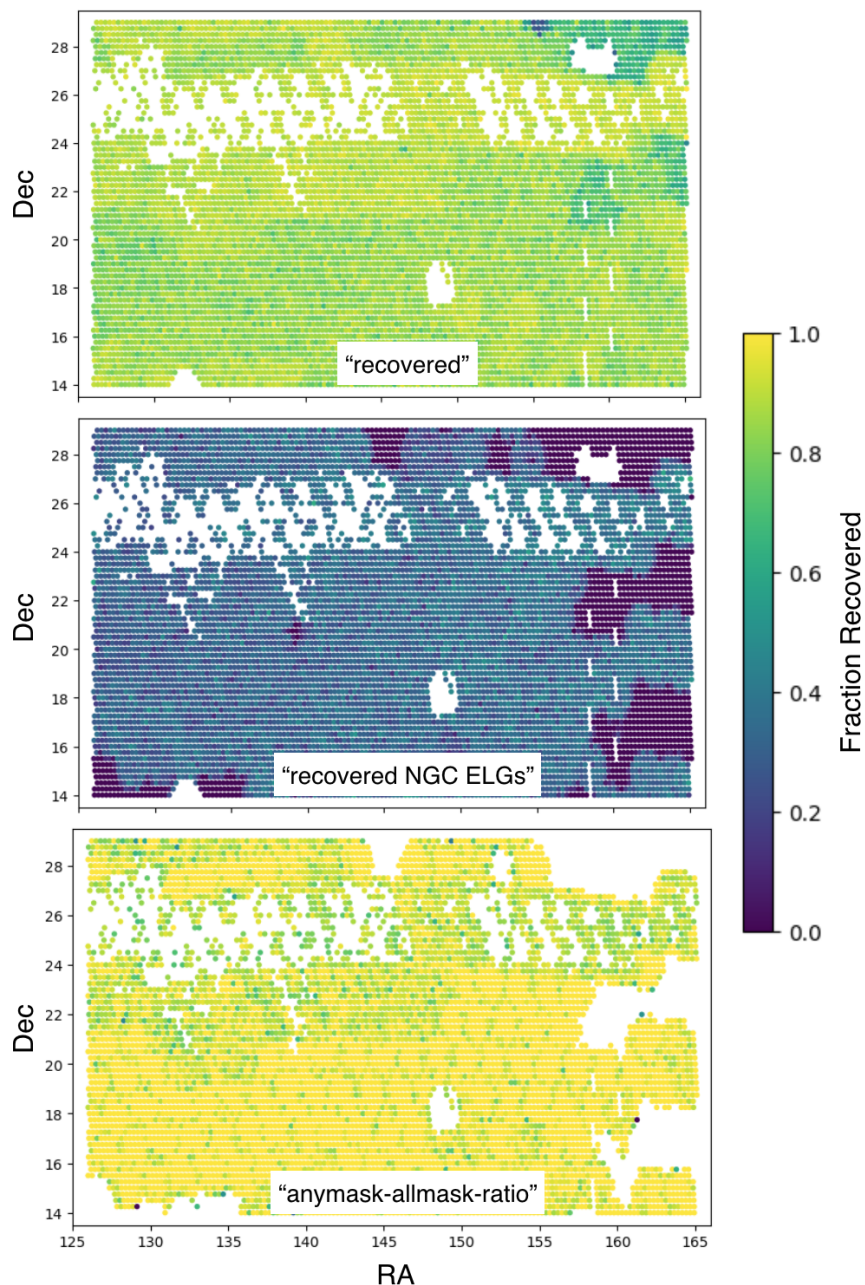
Figure 5.10: weight maps of imaging systematics that can be used by map–based methods for removing imaging systematics or to create mocks for estimating the variance of arbitrary ACF measurements. (Top) The fraction of all injected sources that `Legacypipe` detects and measures. (Middle) The fraction of true NGC eBOSS ELGs that `Legacypipe` detects and measures and that have `Tractor` measurements that pass NGC eBOSS ELG target selection. (Bottom) Using `Tractor` measurements, the ratio of the number of sources that pass NGC eBOSS ELG target selection using anymask grz = 0 to the number of when using allmask grz = 0.

Chapter 6

Conclusions

6.1   Thesis Conclusions

This research undertaken for this thesis has enhanced DESI's capability to achieve its science objectives by improving all facets of the Legacy Survey's program. These range from optimizing depth uniformity while taking observations, to running the `Legacypipe` pipeline that transforms images of the night sky into large–scale–structure catalogs, to implementing a novel method for understanding the inevitable biases and systematics in those catalogs.

A major challenge for past and future wide–field imaging surveys is the uneven depth that results from varying observing conditions that plague ground–based observatories. Chapter 2 presents the mapping and observing strategy for DECaLS and MzLS, both of which employ a unique strategy to dynamically adjust the exposure times as rapidly as possible (every 2–3 minutes) in response to the changing observing conditions. Chapter 3 explores the effect that dynamic exposure times (expose precisely long enough to reach depth) can have on other wide–field surveys, both ongoing and planned, such as PTF, iPTF, DES, ZTF and LSST. Compared to the nominal model of fixed exposure times, the benefits of dynamic exposure times are quite impressive.

Another major challenge for future galaxy surveys will be to understand the inevitable biases and systematics in their galaxy sample(s). For example, the Legacy Surveys will combine g, r, and z imaging from three telescopes to provide 30M galaxy targets for DESI. To make cosmological measurements, the clustering statistics of the observed distribution of galaxies must be compared to a random distribution of galaxies that incorporates all the signatures of systematic effects that impact the observed data. This would be easy if every galaxy could be detected, but a large number of instrumental effects can make the observed and actual distributions of galaxies very different. For example, two galaxies that appear near each other on the sky will often be detected as a single galaxy; the fainter galaxy often being lost. Similarly, bright stars make the detection of nearby faint galaxies challenging. Variations in observing conditions, especially for a multi–year survey, create unobserved or poorly sampled regions of the sky and consequently fewer galaxy detections. These biases and systematics, which come in at the few–percent level, must be accurately characterized at

a level an order of magnitude better for the next generation of galaxy redshift surveys, such as DESI, to measure cosmological parameters to sub–percent accuracy. However, describing which galaxies are and are not detected in the vicinity of a bright star requires knowing exactly how source detection and measurement take place, which is encoded in a piece of software with thousands of lines of code. For the Legacy Surveys this code is `Legacypipe`. Chapters 4 and 5 present our new method that allows us to characterize the above process. Our Monte Carlo method adds simulated sources, with properties closely matched to the galaxies of interest, to random locations in the astronomical images and then performs source detection and measurement, characterizing the complex selection inherent in large–scale–structure catalogs. The process is repeated until the injected source density is high enough to satisfy one's science objectives. For instance, the DESI target density for ELGs is 2400 deg^2, so simulated ELGs should be injected at more than 10 times this density. We used `Obiwan` to identify numerous biases and systematics in `Legacypipe`, namely, that it underestimates the uncertainty on g, r, and z flux by factors of 1.7–2, on r_{half} by a factor of 2.5–5, and the uncertainty on e1 and e2 by a factor of 2.7–3.5.

Although written to work with `Legacypipe`, `Obiwan` is open source and modular so that the astronomical community can use it as a general tool for analyzing multi–wavelength imaging data. There is increasing interest in the DESI collaboration for using `Obiwan` in the final DESI clustering analysis; and an increasing list of `Obiwan` users. See our ReadTheDocs page.[1]

As a newly named DESI builder, I look forward to staying involved with DESI no matter where my new adventures take me, as I transition from academia to industry.

---

[1] http://obiwan.readthedocs.io/en/latest

Bibliography

Abazajian, K. N., Adelman-McCarthy, J. K., Agüeros, M. A., et al. 2009, ApJS, 182, 543

Albrecht, A., Bernstein, G., Cahn, R., et al. 2006, ArXiv Astrophysics e-prints, astro-ph/0609591

Alpher, R. A., Bethe, H., & Gamow, G. 1948a, Physical Review, 73, 803

Alpher, R. A., & Herman, R. 1948a, Nature, 162, 774

Alpher, R. A., Herman, R., & Gamow, G. A. 1948b, Physical Review, 74, 1198

Alpher, R. A., & Herman, R. C. 1948b, Physical Review, 74, 1737

Anderson, L., Aubourg, E., Bailey, S., et al. 2012, MNRAS, 427, 3435

Anderson, L., Aubourg, É., Bailey, S., et al. 2014, MNRAS, 441, 24

Bassett, B., & Hlozek, R. 2010, Baryon acoustic oscillations, 246

Bennett, C. L., Halpern, M., Hinshaw, G., et al. 2003, The Astrophysical Journal Supplement Series, 148, 1

Bertin, E. 2011, in Astronomical Society of the Pacific Conference Series, Vol. 442, Astronomical Data Analysis Software and Systems XX, ed. I. N. Evans, A. Accomazzi, D. J. Mink, & A. H. Rots, 435

Beutler, F., Blake, C., Colless, M., et al. 2011, Monthly Notices of the Royal Astronomical Society, 416, 3017

Beutler, F., Saito, S., Seo, H.-J., et al. 2014, MNRAS, 443, 1065

Beutler, F., Seo, H.-J., Ross, A. J., et al. 2016, ArXiv e-prints, arXiv:1607.03149

Blake, C., Jurek, R. J., Brough, S., et al. 2009, MNRAS, 395, 240

Blake, C., Brough, S., Colless, M., et al. 2010, MNRAS, 406, 803

Blake, C., Kazin, E. A., Beutler, F., et al. 2011a, MNRAS, 418, 1707

Blake, C., Davis, T., Poole, G. B., et al. 2011b, MNRAS, 415, 2892

Bradley, L., Sipocz, B., Robitaille, T., et al. 2017, astropy/photutils: v0.4

Burleigh, K. J., Kong, H., Comparat, J., et al. 2018c in prep., AJ

Burleigh, K. J., Moustakas, J., & The DESI Collaboration. 2018b in prep., AJ

Burleigh, K. J., Dey, A., Lang, D., et al. 2018a in prep., AJ

—. in prep., AJ

Chambers, K. C., Magnier, E. A., Metcalfe, N., et al. 2016, ArXiv e-prints, arXiv:1612.05560 [astro-ph.IM]

Chevallier, M., & Polarski, D. 2001, International Journal of Modern Physics D, 10, 213

Colless, M., Dalton, G., Maddox, S., et al. 2001a, MNRAS, 328, 1039

—. 2001b, MNRAS, 328, 1039

Comparat, J., Jullo, E., Kneib, J.-P., et al. 2013, MNRAS, 433, 1146

Conroy, C., Wechsler, R. H., & Kravtsov, A. V. 2006, ApJ, 647, 201

Dawson, K. S., Schlegel, D. J., Ahn, C. P., et al. 2013, AJ, 145, 10

Dawson, K. S., Kneib, J.-P., Percival, W. J., et al. 2016, AJ, 151, 44

de Vaucouleurs, G. 1948, Annales d'Astrophysique, 11, 247

Delubac, T., Bautista, J. E., Busca, N. G., et al. 2015, A&A, 574, A59

Delubac, T., Raichoor, A., Comparat, J., et al. 2017, MNRAS, 465, 1831

DES Collaboration. 2017, ArXiv e-prints, arXiv:1708.01530

DESI Collaboration. 2016a, ArXiv e-prints, arXiv:1611.00036 [astro-ph.IM]

—. 2016b, ArXiv e-prints, arXiv:1611.00037 [astro-ph.IM]

Desjacques, V., Jeong, D., & Schmidt, F. 2016, ArXiv e-prints, arXiv:1611.09787

Dey, A., Rabinowitz, D., Karcher, A., et al. 2016a, in Proc. SPIE, Vol. 9908, Ground-based and Airborne Instrumentation for Astronomy VI, 99082C

Dey, A., Rabinowitz, D., Karcher, A., et al. 2016b, in Proc. SPIE, Vol. 9908, Ground-based and Airborne Instrumentation for Astronomy VI, 99082C

Dey, A., Schlegel, D. J., Lang, D., et al. 2018, ArXiv e-prints, arXiv:1804.08657

Dodelson, S. 2003, Modern cosmology (San Diego, CA: Academic Press)

Doroshkevich, A. G., Zel'dovich, Y. B., & Syunyaev, R. A. 1978, Soviet Ast., 22, 523

Drinkwater, M. J., Jurek, R. J., Blake, C., et al. 2010, MNRAS, 401, 1429

D'Souza, R., & Bell, E. F. 2018, MNRAS, 474, 5300

Eisenstein, D. J., & Bennett, C. L. 2008, Physics Today, 61, 44

Eisenstein, D. J., & Hu, W. 1998, ApJ, 496, 605

Eisenstein, D. J., Seo, H.-J., & White, M. 2007, ApJ, 664, 660

Eisenstein, D. J., Zehavi, I., Hogg, D. W., et al. 2005, ApJ, 633, 560

Elsner, F., Leistedt, B., & Peiris, H. V. 2016, MNRAS, 456, 2095

Elvin-Poole, J., Crocce, M., Ross, A. J., et al. 2017, ArXiv e-prints, arXiv:1708.01536

Falco, E. E., Kurtz, M. J., Geller, M. J., et al. 1999, PASP, 111, 438

Favole, G., Comparat, J., Prada, F., et al. 2016, MNRAS, 461, 3421

Fitzpatrick, E. L. 1999, PASP, 111, 63

Fixsen, D. J., Cheng, E. S., Gales, J. M., et al. 1996, ApJ, 473, 576

Flaugher, B., Diehl, H. T., Honscheid, K., et al. 2015, AJ, 150, 150

Gaia Collaboration, Brown, A. G. A., Vallenari, A., et al. 2016a, A&A, 595, A2

Gaia Collaboration, Prusti, T., de Bruijne, J. H. J., et al. 2016b, A&A, 595, A1

Geach, J. E., Smail, I., Best, P. N., et al. 2008, MNRAS, 388, 1473

Gil-Marín, H., Verde, L., Noreña, J., et al. 2015, MNRAS, 452, 1914

Górski, K. M., Hivon, E., Banday, A. J., et al. 2005, ApJ, 622, 759

Hamilton, A. J. S. 1993, ApJ, 417, 19

Ho, S., Cuesta, A., Seo, H.-J., et al. 2012, ApJ, 761, 14

Hu, W., & White, M. 1996, ApJ, 471, 30

Hubble, E. 1929, Proceedings of the National Academy of Science, 15, 168

Huchra, J. P., Vogeley, M. S., & Geller, M. J. 1999, ApJS, 121, 287

Ivezić, Ž., Kahn, S. M., Tyson, J. A., et al. 2008, ArXiv e-prints, arXiv:0805.2366

Jones, D. H., Saunders, W., Colless, M., et al. 2004, MNRAS, 355, 747

Kaiser, N. 1984, ApJ, 284, L9

Klypin, A., Prada, F., Yepes, G., Hess, S., & Gottlober, S. 2013, ArXiv e-prints, arXiv:1310.3740 [astro-ph.CO]

Klypin, A., Yepes, G., Gottlöber, S., Prada, F., & Heß, S. 2016, MNRAS, 457, 4340

Landy, S. D., & Szalay, A. S. 1993, ApJ, 412, 64

Lang, D., Dey, A., Schlegel, D. J., et al. in prep, AJ

Laurent, P., Eftekharzadeh, S., Le Goff, J.-M., et al. 2017, J. Cosmology Astropart. Phys., 7, 017

Law, N. M., Kulkarni, S. R., Dekany, R. G., et al. 2009, PASP, 121, 1395

Leistedt, B., Peiris, H. V., Mortlock, D. J., Benoit-Lévy, A., & Pontzen, A. 2013, MNRAS, 435, 1857

Limber, D. N. 1953, ApJ, 117, 134

Linder, E. V. 2003, Physical Review Letters, 90, 091301

Lucas, G. 1977, Star Wars. Episode IV, A New Hope (20th Century Fox, Lucasfilm Limited production)

Maddox, S. J., Efstathiou, G., & Sutherland, W. J. 1996, MNRAS, 283, 1227

Meiksin, A., White, M., & Peacock, J. A. 1999, MNRAS, 304, 851

Meisner, A. M., Lang, D., & Schlegel, D. J. 2017, AJ, 153, 38

Mo, H., van den Bosch, F. C., & White, S. 2010, Galaxy Formation and Evolution

Myers, A. D., Brunner, R. J., Richards, G. T., et al. 2006a, ApJ, 638, 622

—. 2006b, ApJ, 638, 622

Myers, A. D., Palanque-Delabrouille, N., Prakash, A., et al. 2015, ApJS, 221, 27

Newman, J. A., Cooper, M. C., Davis, M., et al. 2013, ApJS, 208, 5

Nidever, D. L., Zasowski, G., Majewski, S. R., et al. 2012, ApJ, 755, L25

Norberg, P., Baugh, C. M., Gaztañaga, E., & Croton, D. J. 2009, MNRAS, 396, 19

Nugent, P. E., & Burleigh, K. J. 2018 in prep., AJ

Padmanabhan, N., Xu, X., Eisenstein, D. J., et al. 2012, MNRAS, 427, 2132

Palanque-Delabrouille, N., Yeche, C., Myers, A. D., et al. 2011, A&A, 530, A122

Partridge, R. B. 2007, 3K: The Cosmic Microwave Background Radiation

Peebles, P. J. E. 1980, The large-scale structure of the universe

Peebles, P. J. E., & Yu, J. T. 1970, ApJ, 162, 815

Penzias, A. A., & Wilson, R. W. 1965, ApJ, 142, 419

Percival, W. J., Cole, S., Eisenstein, D. J., et al. 2007, MNRAS, 381, 1053

Percival, W. J., Reid, B. A., Eisenstein, D. J., et al. 2010, MNRAS, 401, 2148

Pilachowski, C., Badenes, C., Bailey, S., et al. 2012, ArXiv e-prints, arXiv:1211.0285 [astro-ph.CO]

Planck Collaboration. 2016, A&A, 594, A13

Prakash, A., Licquia, T. C., Newman, J. A., et al. 2016, ApJS, 224, 34

Raichoor, A., Comparat, J., Delubac, T., et al. 2017, MNRAS, 471, 3955

Rose, C., & Smith, M. D. 2002, in Compstat, ed. W. Härdle & B. Rönz (Heidelberg: Physica-

Verlag HD), 437

Ross, A. J., Ho, S., Cuesta, A. J., et al. 2011, MNRAS, 417, 1350

Ross, A. J., Percival, W. J., Sánchez, A. G., et al. 2012, MNRAS, 424, 564

Ross, A. J., Beutler, F., Chuang, C.-H., et al. 2017, MNRAS, 464, 1168

Rowe, B. T. P., Jarvis, M., Mandelbaum, R., et al. 2015, Astronomy and Computing, 10, 121

Rybicki, G. B., & Press, W. H. 1992, ApJ, 398, 169

Sawangwit, U., Shanks, T., Abdalla, F. B., et al. 2011, MNRAS, 416, 3033

Schlafly, E. F., & Finkbeiner, D. P. 2011, ApJ, 737, 103

Schlegel, D. J., Finkbeiner, D. P., & Davis, M. 1998, ApJ, 500, 525

Scoville, N., Abraham, R. G., Aussel, H., et al. 2007, The Astrophysical Journal Supplement Series, 172, 38

Sersic, J. L. 1968, Atlas de Galaxias Australes

Sherwin, B. D., & Zaldarriaga, M. 2012, Phys. Rev. D, 85, 103523

Silk, J. 1968, ApJ, 151, 459

Skrutskie, M. F., Cutri, R. M., Stiening, R., et al. 2006, AJ, 131, 1163

Slepian, Z., & Eisenstein, D. J. 2015, MNRAS, 454, 4142

Slosar, A., Seljak, U., & Makarov, A. 2004, Phys. Rev. D, 69, 123003

Smoot, G. F., Bennett, C. L., Kogut, A., et al. 1992, ApJ, 396, L1

Suchyta, E., Huff, E. M., Aleksić, J., et al. 2016, MNRAS, 457, 786

Sumiyoshi, M., Totani, T., Oshige, S., et al. 2009, ArXiv e-prints, arXiv:0902.2064

Sunyaev, R. A., & Zeldovich, Y. B. 1970, Ap&SS, 7, 3

Tegmark, M., Hamilton, A. J. S., Strauss, M. A., Vogeley, M. S., & Szalay, A. S. 1998, ApJ, 499, 555

Tegmark, M., Eisenstein, D. J., Strauss, M. A., et al. 2006, Phys. Rev. D, 74, 123507

The Dark Energy Survey Collaboration. 2005, ArXiv Astrophysics e-prints, astro-ph/0510346

Valdes, F., Gruendl, R., & DES Project. 2014, in Astronomical Society of the Pacific Conference Series, Vol. 485, Astronomical Data Analysis Software and Systems XXIII, ed. N. Manset & P. Forshay, 379

Weinberg, D. H., Mortonson, M. J., Eisenstein, D. J., et al. 2013, Phys. Rep., 530, 87

Wright, E. L., Eisenhardt, P. R. M., Mainzer, A. K., et al. 2010, AJ, 140, 1868

York, D. G., Adelman, J., Anderson, Jr., J. E., et al. 2000, AJ, 120, 1579

Zou, H., Zhou, X., Fan, X., et al. 2017, PASP, 129, 064101

Appendix A

Observing Strategy for the Legacy Surveys

A.1   Color Transformations from PS1 to DECam/MOSAIC3

The g–band PS1 to DECam color correction is

$$g_{\text{decam}} = g_{\text{ps1}} + A_0 + A_1 \left(g_{\text{ps1}} - r_{\text{ps1}}\right) + A_2 \left(g_{\text{ps1}} - r_{\text{ps1}}\right)^2 +$$
$$+ A_3 \left(g_{\text{ps1}} - r_{\text{ps1}}\right)^3, \tag{A.1}$$

where the functional form is identical for r and z–band, and the A_i coefficients are given in Table A.1 for DECam and MOSAIC3.

A.2   Useful numbers

The read noise and coefficients for atmospheric extinction and galactic extinction are listed in Table A.2, for each camera and band. These are useful to document but are not needed in the main text.

Table A.1: Color Transformations from PS1 to DECam/MOSAIC3

Camera	Filter	D_0	D_1	D_2	D_3
DECam	g	0.0	0.04709	0.00084	−0.00340
DECam	r	0.0	−0.09939	0.04509	−0.01488
DECam	z	0.0	−0.13404	0.06591	−0.01695
MOSAIC3	z	0.0	−0.12132	0.04608	−0.01164

Table A.2: Useful numbers

Statistic	Symbol	Units	DECam			MOSAIC3
			g	r	z	z
Read Noise	R_{out}	e-/pixel	7.0	7.0	7.0	5.9
Atmospheric Extinction	K	–	0.17	0.10	0.06	0.06
Galactic Extinction	A	–	3.214	2.165	1.592	1.592

Note. — The values for A are according to the Fitzpatrick (1999) extinction curve and the analysis of Schlafly & Finkbeiner (2011).

Appendix B

`Obiwan`, A New Hope: Characterizing Astronomical Imaging Systematics with Forward Modeling and Monte Carlo Simulations of Galaxies

B.1   Software

`Obiwan` is written in Python 3.6 and is compatible with Python 2.7. See our ReadThe-Docs page http://obiwan.readthedocs.io/en/latest for how to use the `Obiwan` API, install its dependencies, and run it at NERSC.

B.1.1   Travis Continuous Integration (CI)

Fig. 4.1 is one of our Travis CI regression tests, which uses `Obiwan` to inject four stars and/or galaxies into a 200x200 pixel DECaLS image in g, r, and z–band, respectively. A quantitative test ensures that `Tractor` measures the flux and shape parameters of the sources accurately, while a qualitative test checks that the expected number of output files are written and they contain the appropriate metadata.

B.1.2   Scaling Tests

We performed the following scaling tests on Edison compute nodes using Python3.6. To estimate the variance in runtime, we repeated each run on 10 randomly chosen bricks from DR5. All compute jobs were launched as independent MPI tasks, one task per brick.

To determine the optimum number of simulated sources to inject per Monte Carlo itera-tion, we measured the run time of each `Legacypipe` stage (see Section 4.3.2), after injecting sources. We performed three sets of runs by injecting 1500 sources all at once, 1000 sources then 500 sources, and 500 sources three times. Fig. B.1 plots the wall times to inject the

1500 sources, averaged over the 10 bricks. Error bars show the standard deviations. Model fitting (the `fitblobs` stage) takes 10x longer than any other stage and is the bottleneck. The overhead of repeating stages (e.g., three times each for the runs with 500 sources) is negligible, which means that injecting a large number of sources does not increase the total wall time. In practice, injecting too many sources (more than 1500 per brick) creates large blobs (see Section 4.3.2), which reduces `Tractor`'s ability to parallelize and often causes it to run out of memory. The optimum number of sources to inject per brick is 1000–1500.
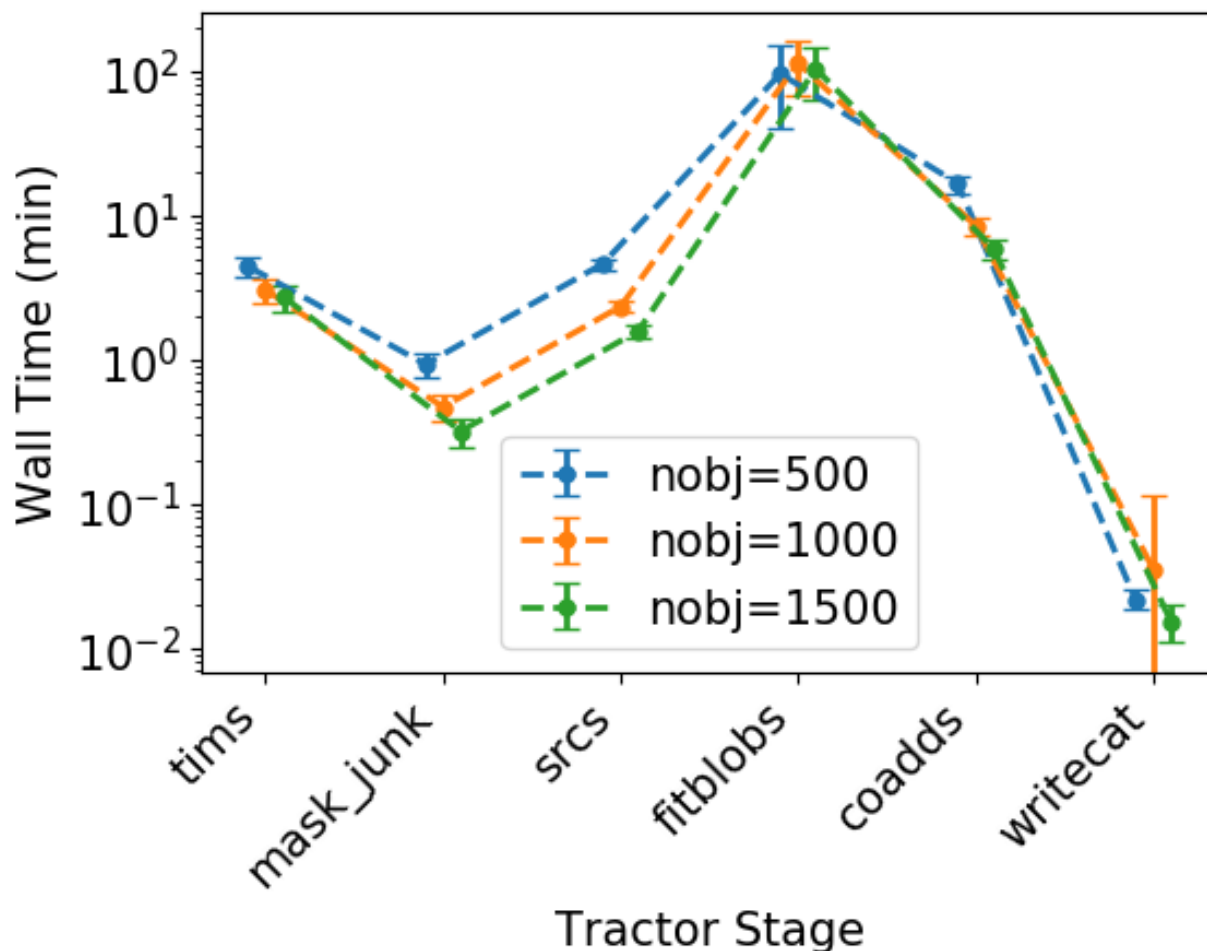
Figure B.1: Scaling test for the optimal number of simulated sources to inject (nobj) per brick. Plotted is the wall time to inject 1500 sources, averaged over 10 bricks, versus `Legacypipe` stage. The different lines correspond to the three sets of runs: injecting 1500 sources all at once (green), 1000 sources then 500 sources (orange), and 500 sources three times (blue).

Next, we determine the optimal number of cores per node when running `Obiwan`. We performed a strong scaling test by injecting 1000 sources per brick using three, four, and

six cores per node, respectively. Fig. B.2 plots the CPU time (wall time multiplied by the number of cores), averaged over the 10 bricks, versus the `Legacypipe` stage. Error bars show the standard deviations. The optimum number of of course per node is three, with six cores being a close second.
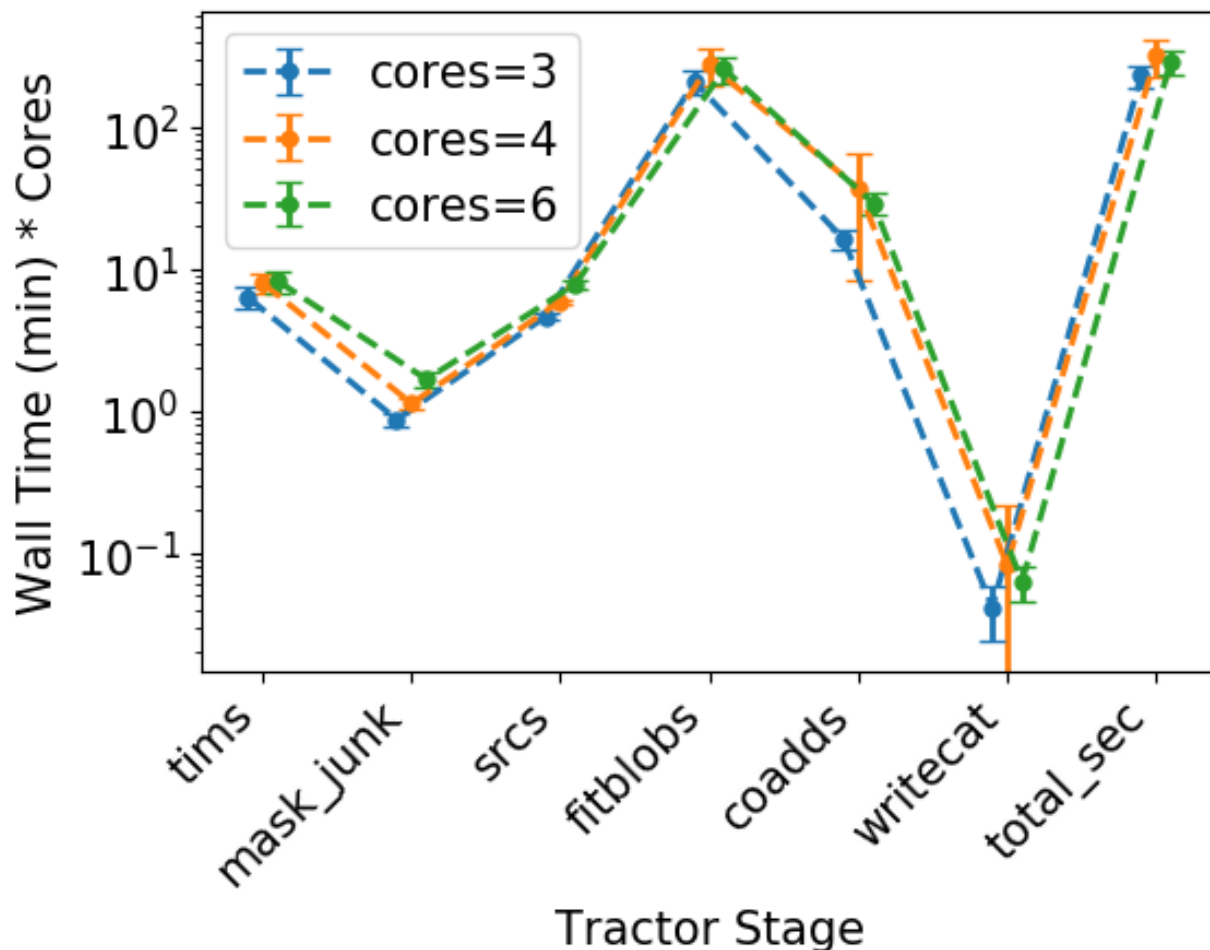

Figure B.2: Strong scaling test for the optimal number of cores per node. Plotted is CPU time versus `Legacypipe` stage. The different lines correspond to using three, four, and six cores per node.

B.1.3 High–Performance Computing at NERSC

`Obiwan` and `Legacypipe` scale on up to 100 compute nodes when installed on I/O optimized file systems, such as on the SCRATCH or global common filesystems at NERSC. A Docker image is needed to perform well on hundreds of nodes or more.

B.2   Data Products

All data products are available at The National Energy Research Scientific Computing Center (NERSC), on Cori SCRATCH: `/global/cscratch1/sd/kaylanb/obiwan_out/cosmos`

Appendix C

Removing Imaging Systematics from the eBOSS ELG Sample with `Obiwan`

C.1 Biases and Systematics (`Legacypipe`)

This section describes the biases and systematics that we find in `Legacypipe` after running `Obiwan` on eBOSS data. Fig. C.1 shows that `Tractor` is biased towards EXP sources. About 95% of true exponential sources are modeled as exponential, while 20% of true de Vaucouleurs sources are modeled as de Vaucouleurs. The other 80% of truly de Vaucouleurs sources are classified as SIMP (50%), EXP (20%), and PSF (10%). The EXP bias is surprisingly because `Tractor` model selection penalizes EXP and DEV sources equally (see Chapter 4). Fig. C.2 (top and middle) shows the distributions of true r_{half} for sources classified as PSF, SIMP, EXP, and DEV by `Tractor`. The most common size is $r_{\mathrm{half}} \sim 0.5''$; this is also most common recovered source size, even among non-SIMP sources. Source size most likely does not cause the EXP bias because the r_{half} distributions for EXP and DEV sources are very similar. Fig. C.2 (bottom) shows the fraction of all sources recovered by `Legacypipe` versus true r_{half}. There is a characteristic size ($r_{\mathrm{half}} \sim 1.5''$) after which the fraction recovered drops to, and fluctuates about, 50%.

Just as we did in chapter 4, we test the accuracy of `Tractor`'s parameter estimates by comparing the `Tractor` measured values for g, r, z flux, r_{half}, and ellipticity e1 and e2, to the true parameters of the sources we inject. Fig. C.3 shows the number of standard deviations (N_σ) away from truth of the `Tractor` measured g, r, and z–band flux, r_{half}, and ellipticity e1 and e2. As before, we get a crude estimate for how much `Tractor` underestimates the true variance by assuming that N_σ is Gaussian distributed and comparing the sample standard deviation (σ_s) to unity. If `Tractor`'s estimate of the true variance is unbiased, then $\sigma_s \sim 1$. Using the σ_s values, we conclude that `Tractor`'s measurement errors are underestimated by factors of ~ 1.8–2x for g, r, z flux, ~ 3.5–4.25x for r_{half}, and ~ 2.8–3.1x for ellipticity e1 and e2.

Fig. C.3 reveals very large systematics offset in flux (~ 0.25 mag in all bands) and r_{half} ($\sim$3–4$''$ for EXP and DEV sources), which we remove by subtracting the mean. `Tractor`
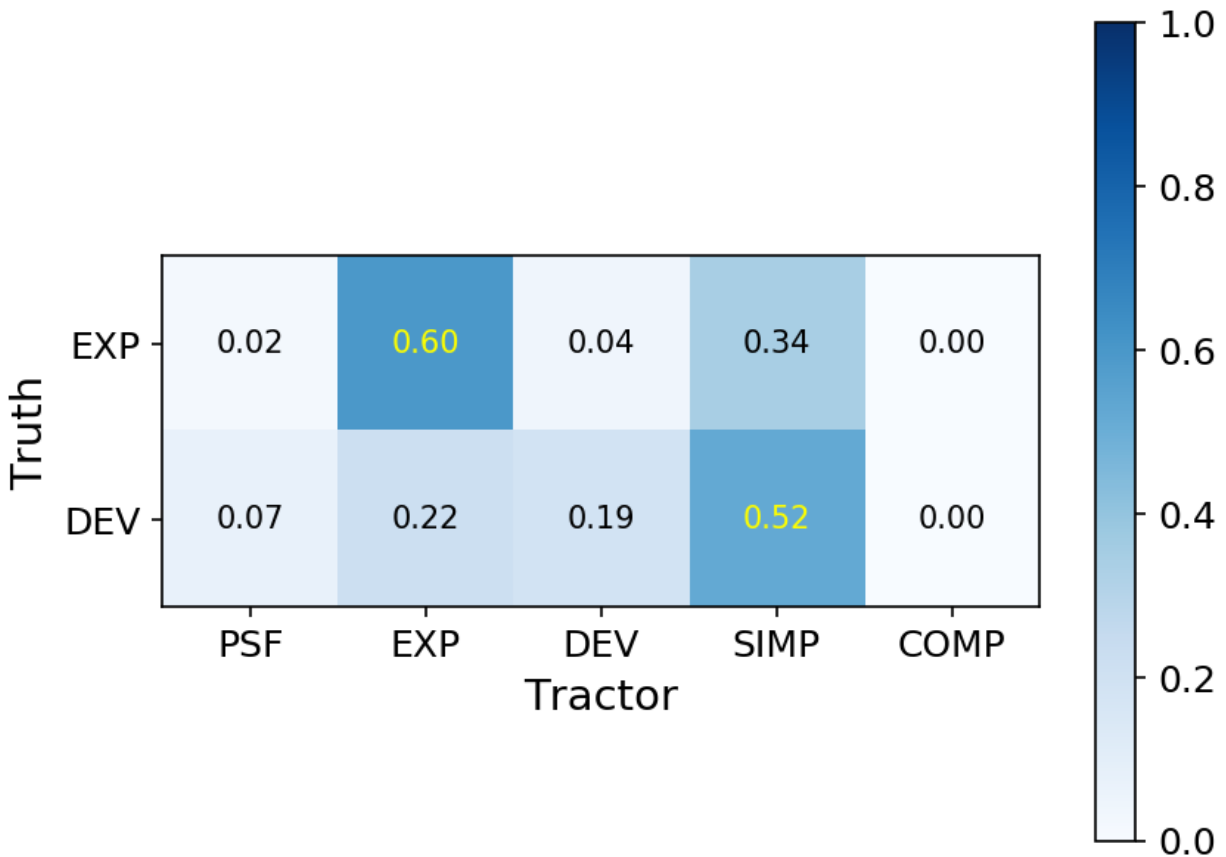
Figure C.1: Confusion matrix showing the fraction of true exponential or de Vaucouleurs sources that `Tractor` models as type PSF, SIMP, EXP, DEV, or COMP. `Tractor` is biased towards EXP sources. `Tractor` is biased towards EXP sources because 95% of true exponential sources are modeled as exponential, while 20% of true de Vaucouleurs sources are modeled as de Vaucouleurs.

fluxes are too faint while `Tractor` r_{half} is too large. There is no systematic offset for the ellipticity e1 and e2 measurements. Reasons for these offsets are discussed in Section C.1.2.

Because the measurement uncertainty can dependent on g, r, z magnitude, we make 2–dimensional histograms of N_σ for g, r, z flux versus g, r, z magnitude, respectively (Fig. C.4, left panel); and magnitude residual versus versus g, r, z magnitude (Fig. C.4, right panel). The results are nearly identical when only considering PSF, SIMP, EXP, or DEV sources.

We say `Legacypipe` recovers a injected source when there is exactly one `Tractor` catalog source within $1''$ of an injected source, and no DR3 `Tractor` catalog sources within $1''$ of the injected source. `Obiwan` injects sources at the nearest pixel center. This should lead to an RA and Dec offset, between the true centroid and `Tractor`'s measurement, equal to the

DECaLS pixel scale of $0.262''$ / pixel. The actual offset is $\sim 0.4''$ (see Fig.C.5), which is larger than expected but still small enough that our $1''$ matching radius is fine. The larger offset is most likely due to co–registry and `Tractor`'s simultaneous fitting of multiple images.

C.1.1 Edge-Sources

Fig. C.6 (bottom right panel) reproduces Fig. C.3 (left column), showing the number of standard deviations between true flux and `Tractor` measurement. The other panels in Fig. C.6 illustrate the data cleaning required to go from raw `Obiwan` outputs (top left panel) to the cleaned `Obiwan` outputs (bottom right panel). The top left panel shows that there are many sources with $N_\sigma \approx 0$ and that there is an offset of a few standard deviations. The offset is discussed in Section C.1.2. The sources with $N_\sigma \approx 0$ are sources that lie on top of CCD edges(s). They are linearly separable by `fracin` < 0.2 (top right panel), which is the fraction of each source that overlaps its CCD(s). The bottom left panel shows the $N_\sigma \approx 0$ distribution for `fracin` < 0.2 sources. The z–band measurements are particularly accurate. The bottom right panel shows the N_σ distribution after removing `fracin` < 0.2 sources and subtracting the mean. Note, the Legacy Surveys website[1] says that `fracin` is "near unity for real sources". This statement is incorrect: it is near unity for non-edge sources.

Why are `Tractor`'s measurements very accurate (e.g., $N_\sigma \approx 0$) for `fracin` < 0.2 sources? To test this we injected tens of galaxies onto the edges of three overlapping g, r, z CCDs, and found that if the source is detected `Tractor` can accurately reconstruct the full source profile even when less than 20% of the profile is actually in the image. The background sky level is effectively zero because so much of the source falls off the CCD, so the variance of the flux measurement is much smaller than for a non-edge source. In principle, we should include the edge–sources in our analysis, but we drop them because we are interested in `Legacypipe` biases and systematics for the average source, not the relatively small sample of edge–sources. Fig. C.7 shows that sources with `fracin` < 0.2 and `fracin` ≥ 0.2 have similar g, r, z magnitude, r_{half}, and redshift distributions, so we do not bias our analysis by removing the edge–sources. Fig. C.7 (bottom right panel) shows that $\sim 11\%$ of truly exponential and de Vaucouleurs galaxies, respectively, are removed by the `fracin` < 0.2 cut.

C.1.2 The 0.25 mag offset

Figs. C.3 and C.4 show that there is a very large (0.25 mag) offset between true flux and `Tractor` measurement, for all g, r, and z bands, and that this offset does not strongly depend on source magnitude or its Sérsic index. The offset is most likely explained by either imperfect sky subtraction or too small a stamp size for simulated sources. Potential problems with these explanations are that the latter should give a strong dependence on Sérsic index, while the former should produce a larger offset in g–band due to the brighter sky.

Imperfect sky subtraction. `Legacypipe` models and subtracts the background sky with a cubic–spline fit to the entire CCD. The spline model was assumed to be insensitive to bright

---

[1] http://legacysurvey.org/dr6/files

sources, however, after producing DR5 we realized that the sky model was tracing bright extended galaxies. An improved sky model was used for DR6,[2] but we are stuck with the pre–DR6 model because we are simulating DR3–era `Tractor` catalogs, so a 0.25 mag offset is conceivable.

Too small a stamp size for simulated sources. `Obiwan` draws each simulated source at the center of a 64×64 pixel postage stamp. The largest simulated sources have $r_{\mathrm{half}} = 2''$ (see Fig. C.2), and we assumed (incorrectly) that 64 pixels ($16''$ with DECam) was large enough to enclose $> 99.9\%$ of the flux for any source. Fig. C.8 shows how the fraction of enclosed flux depends on Sérsic index. For $n = 1$, 99% of the flux occurs at $2\,r_{\mathrm{half}}$ and 99.9% at $5\,r_{\mathrm{half}}$. For $n = 4$, 99% of the flux occurs at $6\,r_{\mathrm{half}}$ and 99.9% at $> 10\,r_{\mathrm{half}}$. The largest $n = 4$ sources have $10\,r_{\mathrm{half}} = 20''$, which makes our 64×64 pixel ($16x16''$) postage stamp too small. However, more than this must be going on because the same ~ 0.25 mag offset is seen when only $r_{\mathrm{half}} = 0.5''$ sources are injected (see Fig. 4.9).

C.2 Injecting Realistic eBOSS ELGs

C.2.1 ELG Targets

We construct our sample of ELG–like eBOSS galaxies (the eBOSS sample) using the eBOSS–`Tractor` tables, described in Section 5.3.3, as follows. We assume that all sources that `Tractor` classifies as type PSF are compact and/or unresolved galaxies. These sources should be reasonably well described by a pixelized PSF profile convolved with an exponential profile having $r_{\mathrm{half}} = \mathrm{avg}(\mathrm{FWHM})/2$, where the average is over all bands, so we reclassify them as such. We also reclassify SIMP sources as EXP and drop COMP sources because they comprise less than 1% of the sample.

DEV galaxies are systematically larger and about 1 mag brighter than EXP in all bands (see Fig. C.9), so we split the above sample into separate DEV and EXP samples. This yields 77,525 EXP and 7,439 DEV galaxies. We refer to this as our eBOSS sample. The full list of cuts we apply is:

- !NGC

- `z_flag == 1`

- $0 \leq \mathrm{redshift} \leq 2$

- `brick_primary`

- type $\neq$ COMP

- $r_{\mathrm{half}} > 0.131''$ (Nyquist limit, one half of the DECam pixel scale)

- (EXP) $r_{\mathrm{half}} < 2.5''$

---

[2] http://legacysurvey.org/dr6/description/

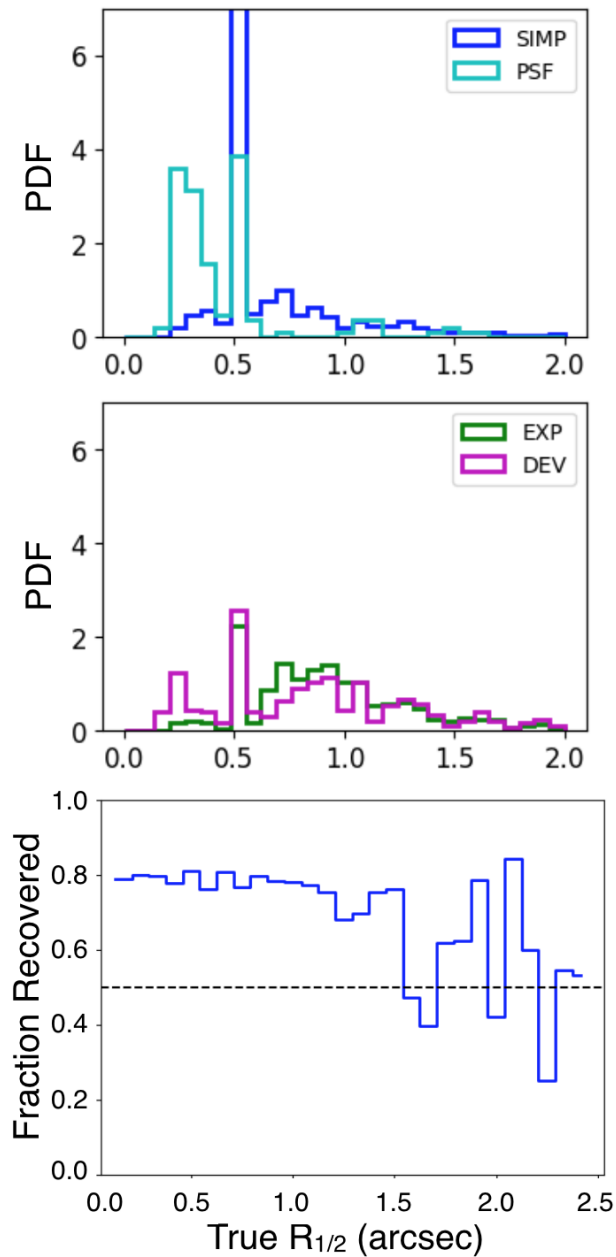- (DEV) $r_{\text{half}} < 5.0''$

Figure C.2: (Top) Injected r_{half} distributions for sources classified as EXP and DEV by `Tractor`. (Middle) Same but sources classified as PSF and SIMP. (Bottom) Fraction of all sources recovered by `Legacypipe` versus injected r_{half}.
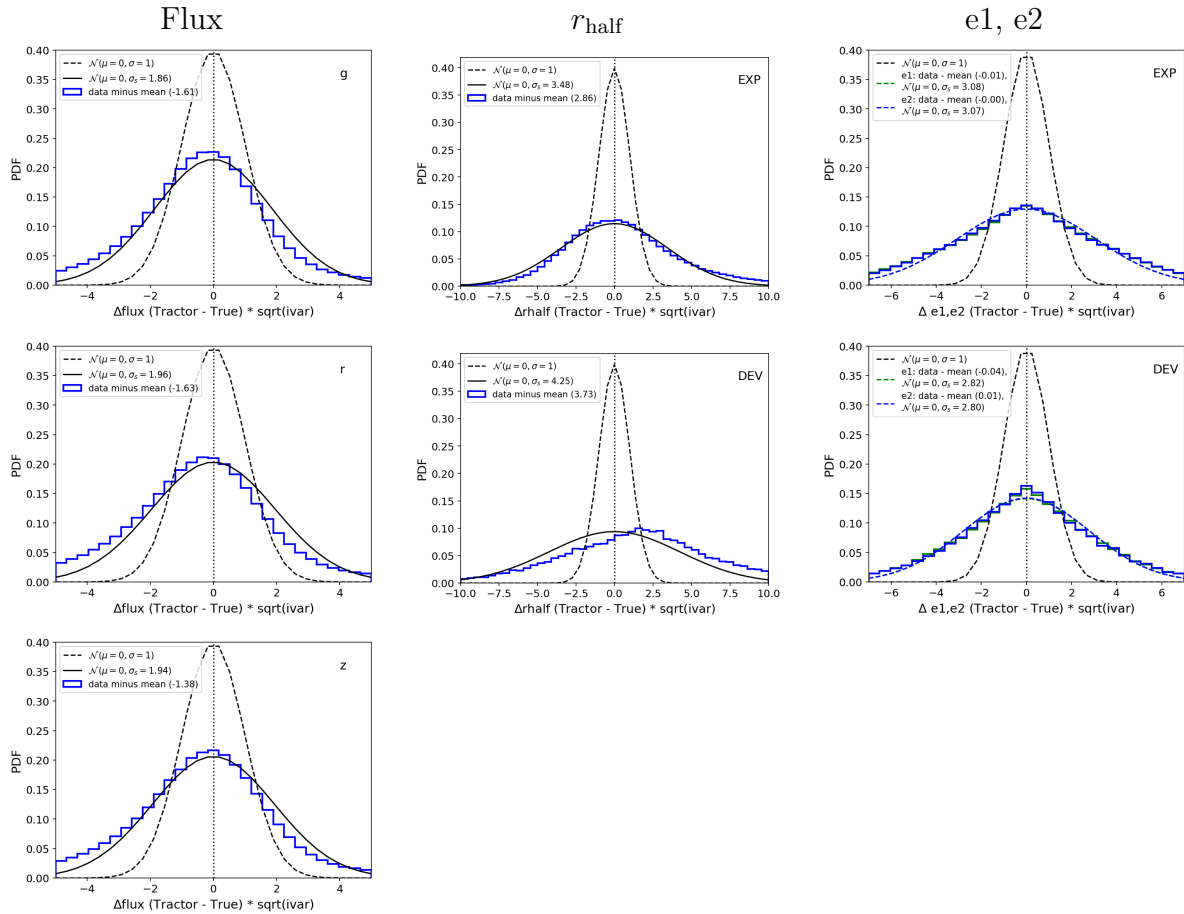
Figure C.3: Number of standard deviations away from truth (N_σ) of the `Tractor` measured flux, r_{half}, and ellipticity. The mean of each distribution has been subtracted. To get a crude estimate for how much `Tractor` underestimates the true variance, we assume that N_σ is Gaussian distributed and compare the sample standard deviation (σ_s) to unity. (Left) N_σ for g, r, z flux. (Middle) N_σ for r_{half} for sources `Tractor` classifies as EXP and DEV. (Right) N_σ for ellipticity e1 and e2 for sources `Tractor` classifies as EXP and DEV.
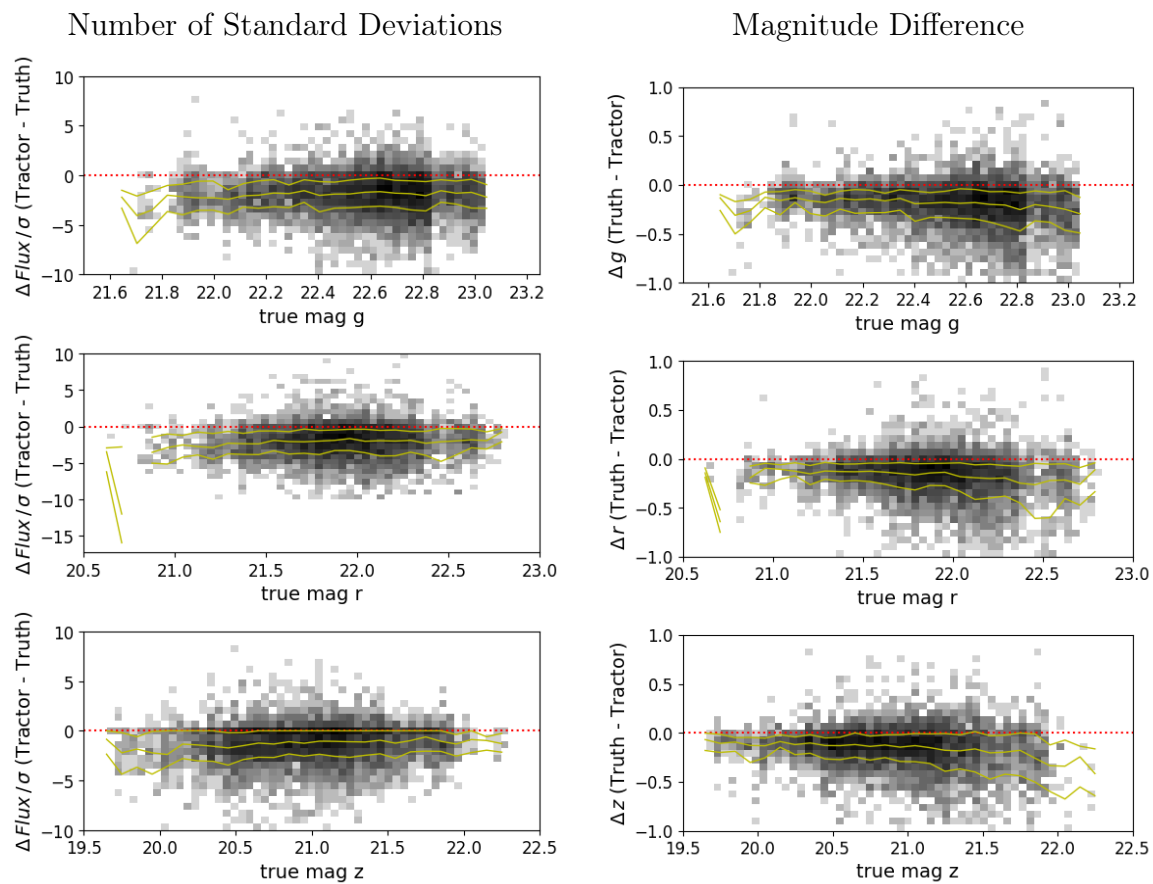
Figure C.4: 2–dimensional histograms of truth–`Tractor` residuals. (Left) N_σ for g, r, z flux versus g, r, z magnitude, respectively. Yellow lines are the 25th, 50th, 75th percentiles. (Right) Magnitude residuals versus g, r, z magnitude.
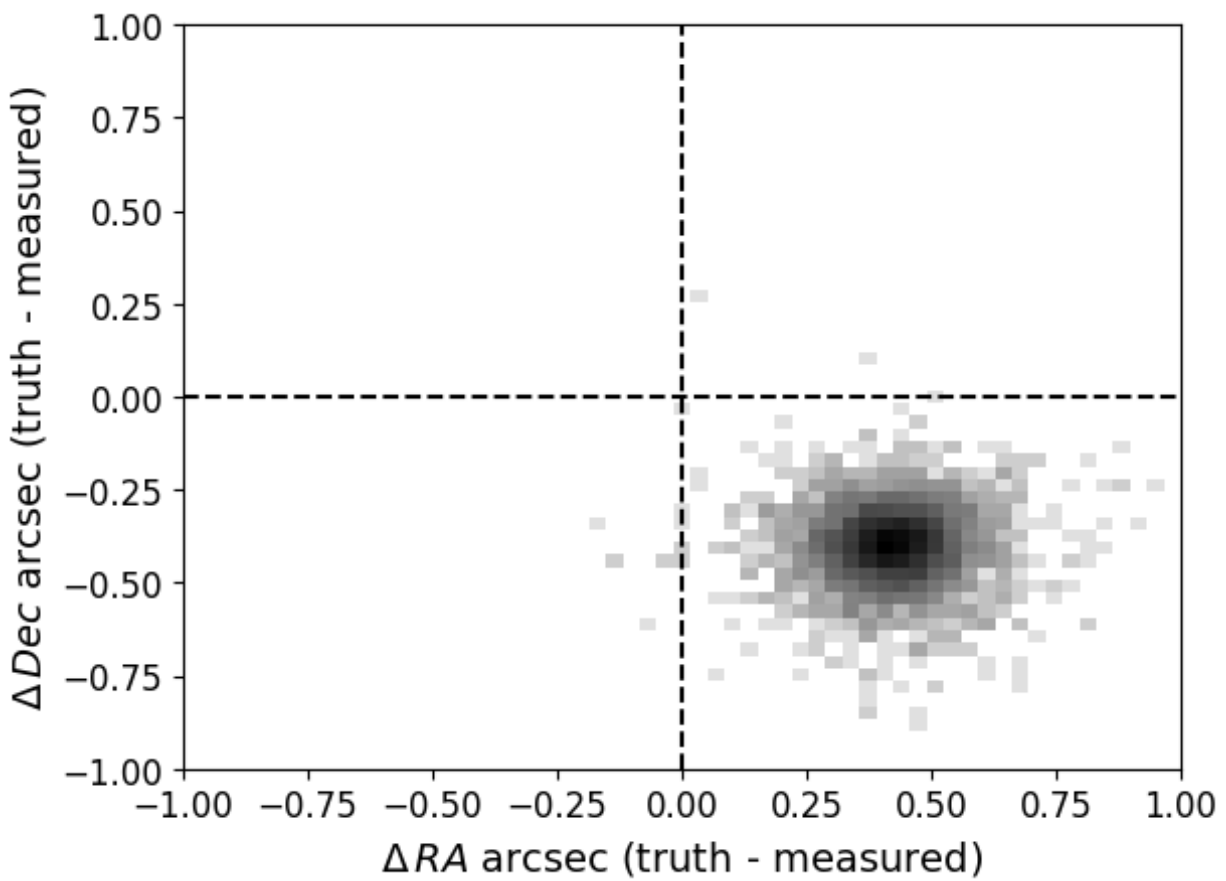
Figure C.5: 2–dimensional histogram of RA and Dec residuals between the true centroid and `Tractor`'s measurement of it. There is a systematic offset of 0.4″ because `Obiwan` injects sources at the nearest pixel center.
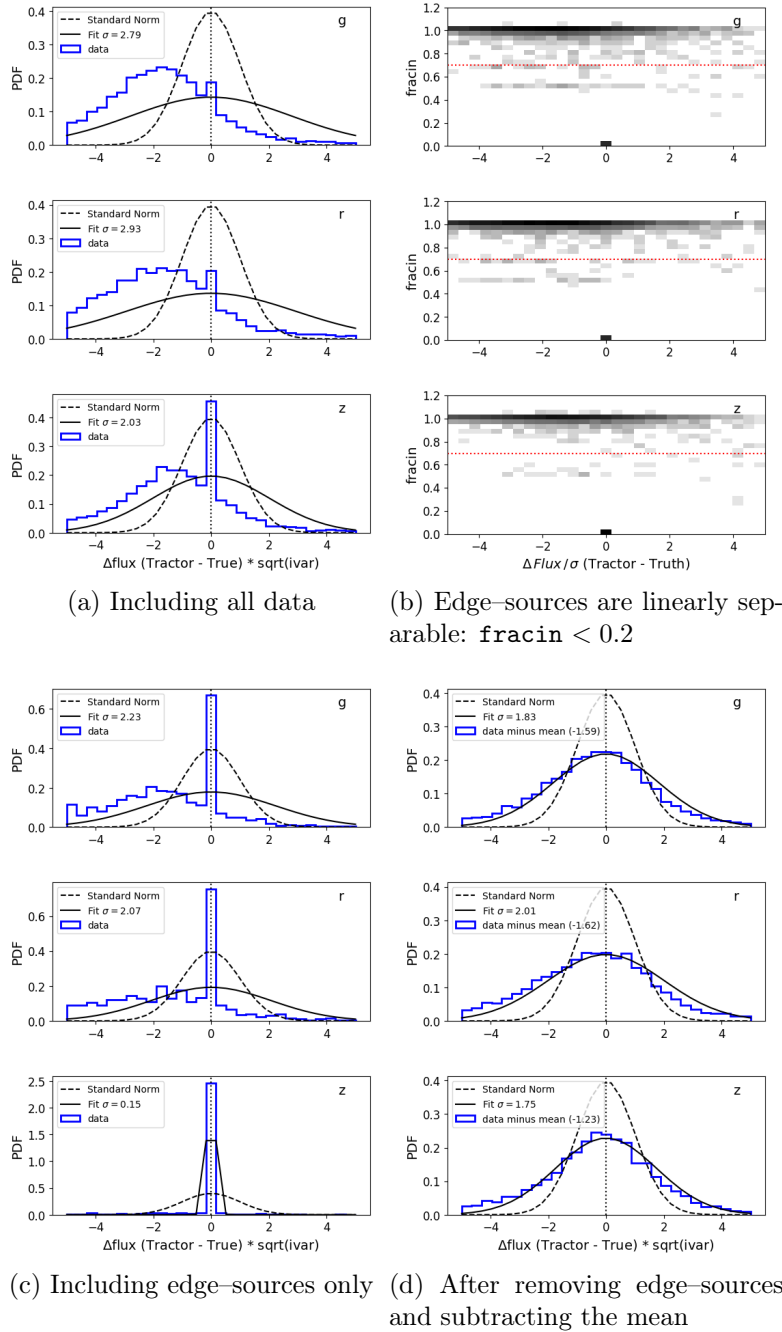
(a) Including all data

(b) Edge–sources are linearly separable: `fracin` < 0.2

(c) Including edge–sources only

(d) After removing edge–sources and subtracting the mean

Figure C.6: Illustration of the data cleaning required to go from raw to cleaned `Obiwan` outputs. (Top Left) The number of standard deviations (N_σ) between true flux and `Tractor` measurement. "ivar" is the inverse variance that `Tractor` estimates for each of its parameters. There is an offset of a few N_σ which corresponds to ~ 0.25 mag (see Section C.1.2) and many sources have $N_\sigma \approx 0$ (these are edge-sources). (Top Right) The edge-sources are linearly separated by `fracin` < 0.2, which is the fraction of each source that overlaps its CCD(s). (Bottom Left) The N_σ distribution for sources with `fracin` < 0.2. (Bottom Right) The N_σ distribution after removing `fracin` < 0.2 sources and subtracting the mean. This reproduces Fig. C.3.
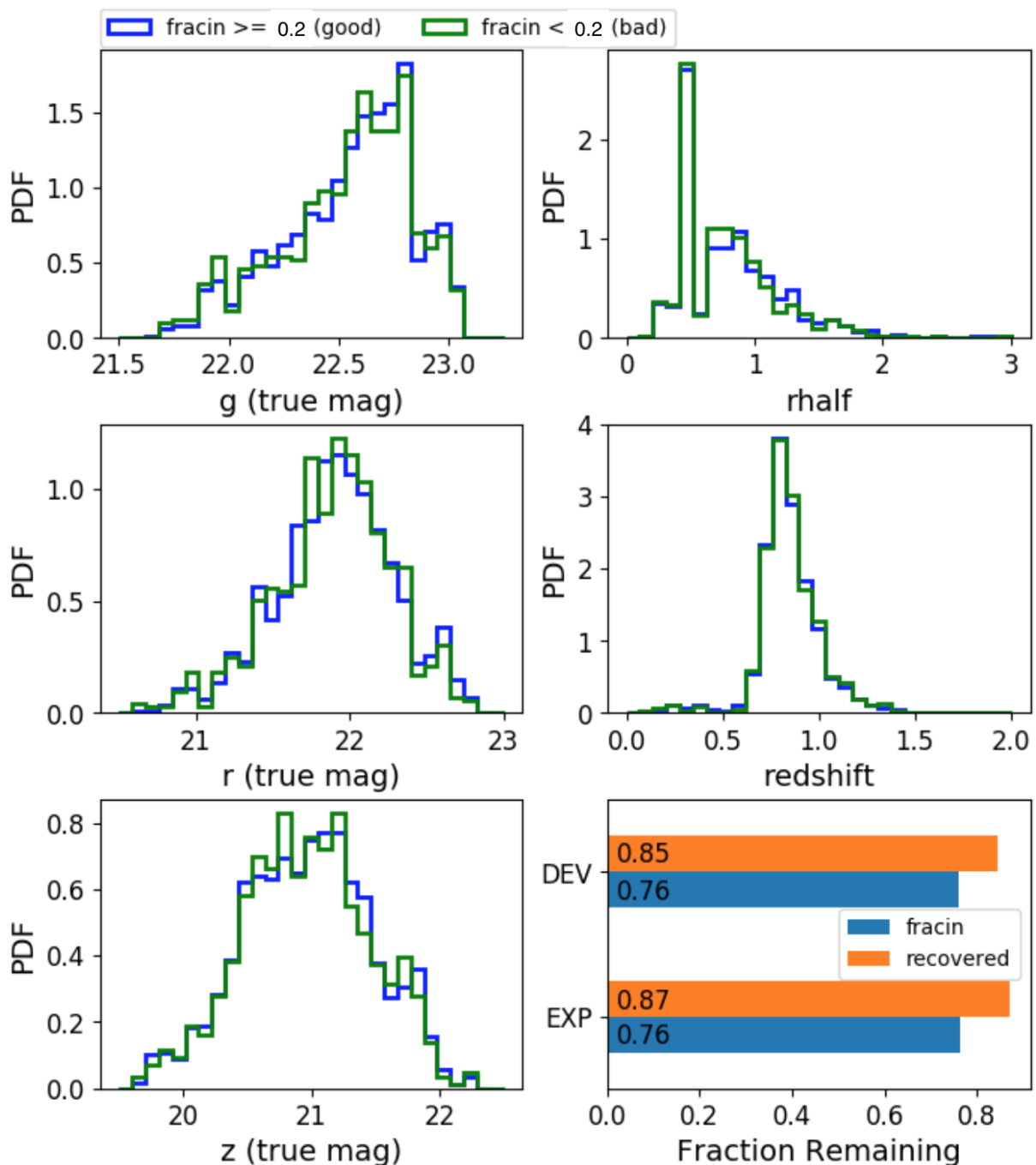
Figure C.7: (Histograms) g, r, z magnitude, r_{half}, and redshift PDFs for sources with `fracin` < 0.2 (blue) and `fracin` ≥ 0.2 (green). (Bottom Right) Fraction of injected exponential and de Vaucouleurs galaxies that are recovered by `Legacypipe` (orange) or remain after `Legacypipe` recovery and the cut on `fracin` < 0.2 (blue). About $\sim 11\%$ of truly exponential and de Vaucouleurs galaxies, respectively, are removed by the `fracin` < 0.2 cut.
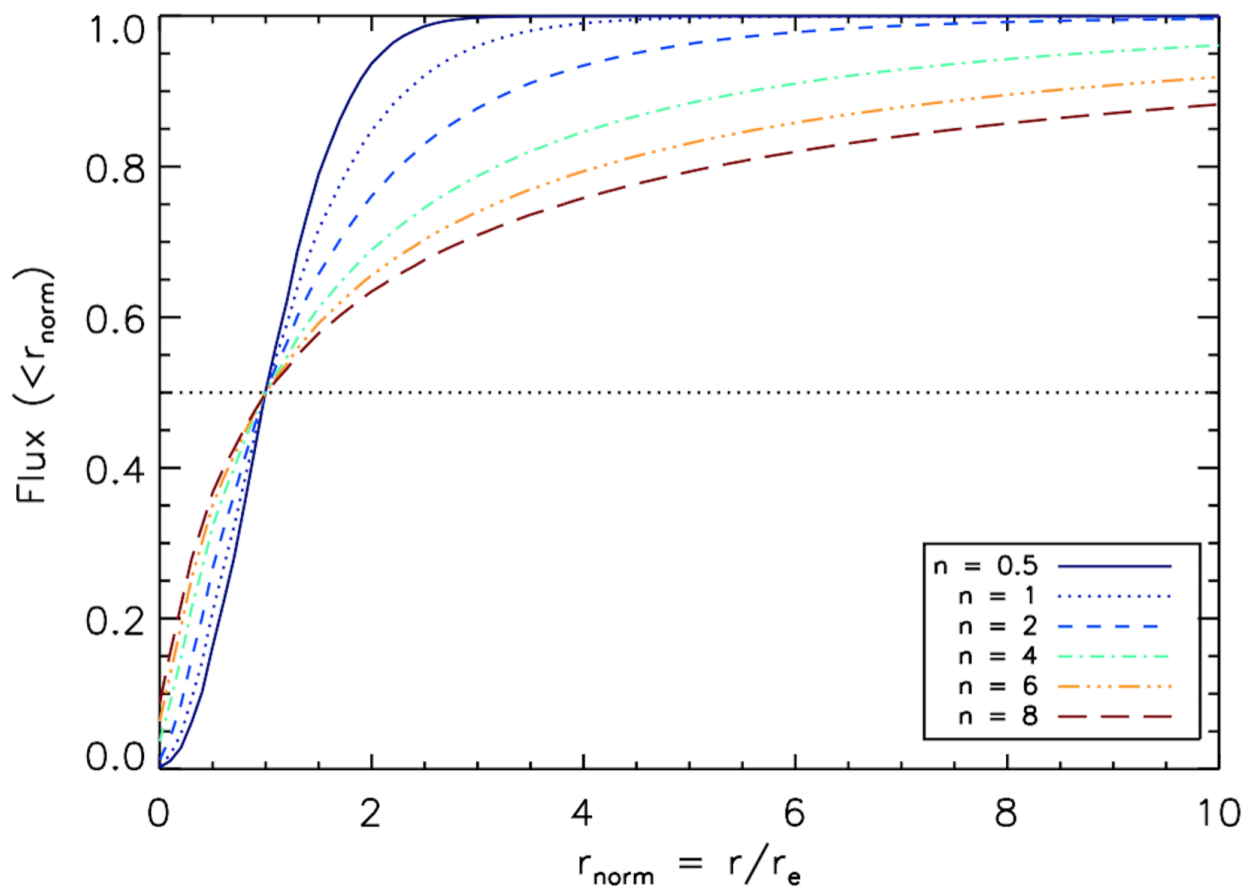
Figure C.8: Sérsic profiles, showing the fraction of the flux contained in a given multiple of the half–light radius (r_e).
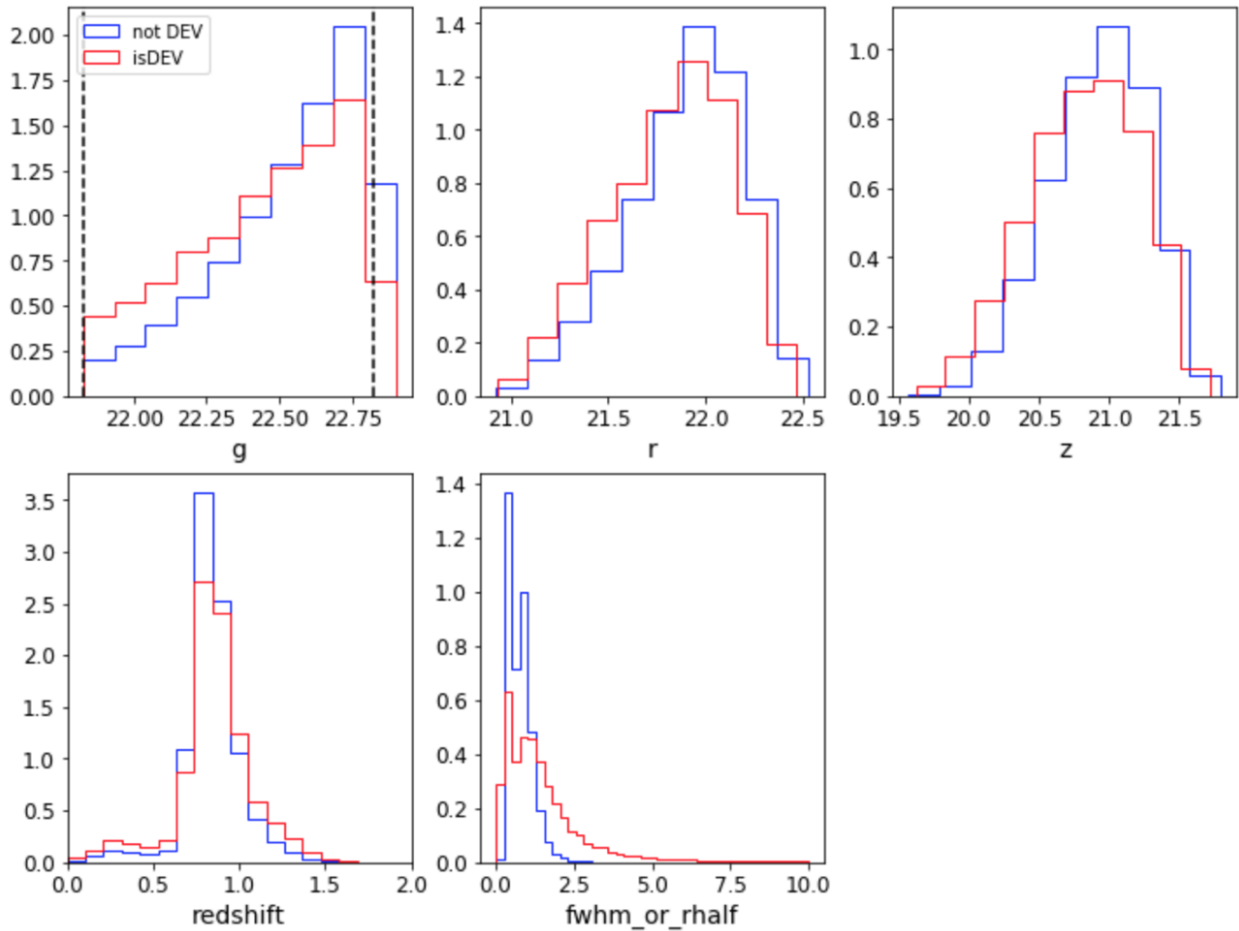
Figure C.9: DEV galaxies are systematically larger and brighter than EXP galaxies. The estimated PDFs are for EXP (blue) and DEV (red) sources for g, r, and z magnitude (top row), redshift (bottom left), and r_{half} (bottom right).

Because the SGC g mag estimated PDF (see Fig C.10) is a step function at $g = 22.825$, a Gaussian mixture model (GMM) will perform badly. The the number density of eBOSS ELGs is largest for fainter ELGs so we must model the faint tail well. To simulate drawing from the joint distribution of brightness, shape, and size, we bootstrap sample from the eBOSS sample.

C.2.2   ELG Almost–Targets

We construct our DR3–DEEP2 sample as follows. We match DEEP2 galaxies to the nearest DR3 tractor catalog sources using a $1''$ matching radius and keeping the nearest neighbor. We reclassify SIMP and PSF sources as EXP, just as we did for the eBOSS sample (see Section C.2.1), and then apply the following cuts,
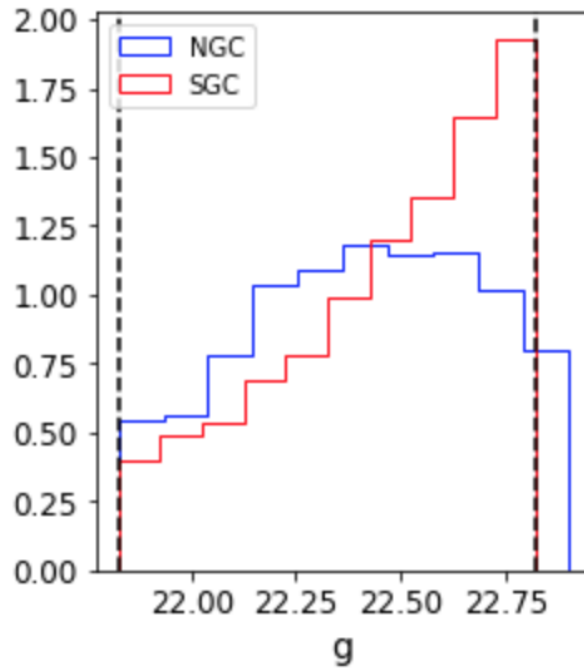
Figure C.10: Estimated PDFs of the number of spectroscopically confirmed galaxies in the NGC (blue) and SGC (red), with DECam g magnitude in the eBOSS selection boundaries. The NGC imaging does not reach the required depth of $g = 22.825$ mag.

- !NGC

- $0 \leq$ redshift ≤ 2 (heliocentric–corrected)

- brick_primary

- g, r, z flux > 0

- g, r, z flux ivar > 0

- type $\neq$ COMP

- $r_{\mathrm{half}} > 0.131''$ (Nyquist limit, one half of the DECam pixel scale)

- (EXP) $r_{\mathrm{half}} < 2.5''$

- (DEV) $r_{\mathrm{half}} < 5.0''$

Fig. C.11 compares the eBOSS and DR3–DEEP2 (cut to eBOSS ELG targets) samples for EXP galaxies by showing the estimated PDFs for g, r, and z flux, redshift, and r_{half}. Fig. C.12 shows that for EXP galaxies, g, r, z, and r_{half} depend on redshift in the same

way for the eBOSS and DR3–DEEP2 samples. The estimated PDFs in Fig. C.11 and the redshift dependence in Fig. C.12 show that the DR3–DEEP2 and eBOSS samples are very similar for EXP galaxies. We see similar agreement for DEV galaxies.
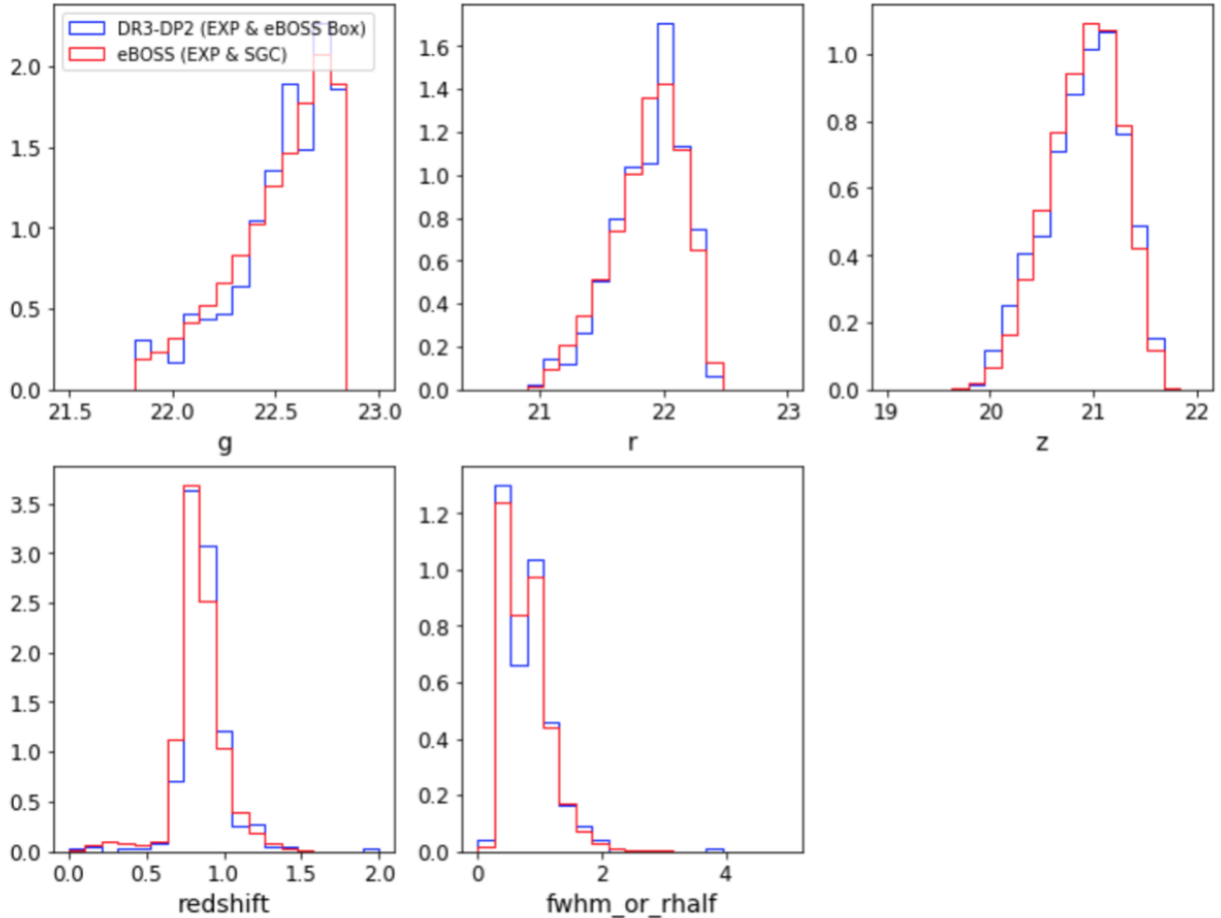

Figure C.11: estimated PDFs of g, r, z, redshift, and r_{half} for EXP galaxies. The eBOSS (red) and DR3–DEEP2 (blue) samples have very similar brightness, shape, and redshift distributions.

Because DR3–DEEP2 galaxies extend beyond the eBOSS selection boundaries, we can sample ELG–like galaxy properties in this region of parameter space and test how galaxies scatter into (e.g., from `Tractor` measurement error) into the eBOSS ELG sample. Fig. 4.9 shows that `Tractor` flux measurements are accurate to $0.1 - 0.3$ mag for $g \sim 22.9$ galaxies, so we keep DR3–DEEP2 SGC galaxies within 0.2 mag of the eBOSSS selection boundaries (g mag, $g - r$, $r - z$), which yields a sample of 1,064 EXP and 85 DEV galaxies. Fig. C.13 compares the resulting eBOSS and DR3–DEEP2 sample properties for EXP and DEV galaxies.

C.2.3 ELG Redshift Distribution

We now describe our algorithm to jointly sample an eBOSS $n(z)$ redshift and its associated brightness, shape, and size using our eBOSS and DR3–DEEP2 samples. The eBOSS $n(z)$ is the distribution of spectroscopic redshifts from the eBOSS–`Tractor` tables weighted by spectroscopic completeness (1/TSR). We drop the NGC spectroscopic redshifts because the NGC imaging data is incomplete. To sample from $n(z)$, we intentionally over–fit a 10 component GMM (see Fig. C.14). We draw redshifts from $n(z)$, dropping those outside the allowed redshift range [0,2], until there are N redshift samples. Each sample gets a unique id, which is an integer [1,N] that we call `id`. For each of the N redshifts, we find the nearest redshift in our (EXP–DEV combined) DR3–DEEP2 sample, which acts an $n(z)$–weighted draw from ELG–like galaxies within 0.2 mag of the eBOSS selection boundaries.

Next, we decide whether each galaxy should have an exponential or de Vaucouleurs profile using the followign chance model. We define an ELG as passing eBOSS ELG SGC target selection (see Section 5.3.2). If the galaxy is an ELG, we find its nearest redshift in the EXP eBOSS sample (90% of the time) or the DEV eBOSS sample (10% of the time); if not, we trim the DR3–DEEP2 sample to galaxies that extends beyond the eBOSS ELG selection boundaries, and find its nearest redshift in the trimmed EXP DR3–DEEP2 sample (90% of the time) or the trimmed DEV DR3–DEEP2 sample (10% of the time). This yields a sample of ELG–like eBOSS galaxies with the desired redshift distributed. Fig. C.15 shows the resulting g, r, z flux, redshift, and r_{half} PDFs for 10,000 draws from the above chance model.

We add the following to our sample: a random RA and Dec coordinate (sampling from the unit sphere), a uniform random position angle and minor to major axis ratio, and a unique id (`id_sample`) saying where the brightness and shape information came from which we call. `id_sample` is the SDSS–ID (`plate-mjd-fiberid`) if from the EXP or DEV eBOSS samples or the `Tractor`–ID (`brickid--objid`) if from the EXP or DEV DR3–DEEP2 samples.

C.3 Data Products

All data products are available at The National Energy Research Scientific Computing Center (NERSC), on Cori SCRATCH: `/global/cscratch1/sd/kaylanb/obiwan_out/eboss_elg`
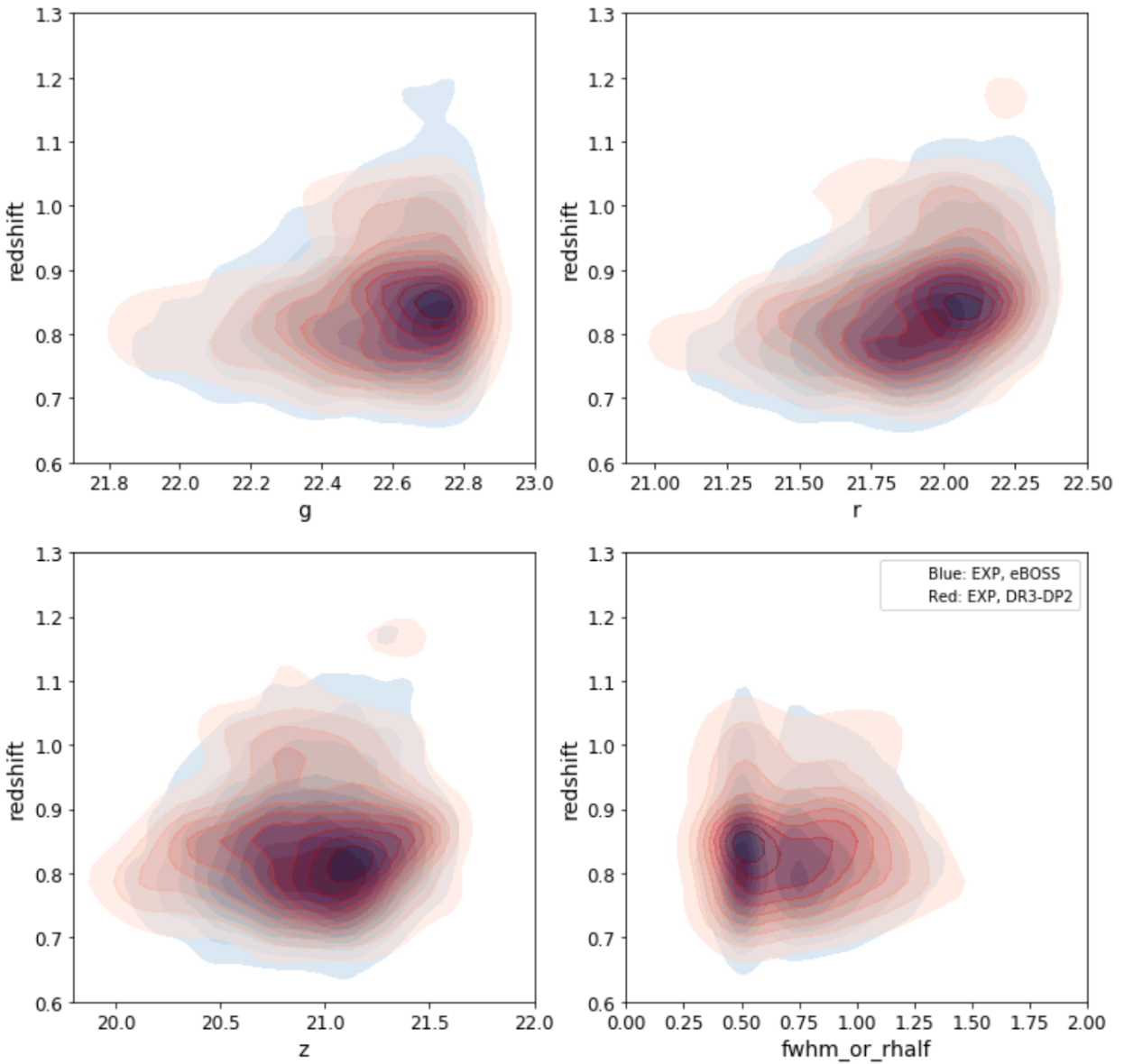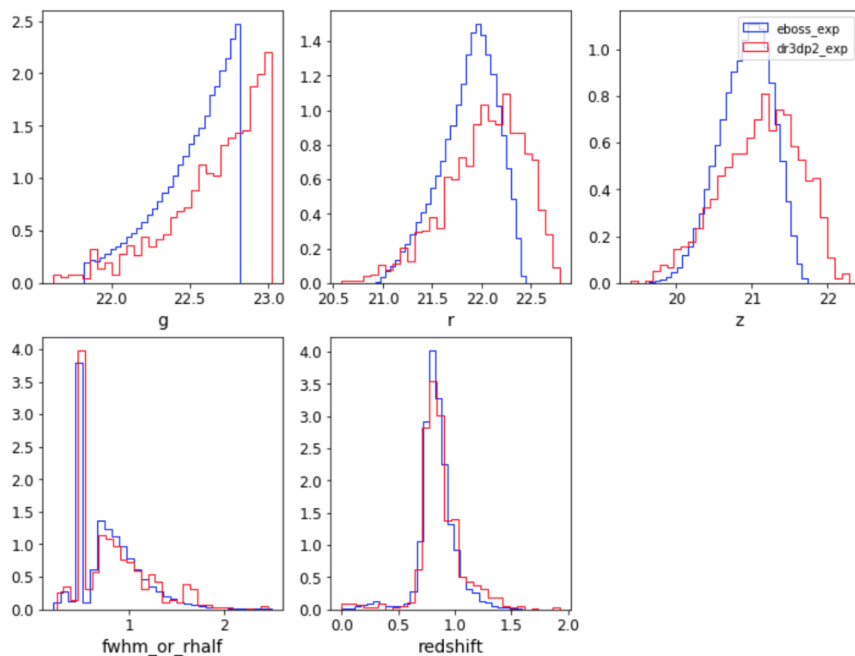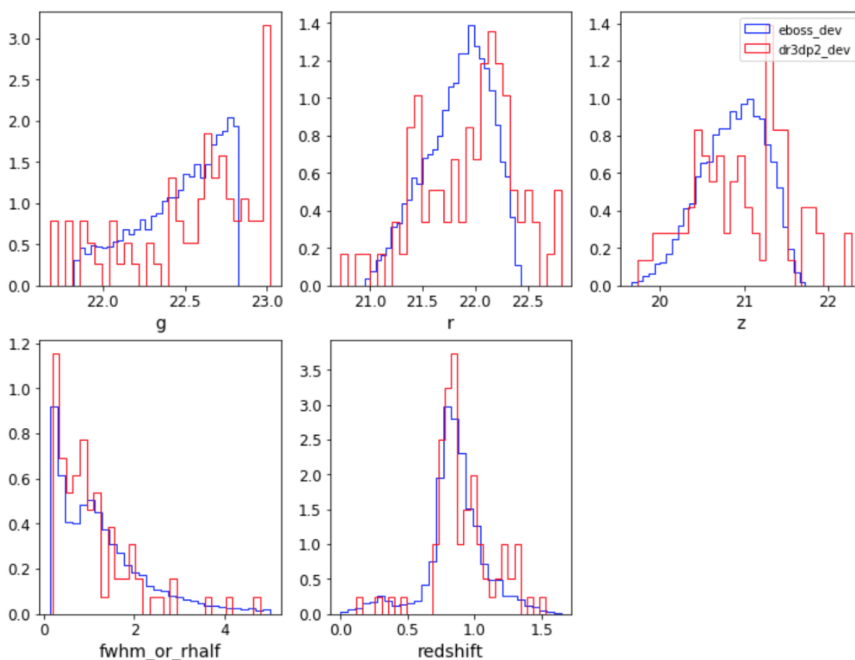
Figure C.12: 2-dimensional contour plots showing how redshift depends on g, r, z mag and r_{half} for EXP galaxies in the eBOSS (blue) and DR3–DEEP2 (red) samples.

(a) type EXP

(b) type DEV

Figure C.13: Comparison of the our final eBOSS and DR3–DEEP2 samples. In the estimated PDFs of g, r, $z$mag, r_{half}, and redshift, the DR3–DEEP2 (red) sample extends about 0.2 mag to brighter and fainter sources than the eBOSS (blue) sample. (a) EXP galaxies. (b) DEV galaxies. The DR3–DEEP2 sample is noisy because there are only 85 DEV galaxies in the sample.
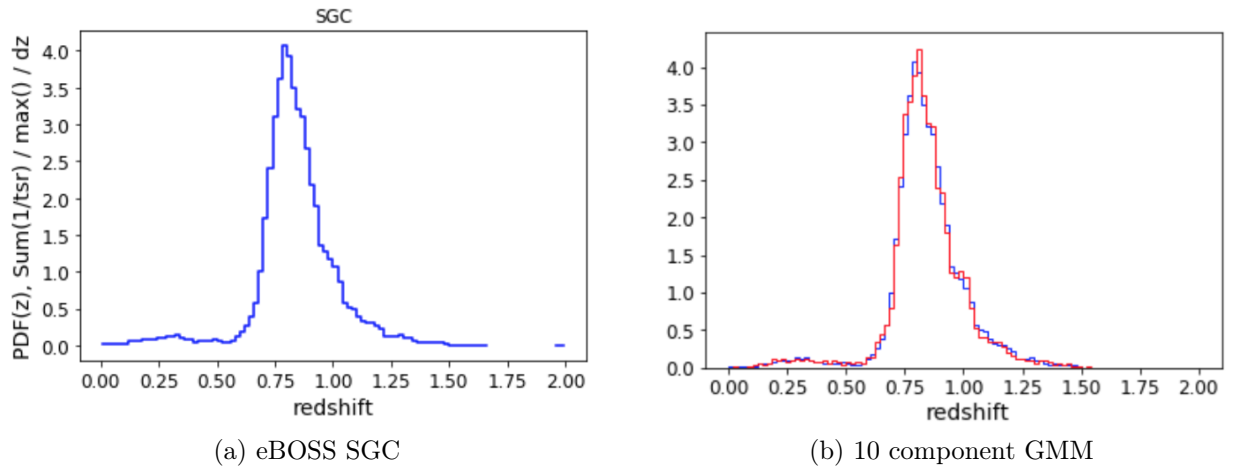
(a) eBOSS SGC

(b) 10 component GMM

Figure C.14: (Left) $n(z)$ from the eBOSS SGC region based on spectra in the eBOSS-`Tractor` tables. (Right) Same but over plotting 10,000 draws from our GMM (blue).
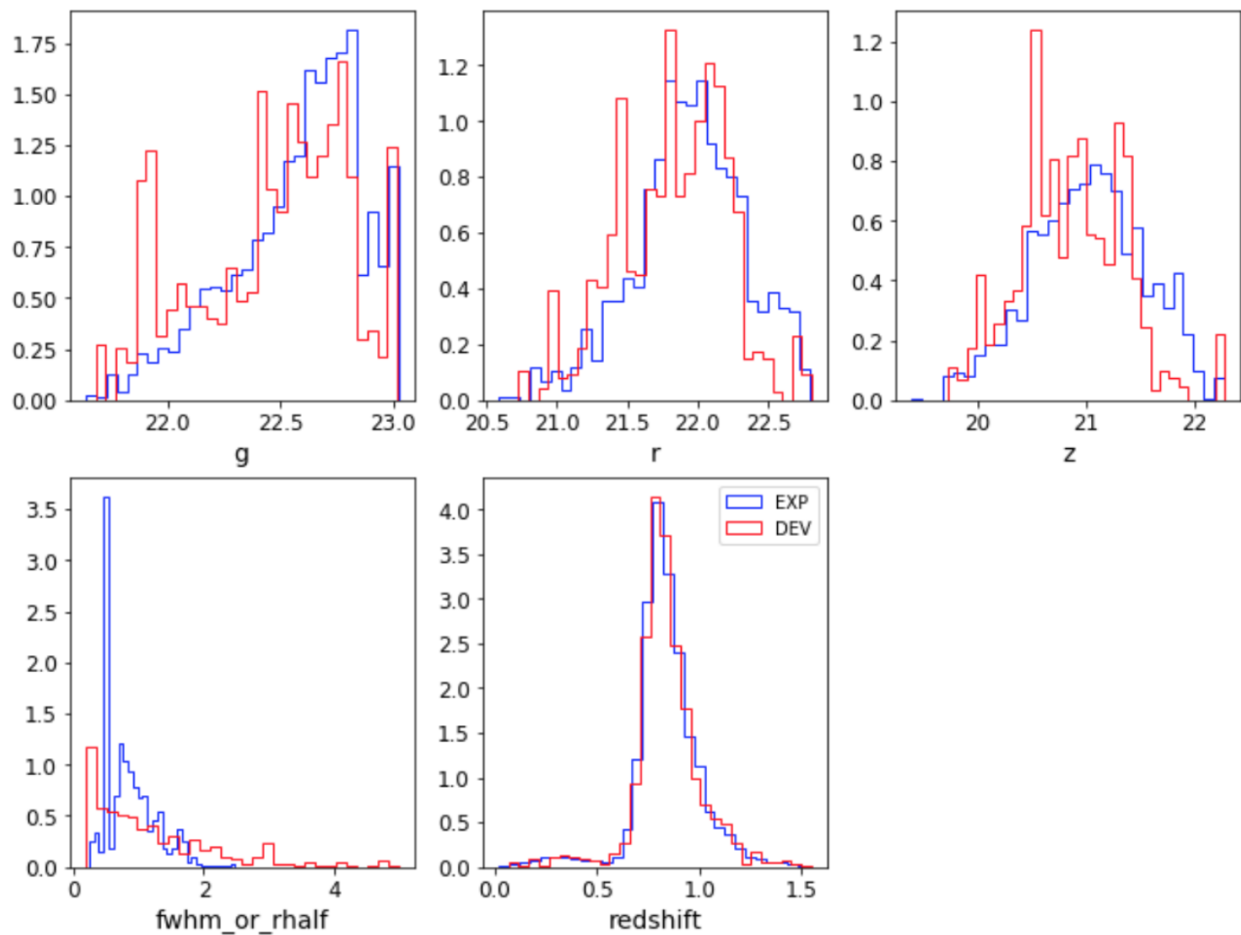
Figure C.15: Properties for EXP and DEV sources that are supposed to be representative of ELG-like eBOSS galaxies. The estimated PDFs of g, r, z, redshift, and r_{half} are from 10,000 draws from our chance model (see Section C.2.3).